The CESR Test Accelerator Electron Cloud Research Program Phase I Report

Editors: *M.A. Palmer, M.G. Billing, G.F. Dugan, M.A. Furman, D.L. Rubin*

December 20, 2011

Program Contributors:

N. Omcikus[1], K.C. Harkay[2], R. Dowd[3], W. Guo, S.Y. Zhang[4], R.L. Holtzapple[5], L. Fabrizio[5], M. Randazzo[5], D. Asner[6], M. Cunningham[6], D. Carmody[7], J. Chu[7], F. Antoniou[8], S. Calatroni[8], F. Caspers[8], M. Gasior[8], R. Jones[8], Y. Papaphilippou[8], J. Pfingstner[8], G. Rumolo[8], H. Schmickler[8], M. Taborelli[8], D. Gonnella[9], J. Jones[10], A. Wolski[10], D. Teytelman[11], J.P. Alexander[12], J. Barley[12], L. Bartnick[12], M.G. Billing[12], K.R. Butler[12], J.R. Calvey[12], S.S. Chapman[12], G.W. Codner[12], M. Comfort[12], C.C. Conolly[12], J.V. Conway[12], J.A. Crittenden[12], C.A. Dennett[12], J.A. Dobbins[12], G.F. Dugan[12], N. Eggert[12], M. Ehrlichman[12], E. Fontes[12], M.J. Forster[12], R.E. Gallagher[12], S.W. Gray[12], S. Greenwald[12], D.L. Hartill[12], W. Hartung[12], Y. He[12], R. Helms[12], L. Hirxhman[12], W.H. Hopkins[12], N. Kaminsky[12], J. Kandaswamy[12], J-S. Kim[12], D.L. Kreinick[12], B. Kreis[12], J. Lanzoni[12], Z. Leong[12], Y. Li[12], H. Liu[12], X. Liu[12], J.A. Livezey[12], A. Lyndaker[12], J. Makita[12], M. McDonald[12], V. Medjidzade[12], R.E. Meller[12], T.P. Moore[12], T.I. O'Connell[12], M.A. Palmer[12], S.B. Peck[12], D.P. Peterson[12], G.A. Ramirez[12], M.C. Rendina[12], P. Revesz[12], D.H. Rice[12], N.T. Rider[12], D.L. Rubin[12], D.C. Sagan[12], S. Santos[12], J. Savino[12], R.M. Schwartz[12], R. Seeley[12], J. Sexton[12], J. Shanks[12], J.P. Sikora[12], E.N. Smith[12], K.W. Smolenski[12], K. Sonnad[12], M. Stedinger[12], C.R. Strohman[12], A.B. Temnykh[12], M. Tigner[12], J.T. Urban[12], S. Vishniakou[12], W. Whitney[12], T. Wilksen[12], H.A. Williams[12], Y. Yariv[12], M.C. Ross[13], C.Y. Tan[13], R. Zwaska[13], B. Carlson[14], K. Hammond[15], Department of Physics, Harvard University, Cambridge, MA 02138, U.S.A. [15], M. Lawson[15], C. Cude[16], T. Demma[17], J. Flanagan[18], H. Fukuma[18], T. Ishibashi[18], P. Jain[18], K. Kanazawa[18], S. Kato[18], K. Kubo[18], K. Ohmi[18], K. Oide[18], H. Sakai[18], K. Shibata[18], Y. Suetsugu[18], H. Tajima[18], M. Tobiyama[18], J. Urakawa[18], R.J. Macek[19], J. Byrd[20], C.M. Celata[20], J.N. Corlett[20], S. De Santis[20], M.A. Furman[20], A. Jackson[20], R. Kraft[20], D.V. Munson[20], G. Penn[20], D.W. Plate[20], A. Rawlins[20], M. Venturini[20], M. Zisman[20], E.L. Wilkinson[21], H. Jin[22], L. Boon[23], A.F. Garfinkel[23], D. Kharakh[24], J. Ng[24], M.T.F. Pivi[24], L. Wang[24], R.P. Badman[25], S. Veitzer[26], L. Schächter[27], P. Kehayias[28], and L. Hales[29]

[1]American River College, Sacramento, CA 95841, U.S.A.
[2]Argonne National Laboratory, Argonne, IL 60439, U.S.A.
[3]Australian Synchrotron, Clayton, 3168, Australia.
[4]Brookhaven National Laboratory, Upton, NY 11973, U.S.A.
[5]Physics Department, California Polytechnic State University, San Luis Obispo, CA 93407, U.S.A.
[6]Department of Physics, Carleton University, Ottawa, Ontario, K1S 5B6, Canada.
[7]Department of Physics, Carnegie Mellon University, Pittsburgh, PA, 15389, U.S.A.
[8]CERN, CH-1211 Genève 23, Switzerland.
[9]Department of Physics, Clarkson University, Potsdam, NY 13699, U.S.A.
[10]Cockroft Institute, Warrington, Cheshire, U.K.
[11]Dimtel, Inc., San Jose, CA 95124, U.S.A.
[12]Cornell Laboratory for Accelerator-based Sciences and Education, Cornell University, Ithaca, NY, 14850, U.S.A.

[13]Fermi National Accelerator Laboratory, Batavia, IL 60510, U.S.A.
[14]Physics Department, Grove City College, Grove City, PA 16127, U.S.A.
[15]Department of Physics, Harvey Mudd College, Claremont, CA 91711, U.S.A.
[16]Department of Physics, Indiana University, Bloomington, IN 47405, U.S.A.
[17]Istituto nazionale di Fisica Nucleare - Laboratori Nazionali di Frascati, 00044 Frascati, Italy.
[18]High Energy Accelerator Research Organization (KEK), Tsukuba, Ibaraki 305-0801, Japan.
[19]Los Alamos National Laboratory, Los Alamos, NM 87544, U.S.A.
[20]Lawrence Berkeley National Laboratory, Berkeley, CA 94270, U.S.A.
[21]Department of Physics, Loyola University, Chicago, IL, 60626, U.S.A.
[22]Department of Physics, Postech, Pohang, Gyeongbuk 790-784, R.O.K.
[23]Department of Physics, Purdue University, West Lafayette, IN 47907, U.S.A.
[24]SLAC National Accelerator Laboratory, Menlo Park, CA 90425, U.S.A.
[25]Department of Physics, Syracuse University, Syracuse, NY 13244, U.S.A.
[26]Tech-X Corporation, Boulder, CO, 80303, U.S.A.
[27]Department of Electrical Engineering, Technion-IIT, Haifa, 32000, Israel.
[28]Department of Physics and Astronomy, Tufts University, Medford, MA 02155, U.S.A.
[29]Department of Physics and Astronomy, University of Utah, Salt Lake City, UT 84112, U.S.A.

Contents

List of Figures

List of Tables

Chapter 1

Studies of Electron Cloud Growth and Its Mitigation

1.1 Local EC Build-Up and Mitigation Studies

1.1.1 Special Features of the CesrTA EC Program

The CesrTA program is almost certainly the single most comprehensive effort to measure and characterize the EC, and to assess techniques for its mitigation, in e^+e^- storage rings to date [1]. Mitigation techniques studied include low-emission coatings such as TiN, amorphous carbon and diamond-like carbon on aluminum chambers; grooves etched in copper chambers; clearing electrodes; and more. Combined with an extensive array of instrumentation and diagnostic tools such as retarding-field analyzers and shielded-pickup detectors, much has been learned to date about the physics governing the buildup of electron clouds. While some of these diagnostics instruments had been employed in previous studies elsewhere in various combinations, the CesrTA program includes all of them in a single storage ring, with measurements analyzed by the same group of researchers. In addition, several pre-existing simulation codes have been augmented, cross-checked, and in some cases debugged, and applied to the analysis of the data.

The flexibility of the beam manipulation at CesrTA affords the unique and valuable possibility of studying the electron cloud formation and dissipation with a beam consisting of an almost arbitrary fill pattern and bunch intensity. This flexibility allows, in principle, to tease out the contributions to the electron cloud due to photoemission from that due to secondary electron emission. This is a consequence of the fact that short bunch trains (typically fewer than 10 bunches) lead to an electron cloud dominated by photoemission, while long bunch trains (say, more than 40) lead to an electron cloud typically dominated by secondary electron emission (unless the peak value of the SEY is unusually low, say < 0.9). In addition, an isolated "witness bunch" can be placed at varying distances from the end of the train, thus affording the possibility of studying the dissipation of the electron cloud as a function of time.

In addition, the beam energy can be varied in the range $\sim 2 - 5$ GeV, which provides a powerful handle on the synchrotron radiation intensity and hence on the photoelectron creation rate. As if the above features were not enough, the instrumentation installed at CesrTA allows the measurement of the electron cloud density bunch by bunch, which provides yet another handle to disentangle the

intensity of the photoelectrons from the secondaries, as well as a more detailed and time-resolved analysis of the build-up of the EC density.

1.1.2 Overview

The buildup of high densities of low-energy electrons produced by the intense synchrotron radiation in electron and positron storage rings has been under active study since it was identified in the mid-90's in the KEK Photon Factory (PF) when operated with a positron beam [2]. While this phenomenon did not present an operational limitation at the PF under nominal conditions, the observation raised immediate concerns for both B Factories, then under design, and triggered significant simulation efforts [3] aimed at quantifying the phenomenon and designing mitigation techniques. Several years later, as the luminosity performance in the B Factories was pushed towards its specified goal, the electron cloud became at some point the most significant limitation. Mitigating this effect at both B Factories then became essential to reach, and then exceed, the design performance [4].

Almost concurrently with the above-mentioned developments at the PF and the B Factories, concerns arose in 1995-96, based on prior experience at the ISR, that electrons might spoil the LHC vacuum [5]. Early 1997 calculations showed that the LHC would be subject to an ECE [6], chiefly because the beam emits copious synchrotron radiation upon traversing the dipole bending magnets, in analogy with e^+e^- storage rings. Indeed, the LHC is the first proton storage ring ever built in which synchrotron radiation is significant: although the critical photon energy is only $\sim$ 44 eV at 7 TeV beam energy (as opposed to several keV in typical e^+e^- storage rings), this value is well above the work function of the chamber metal, hence photoemission inside the chamber is unavoidable. A straightforward calculation yields an estimate of 0.4 photons emitted per proton per dipole magnet traversal, also at 7 TeV beam energy. Although $\sim$50% of these photons have energies below the work function of the metal, the remaining 50% lead to a substantial number of photoelectrons. Further calculations [6, 7], including the effects of secondary electron emission, quickly revealed the possibility of a substantial ECE. In the case of the LHC, the primary concern from the ECE is the power deposited by the electrons on the beam screen as they rattle around the chamber under the action of the beam; this power must be dissipated by the cryogenic system if the LHC superconducting magnets are to work according to specifications. Since the cryogenic system was designed before the prediction of the ECE in the LHC, a significant "crash program" was launched in 1997[1] to better estimate the power deposition, to identify the conditions under which the cooling capacity might be exceeded, and to devise mitigation mechanisms if necessary [8]. As part of this effort, the ECE has been experimentally studied at the SPS and the PS at the high beam intensities required for nominal LHC operation (recent experience at the LHC has confirmed the expectation of a significant ECE, even though the beam energy is presently only 3.5 TeV [9]). This crash program at the LHC was almost certainly the single most comprehensive effort to understand the electron cloud in a hadron machine, and was comparable in scope to the present program at CESRTA for an e^+e^- machine.

The above-mentioned ECE's are related to previously observed electron- proton dynamical effects such as beam-induced multipacting (BIM), first observed at the CERN proton storage ring ISR [10] when operated with bunched beams. Closely related to BIM is trailing-edge multipacting observed at the LANL spallation neutron source PSR [11], where electron detectors register a large signal

[1] The website `http://ab-abp-rlc.web.cern.ch/ab-abp-rlc-ecloud/` provides documentation and software tools related to this effort.

during the passage of the tail of the bunch even for stable beams. All ECEs in e^+e^- as well as in hadron storage rings have precursors in the e-p instabilities for bunched and unbunched beams first seen at BINP in the mid-60s [12].

The interest generated by the observations at the PF published in 1995 triggered a series of dedicated workshops the most recent of which was held at Cornell in 2010 [13]. The similarities of the ECE's in e^+e^- and hadron storage rings is evidenced by the simultaneous and comparable participation, since 1997, of both communities in these workshops. Phenomena related to electron cloud buildup have been reported (and in some cases been a performance- limiting factor) at the Advanced Photon Source at ANL [14], BEPC [15], the Spallation Neutron Source at ORNL [16], the Relativistic Hadron Collider at BNL [17], the Proton Storage Ring at LANL [18], the DAΦNE Φ-factory at the INFN-LNF in Frascati [19], PEP-II at SLAC [20, 21], the Tevatron Main Injector at FNAL [22], the CERN Proton Synchrotron [23] and Super Proton Synchrotron [24] and the LHC [9].

The enhanced understanding of electron cloud physics has identified the phenomenon as a primary potential limiting factor in the operation of damping rings for future e^+e^- linear colliders [25–27]. The determining physical phenomena governing the characteristics of the clouds are the generation of photoelectrons, their trajectories in the transient and ambient electric and magnetic fields, and the secondary electron yield properties of the vacuum chamber. Thus the RF structure of the beams, their intensities, the shape and dimensions of the vacuum chambers, and especially the surface physics properties of those chambers affect the production of electrons by incident electrons, and are therefore important factors in the rates of buildup and decay. A variety of mitigation techniques have been experimentally studied and implemented in operating beamlines, such as grooves on the chamber surface of the LHC arcs, the TiN coating in the PEP-II ring [28] and at the Spallation Neutron Source, and weak solenoidal magnetic fields at both B Factories [21, 29].

The CesrTA program is almost certainly the single most extensive project for the study of mitigation techniques in e^+e^- storage rings to date, including mitigation techniques based on low-emission coatings such as TiN, amorphous carbon and diamond-like carbon on aluminum chambers; grooves etched in copper chambers; clearing electrodes; and more. Combined with an extensive array of instrumentation and diagnostic tools such as retarding-field analyzers and shielded-pickup detectors, much has been learned to date about the physics governing the local buildup of electron clouds.

In essentially all cases of practical interest, it is the secondary electron emission process that dominates the build-up of the electron cloud because this process leads to a compounding effect of the electron density under the action of successive bunches traversing the chamber: the more electrons are present in the chamber, the more electrons are generated upon striking the chamber walls. The CesrTA facility affords the unique and valuable possibility of studying the electron cloud formation and dissipation with a beam consisting of an almost arbitrary fill pattern and bunch intensity. This flexibility allows to tease out the contributions to the electron cloud due to photoemission from secondary electron emission. Short bunch trains (say, fewer than 10 bunches) lead to an electron cloud dominated by photoemission, while long bunch trains (say, more than 40) lead to an electron cloud dominated by secondary electron emission. As if this flexibility were not enough, CesrTA also allows the measurement of the electron cloud bunch by bunch, which provides another way to disentangle the two above-mentioned effects: the formation of the electron cloud at the beginning of the train is dominated by photoemission, while secondary emission dominates the formation towards the tail. In addition, an isolated "witness bunch" can be placed at varying distances from the end of the train, thus affording the possibility of studying the dissipation of the

electron cloud as a function of time.

1.1.3 Simulation Program

A broad-based program of developing, comparing and benchmarking electron cloud buildup simulation codes was initiated in the CesrTA collaboration in 2008 and continues today. We have used CesrTA input parameters as input to the simulation codes ECLOUD [30, 31], CLOUDLAND [32, 33], POSINST [20, 34], WARP/POSINST [35] and PEHTS [36], and compared the results against measurements. By iterating this process, we are able to pin down parameters that are not well known and thereby make more reliable extrapolations to the future ILC damping rings. The main (indeed, the only) parameters that are not well known are those pertaining to the electronic surface properties, ie. photon reflectivity, photoemission and secondary electron emission.

1.1.3.1 EC Build-Up Modeling

Essential components of the codes are photoelectron generation models, time-sliced calculations of macroparticle dynamics including beam kicks, the space charge force from the cloud itself, and the Lorentz forces of ambient magnetic fields, and the the model describing the various components of the secondary yield (SEY). The ECLOUD and POSINST models use two-dimensional approximations for the electric fields and have successfully reproduced a variety of coherent tune shift measurements, as well as local RFA and shielded-pickup measurements. These 2D codes are relatively fast, and are generally successful in predicting the features of the electron cloud in regions of the ring that are essentially 2D, namely field-free regions and long magnets, especially dipoles. The CLOUDLAND [37] and WARP/POSINST [38] codes are 3D and therefore far more computationally expensive, and have been used to model the electron cloud in essentially 3D regions such as quadrupole, sextupole and wiggler magnets, providing information on the long-term trapping of electrons. In addition, it should be pointed out the ECLOUD and POSINST are build-up codes, assuming the beam is a prescribed function of space and time and therefore does not respond to the electron cloud. CLOUDLAND and WARP/POSINST, in addition to being 3D, have the option of describing the beam fully dynamically, so that the beam and the electron cloud respond to their mutual simultaneous influence. in quadrupole, sextupole and wiggler magnets, providing information on the long-term trapping of electrons.

1.1.3.2 Photoelectron Models

The components of the photoelectron generation model are the azimuthal location distribution of photoelectrons produced on the wall of the vacuum chamber, the angular function governing their initial momentum direction, and their kinetic energy spectrum. The code benchmarking project revealed that reconciliation of the time structure of density buildup in the ECLOUD and POSINST codes for CesrTA conditions required a modification of the ECLOUD model for the angular distribution to match that employed by POSINST. The simple model implemented at present uses a single energy-independent value for the quantum efficiency, ignores the incident photon energy spectrum and generates an ad-hoc photoelectron energy distribution which must be re-tuned for each set of beam conditions under study.

While the modeling for the coherent tune measurements proved to be rather insensitive to the assumed photoelectron energy distribution (see Section **??**), the local RFA measurements, and especially the time-resolved shielded-pickup pulse shapes have been shown to impose strict constraints on the photoelectron generation model. These results are described in Sect. 1.2.2 below.

On the other hand, the modeling of the coherent tune shift measurements depends critically on the azimuthal location distribution of the produced photoelectrons. As the bunch current increases, the contribution from the dipole regions begins to dominate the total tune shift, since the cloud electrons are trapped on field lines near the vertical plane of the beam. If photon reflection were to be ignored in the model, this dominant contribution would not contribute at all, since no photoelectrons would be produced on the top or bottom of the beampipe. The CesrTA cloud modeling effort thus required a substantial effort to develop a photon transport model, as described in Section **??**.

1.1.3.3 Photon Transport

In this section, we present four examples of `SYNRAD3D` photon transport simulations using CesrTA lattices and vacuum chambers.

Example 1: Photon Emission in a Dipole As the first example, we consider the CesrTA ring with a 5.3 GeV positron beam, and use `SYNRAD3D` to simulate photon emission only in the arc dipole at B12W. The vacuum chamber is a simple ellipse (dimensions 9 cm horizontal by 5 cm vertical), and the scattering is purely specular. The photons are generated only in the upstream end of this dipole but propagate downstream and can scatter.

In Fig. 1.1, we show a collection of photon trajectories, projected onto the bend plane. Photons generated by the beam in B12W strike the B12W vacuum chamber a short distance downstream. Some are absorbed here, but most scatter and strike the vacuum chamber further downstream, in B13W. More are absorbed here, but many others scatter again.

These photon trajectories in three dimensions are shown in Fig. 1.2. Photons from the source (on the right) propagate and strike the vacuum chamber. Blue dots represent absorption sites. For this simple example, in which the photon source is localized longitudinally, the absorption site locations tend to be clumped in several clusters (at the location of downstream dipoles), with decreasing intensity as we get further from the source.

Other features of the photon scattering and absorption process are shown in Fig. 1.3 and Fig. 1.4.

In Fig. 1.3(left), a histogram of the number of reflections is presented. Many photons suffer no reflections, that is, they are absorbed as soon as they hit the vacuum chamber, but most are reflected several times before being absorbed. The mean number of reflections is 5.4.

In Fig. 1.3(right), a histogram of the energy of all absorbed photons is presented. This is strongly peaked at zero but has a long tail out to at least 5 keV.

In Fig. 1.4, a two dimensional histogram of the number of photons vs. location of the absorption site along the vacuum chamber perimeter is presented. This is is peaked at the outside edge of the vacuum chamber, where the direct photon strikes occur, but there is long tail extending around the entire surface of the vacuum chamber, due to the reflected photons.

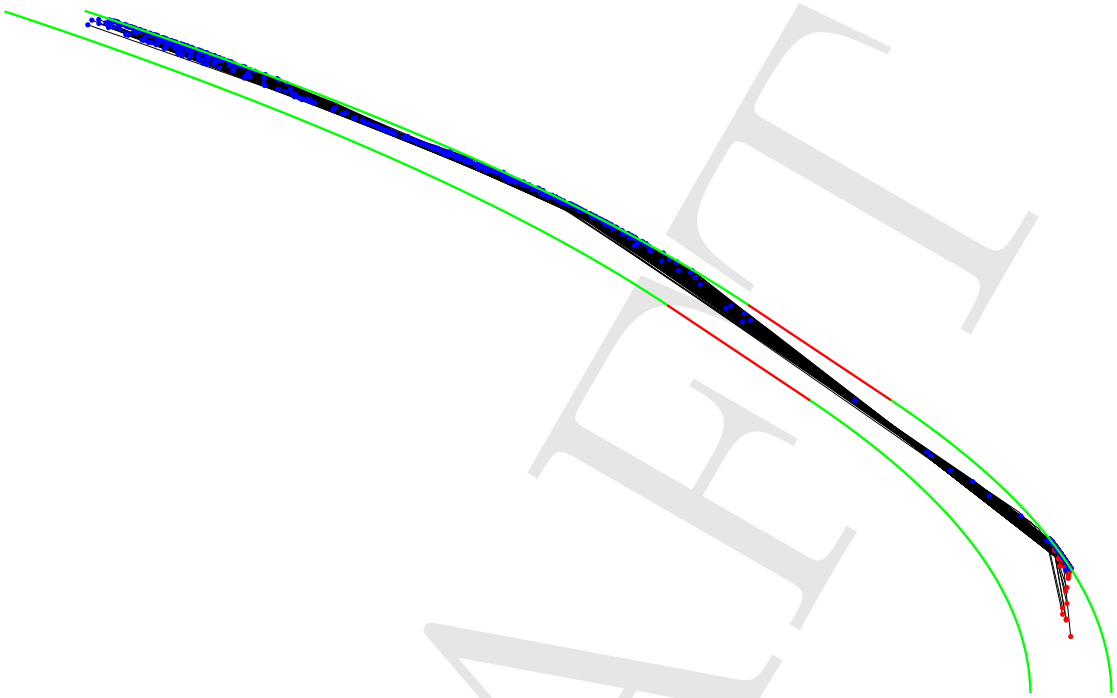

Figure 1.1: Photon trajectories from B12W: projections onto bend plane. The red dots at the lower right are the photon source (the radiating beam in a section of the dipole). Black lines are photon trajectories, and blue dots are photon absorption sites. The green lines in the lower right are the edges of the vacuum chamber in B12W; the red lines are the edges in a straight section, and the green lines on the left are the edges of the vacuum chamber in the next dipole, B13W. The geometry has been distorted for purposes of illustration.

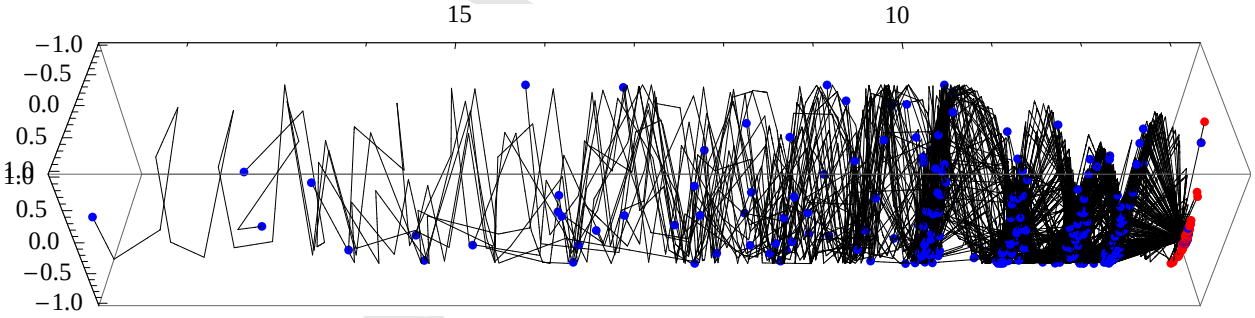

Figure 1.2: Photon trajectories from B12W in three dimensions. The photon source is on the right. Black lines are trajectories, and blue dots are photon absorption sites. The transverse geometry has been distorted from an ellipse to a circle, and the longitudinal dimension has been rectified and divided by 10, for purposes of illustration.

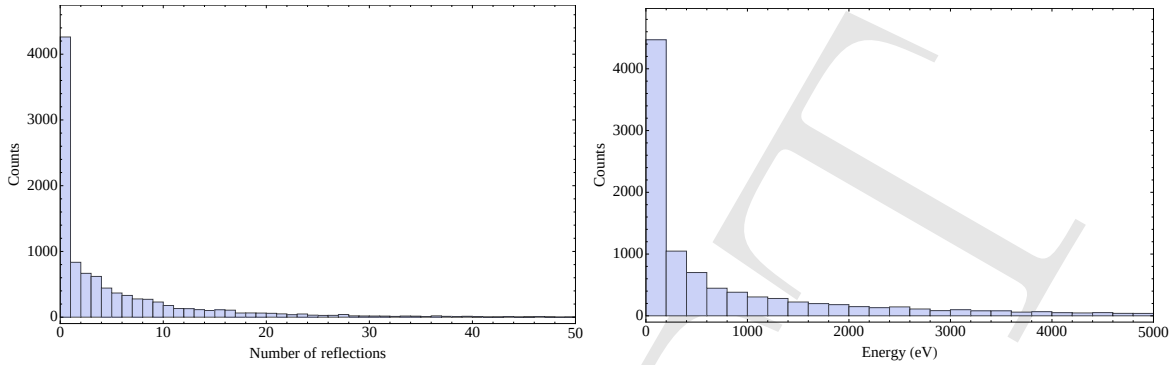

Figure 1.3: Reflection distribution (left) and energy distribution (right). The mean number of reflections is 5.1

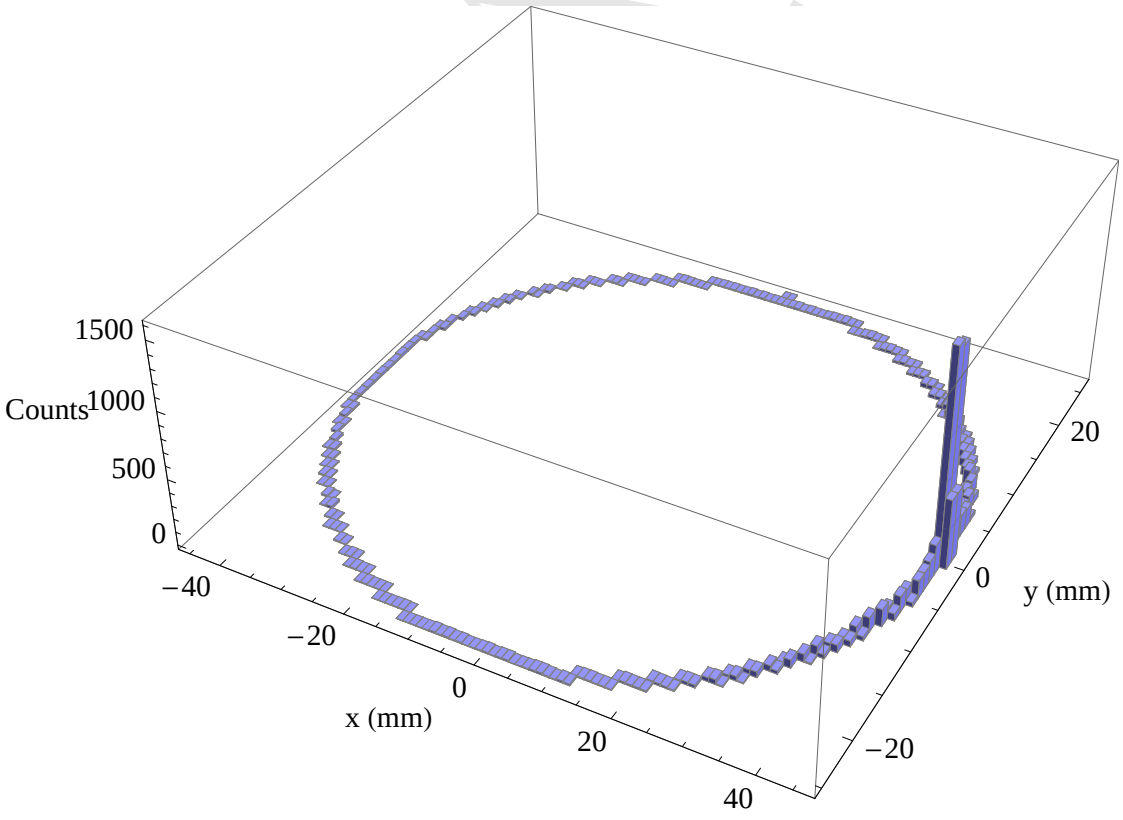

Figure 1.4: Distribution of photon absorption sites around the vacuum chamber perimeter

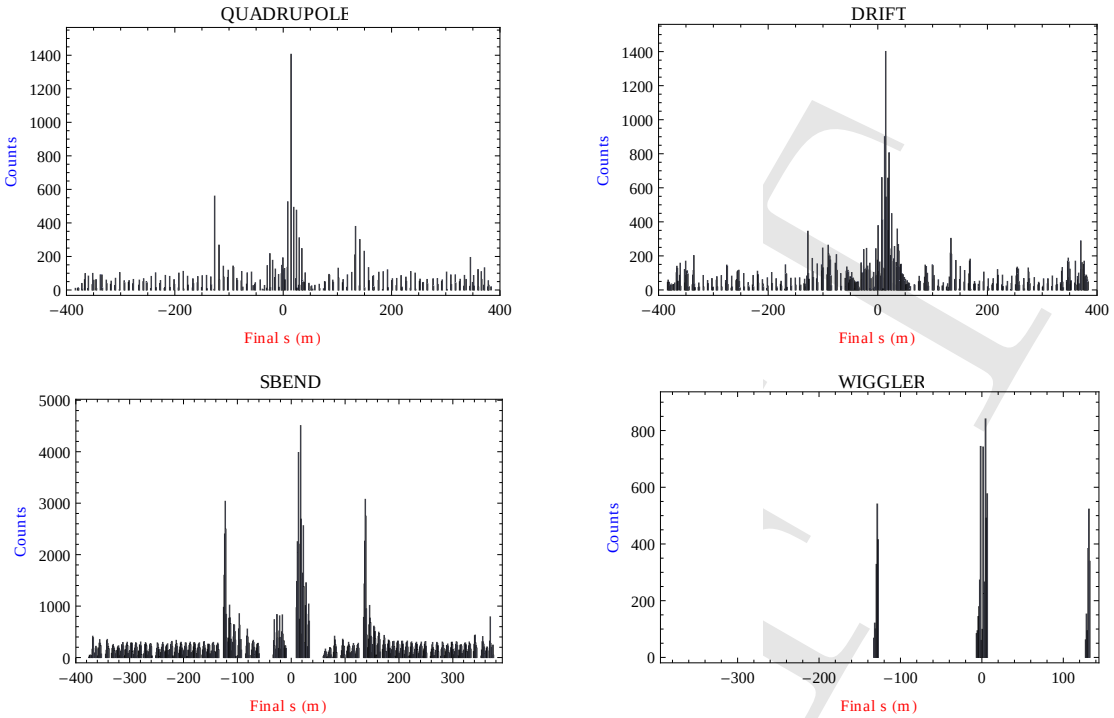

Figure 1.5: Distribution of photon absorption sites vs. longitudinal position, for different magnetic environments. The origin for the longitudinal coordinate is the center of the L0 straight section. The ring circumference is about 760 m.

Example 2: Photon emission throughout the Ring, elliptical vacuum chamber, no diffuse scattering For the second example, photon emission throughout the CesrTA ring from a 2.1 GeV positron beam is simulated. (The lattice name is `2085mev_20090516`). The vacuum chamber is again a simple ellipse, and the scattering is purely specular.

In Fig. 1.5, the distribution of photon absorption sites around the ring is shown, sorted by the type of magnetic environment in which the absorption occurs. This information is important for simulations of electron cloud growth, which is strongly influenced by the magnetic environment.

The wigglers in the L0 straight section are responsible for the large peaks near $s = 0$. The large peaks near $s = \pm 130$ m are due to wigglers in the arcs near these locations. The small peaks in the arcs are due to the regular CesrTA dipoles.

In Fig. 1.6, we present the photon intensity distribution (in photons/meter/radian) vs. polar angle (measured around the vacuum chamber, with zero angle corresponding to the radial outside direction), averaged over each type of magnetic environment.

In the wigglers, most of the photons come from the radiation fans in an upstream wiggler region, so there are strong peaks on both edges of the vacuum chamber. In the bends, most of the radiation is from direct strikes from upstream dipoles, so there is only a strong peak on the radial outside edge, together with a long tail, due to scattering. In the quadrupoles and drifts, there are two peaks, with the higher one at the radial outside, and a distribution between the peaks due to scattering.

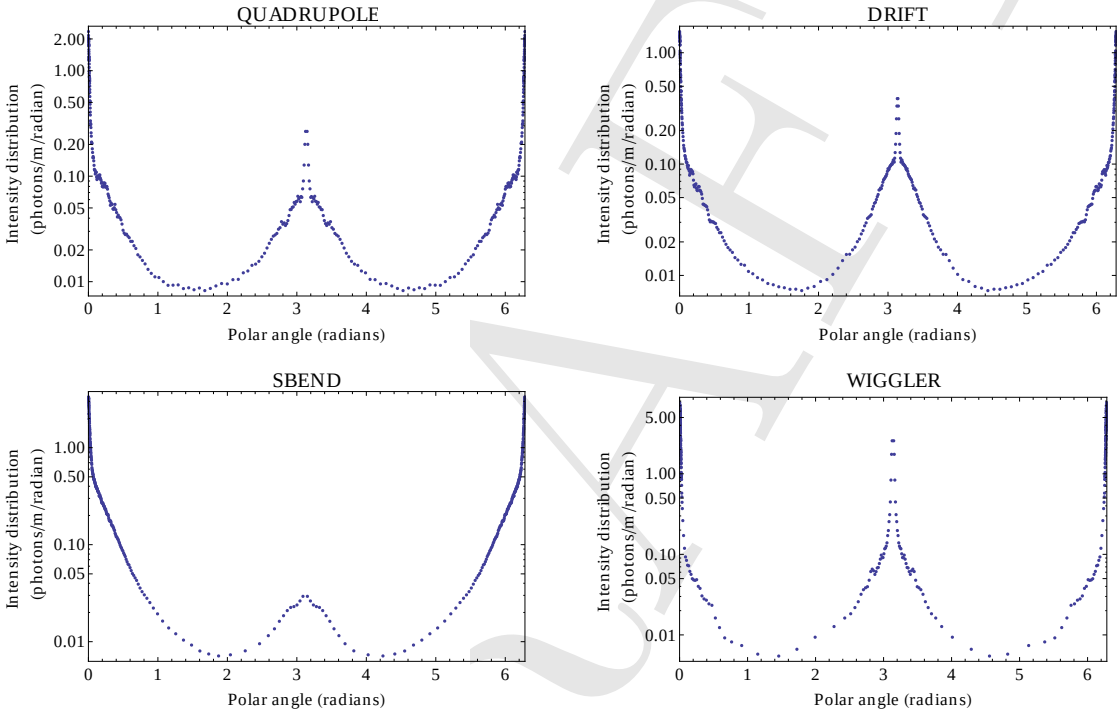

Figure 1.6: Photon intensity distribution (in photons/meter/radian) vs. polar angle (measured around the vacuum chamber, with zero angle corresponding to the radial outside direction), averaged over each type of magnetic environment. A 9 cm (horizontal) by 5 cm (vertical) elliptical vacuum chamber profile is assumed throughout the ring, and all scattering is specular. Top-bottom symmetry is assumed.

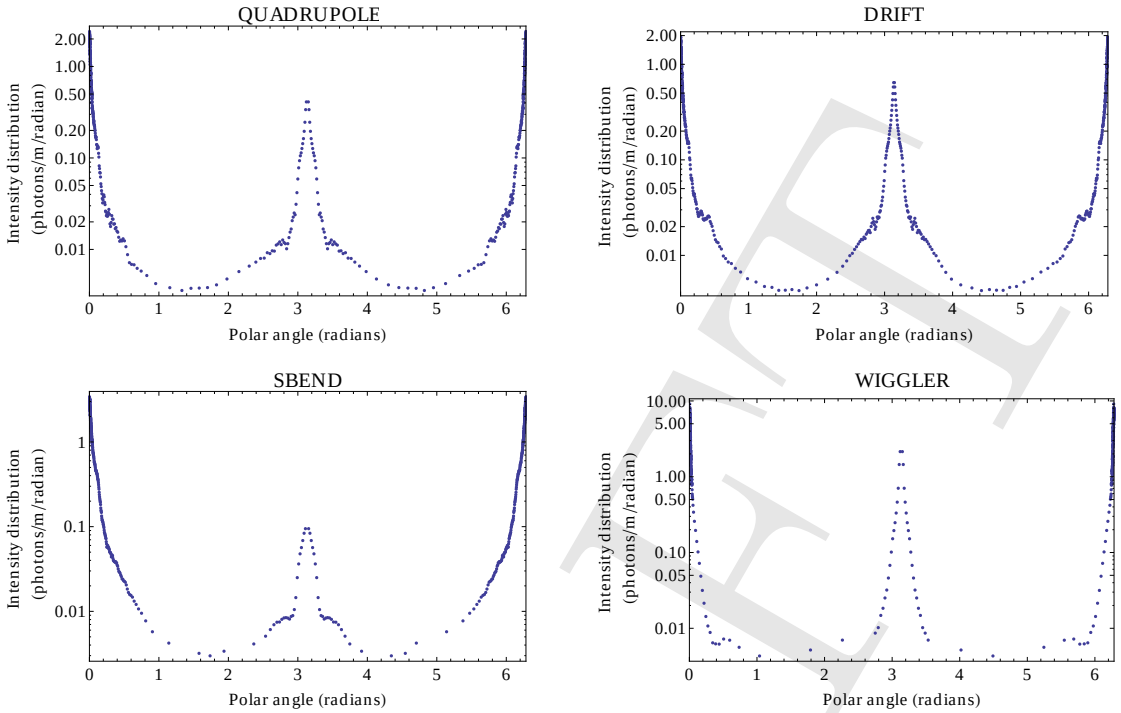

Figure 1.7: Photon intensity distribution (in photons/meter/radian) vs. polar angle (measured around the vacuum chamber, with zero angle corresponding to the radial outside direction), averaged over each type of magnetic environment. A realistic model for the CesrTA vacuum chamber throughout the ring is used. All scattering is specular. Top-bottom symmetry is assumed.

Example 3: Photon emission throughout the ring, realistic vacuum chamber, no diffuse scattering For the third example, photon emission throughout the CesrTA ring from a 2.1 GeV positron beam is simulated again, with a realistic vacuum chamber profile. The scattering is purely specular, as in the previous example.

In Fig. 1.7, we present the photon intensity distribution (in photons/meter/radian) vs. polar angle (measured around the vacuum chamber, with zero angle corresponding to the radial outside direction), averaged over each type of magnetic environment.

Compared to the previous example, the photon intensity on the top and bottom of the chamber (polar angles of $\pi/2$ and $3\pi/2$) is substantially suppressed, while the radiation striking the radial inside edge of the vacuum chamber (polar angle near π) is enhanced. This is primarily due to the local shape of the vacuum chamber at the strike point of the direct synchrotron radiation. For the elliptical chamber, the wall is curved at the radiation strike point, which, for a finite sized radiation stripe, enhances scattering out of the median plane. For the real CesrTA chamber, for most of the ring, the wall is vertical at the radiation strike point (see Figure **??**), so that scattering out of the median plane is limited.

Example 4: Photon emission throughout the ring, realistic vacuum chamber, diffuse scattering included. For the fourth example, photon emission throughout the CesrTA ring from a 2.1 GeV positron beam is simulated again, with a realistic vacuum chamber profile. In this case, diffuse scattering is included, using the parameters and model described in Sect. **??**.

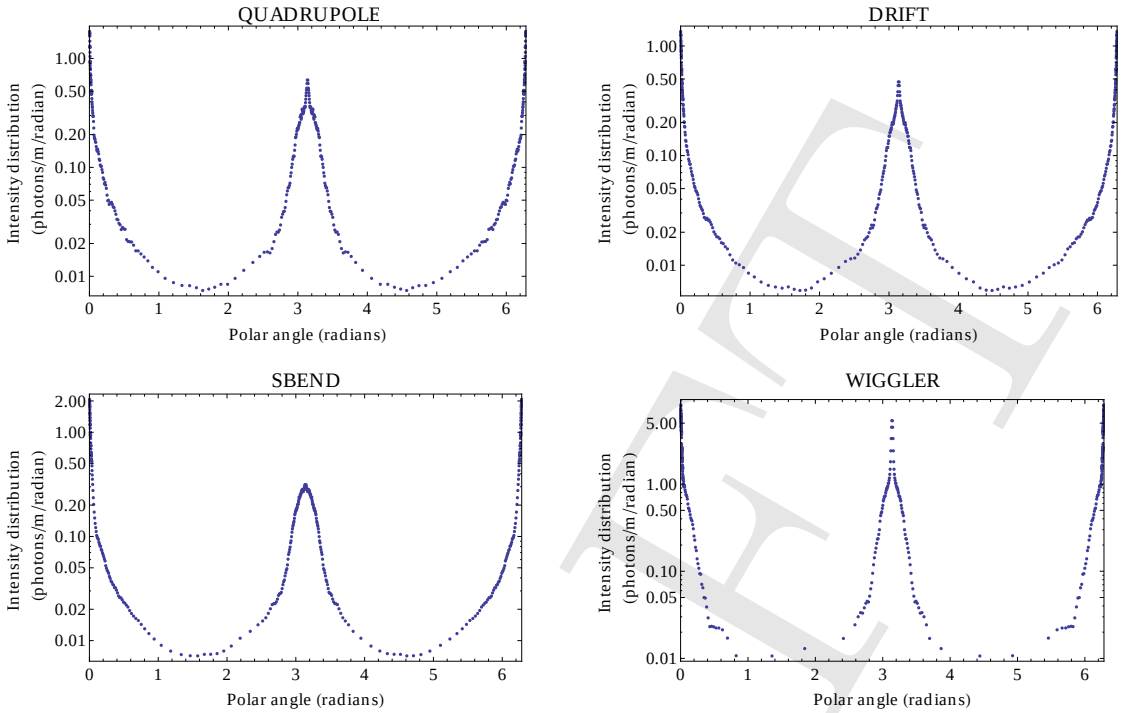

Figure 1.8: Photon intensity distribution (in photons/meter/radian) vs. polar angle (measured around the vacuum chamber, with zero angle corresponding to the radial outside direction), averaged over each type of magnetic environment. A realistic model for the CESR vacuum chamber throughout the ring is used, and diffuse scattering is included. Top-bottom symmetry is assumed.

In Fig. 1.8, we present the photon intensity distribution (in photons/meter/radian) vs. polar angle (measured around the vacuum chamber, with zero angle corresponding to the radial outside direction), averaged over each type of magnetic environment.

Compared to the previous example, the photon intensity on the top and bottom of the chamber (polar angles of $\pi/2$ and $3\pi/2$) is now much higher, and is comparable to that seen in Example 2. This is due to the out-of-plane diffuse scattering, which results in substantial amounts of radiation scattering out of the median plane. In addition, the radiation striking the radial inside edge of the vacuum chamber (polar angle near π) is also increased.

1.1.3.4 RFA Modeling

In principle, a single RFA voltage scan, in which data is collected while the retarding voltage is varied (see Section **??**), gives a great deal of information about the local behavior of the electron cloud. In practice, however, it is a highly nontrivial task to map a data point from a voltage scan to any physical quantity, such as cloud density. Typically, this gap is bridged through the use of cloud simulation programs, which track the motion of cloud particles during and after the passage of a bunch train (Section 1.1.3.1). Generally speaking, there are two ways to obtain a predicted RFA signal from a cloud simulation program: by postprocessing the output of the program, or by integrating an RFA model into the actual code. Both methods are discussed below.

Drift RFA Simulations The simplest method for simulating the output of an RFA for a given set of beam conditions is post-processing the output of a cloud simulation program, such as POSINST [34] or ECLOUD [39]. More specifically, these codes can output a file containing information on each macroparticle-wall collision, and one can perform a series of calculations on this output to determine what the RFA would have seen had one been present.

A basic postprocessing script does the following:

- Determine if the macroparticle has hit in the azimuthal region where one of the RFA collectors exists.
- Calculate an efficiency (probability of passing through the beam pipe hole) based on the incident angle and energy of the particle.
- Choose an energy "bin" for the particle based on its transverse energy.
- Deposit the final charge (equal to the macroparticle charge times the overall RFA efficiency) into the appropriate and collector and energy bin
- To replicate an RFA measurement at a given retarding voltage, add up all the signal in bins with higher energy than the voltage.

Note that by proceeding in this way one implicitly assumes that the presence of the RFA has no effect on the development of the cloud. This assumption is probably justified for a drift RFA, but may not be in the presence of a magnetic field. The latter case is discussed below.

Bench measurements of RFA efficiency have shown an enhancement of the signal at low retarding voltage due to the production of low energy secondary electrons inside the beam pipe holes [40]. An example bench measurement is shown in Fig. 1.9. It was taken using a monoenergetic beam of 200eV electrons, but shows a large increase in the signal at positive retarding voltage, where these low energy secondaries are guided into the RFA. We have developed a specialized particle tracking simulation to quantify this effect. It uses a monte carlo method to calculate the average efficiency for an incident electron, as a function of energy and angle, including beam pipe hole secondaries. Fig. 1.10 shows the effect of this enhancement for two different incident energies. This is included in the analysis as an additional charge added to the simulated RFA signal at zero retarding voltage. We are currently doing more rigorous bench measurements to fully quantify this effect.

In a drift region, qualitative agreement between data and (post-processed) simulation can generally be obtained without fine tuning of the simulation parameters. For example, Fig. 1.11 shows the measured and simulated (with POSINST [34]) RFA signal for voltage scan done under a typical set of beam conditions. The plots give collector signal as a function of collector number and retarding voltage. Here the data and simulation are similar both in general shape and magnitude. Getting closer quantitative agreement, however, requires a more systematic approach; see Section 1.1.4.2 for details.

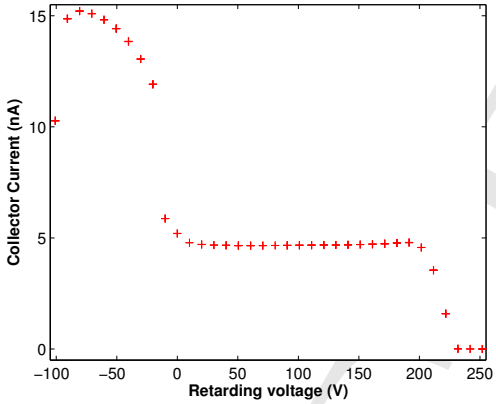

Figure 1.9: Bench measurement of RFA efficiency, showing an enhancement at low energy.

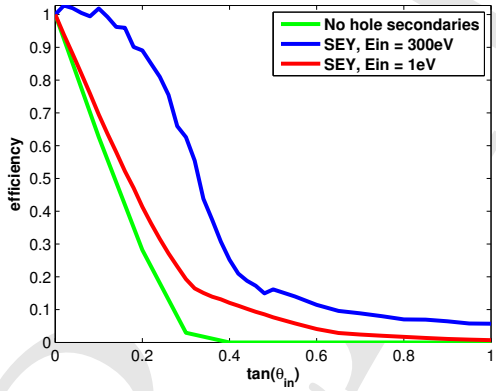

Figure 1.10: Simulated RFA efficiency vs incident angle, including secondary electrons produced in the beam pipe holes. The geometric efficiency (not including secondaries) is shown for comparison.

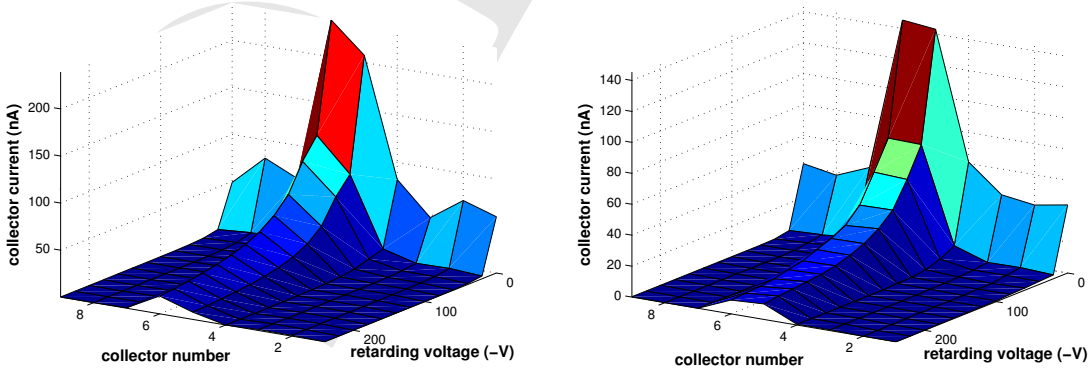

Figure 1.11: Comparison of data (left) and un-optimized simulation (right), Aluminum drift RFA. Beam conditions are 45 bunches of positrons at 1.25mA/bunch, 14ns spacing, 2.1GeV.

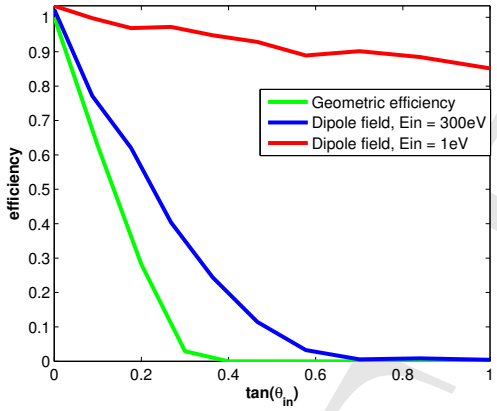

Figure 1.12: Simulated RFA efficiency vs incident angle for a CESR dipole RFA, with a 790G magnetic field. This corresponds to operation at 2.1GeV.

Dipole RFA Simulations Simulations have also been done for an RFA located inside a CESR dipole (see Section **??**), using the same method described above. Simulated efficiency curves for different incident energies are shown in Fig. 1.12. The simulation gives a very high efficiency for low energy electrons, due to their small cyclotron radius.

Fig. 1.13 shows a typical example of a simulation done for a dipole RFA. The results are again roughly consistent with the data, except at low energy ($V_{ret} = 0$). Here, the simulation significantly overestimates the signal observed by the RFA. One possible explanation for this discrepancy is an over-counting of the effect of individual macroparticles in the simulation. If a macroparticle collides with the vacuum chamber wall in the area covered by the RFA and creates a signal there, it should lose a corresponding amount of charge. However, this cannot be accomplished with a postprocessing method. In a dipole region, a single macroparticle will move up and down along the same field line, potentially striking the RFA area several times. The postprocessing script will treat each of these collisions separately, and obtain a spuriously high signal. This effect will be become worse as the macroparticle becomes more tightly constrained along the field line (i.e. as its cyclotron radius becomes smaller). So we expect it to be worse for low energy electrons (as in Fig. 1.13), and for high magnetic fields (as we will see in the section on wiggler simulations).

Quadrupole RFA Simulations Some preliminary simulations have been done for the quadrupole RFA installed in CESR. The simulations generally reproduce the behavior, discussed in section 1.1.4.1, where the majority of the signal is concentrated in one collector. Interestingly, they also give some indirect evidence that the cloud can become trapped in the quadrupole for long periods of time.

Fig 1.14 shows the signal in collector no. 10 for a voltage scan done with a 45 bunch train of positrons at 1mA/bunch. Also plotted are simulations done in ECLOUD [39] of these conditions. If one does a simulation for only one beam revolution period (2.56μs), the simulated signal is too low at all energies by over an order of magnitude. However, if one continues the simulation for multiple turns, one finds that the data and simulation start to get closer. By 19 turns, they are in very good agreement at high energy, and within a factor of 2 at low energy. This implies that the cloud is building up over several turns, and that the RFA is sensitive to this slow buildup.

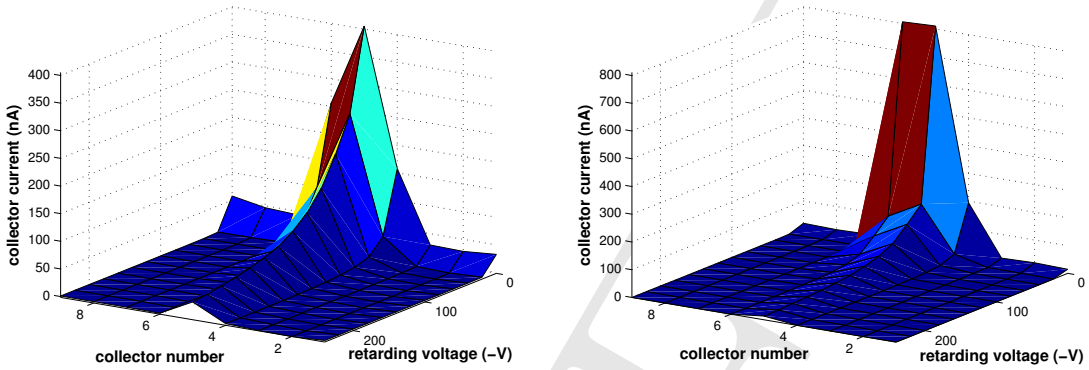

Figure 1.13: Comparison of data (left) and un-optimized simulation (right), Aluminum dipole RFA. Beam conditions are 45 bunches of positrons at 1.25mA/bunch, 14ns spacing, 2.1GeV.

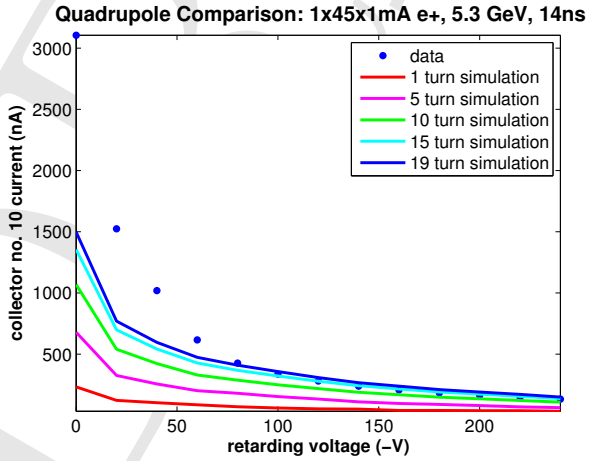

Figure 1.14: Quadrupole RFA simulation showing long term cloud buildup: 45 bunches, 1mA/bunch, e+, 5.3 GeV, 14ns

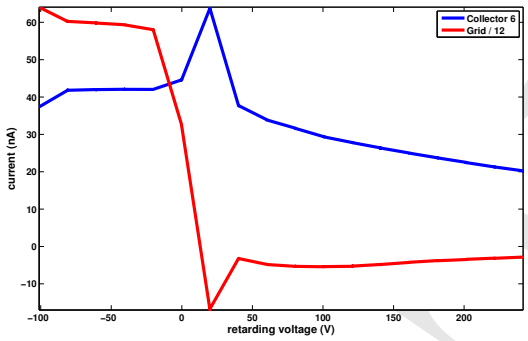

Figure 1.15: Resonant enhancement in wiggler data, 45 bunches, 1.25 mA/bunch, e+, 2.1GeV. Note that there are 12 collectors, so collector 6 is one of the central ones. Also note that the grid signal is divided by 12.

Wiggler RFA Simulations One major disadvantage of using a postprocessing RFA model is that one cannot accurately model any interaction between the RFA and the cloud. For an example of such an interaction, see Fig. 1.15. It shows a voltage scan done with an RFA in the center pole of a wiggler (approximated by a 1.9 T dipole field). Here one can see a clear enhancement in the signal at low (but nonzero) retarding voltage. Since the RFA should simply be collecting all electrons with an energy more than the magnitude of the retarding voltage, the signal should be a monotonically decreasing function of the voltage. So the RFA is not behaving simply as a passive monitor. Furthermore, the spike in collector current is accompanied by a corresponding dip in the grid current, suggesting that the grid is the source of the extra collector current.

We believe this spurious signal comes from a resonance between the bunch spacing and retarding voltage. To understand this, consider an electron which collides with the retarding grid and generates a secondary. Because electrons are so strongly pinned to the magnetic field lines in a 1.9T field, this electron is likely to escape through the same beam pipe hole that the primary entered. In other words, the motion of the electrons is approximately one-dimensional. An electron ejected from the grid will gain energy from the retarding field before it re-enters the vacuum chamber. If it is given the right amount of energy, it will be near the center of the vacuum chamber during the next bunch passage, and get a large beam kick, putting it in a position to generate even more secondaries. The net result is a resonance condition for the retarding voltage that is inversely proportional to the square of the bunch spacing, since the shorter the bunch spacing, the more kinetic energy an electron needs to arrive at the beam in time for the next bunch passage [41]. Fig. 1.16 shows that this dependence is (roughly) present in the data, though the low energy spike in the 4ns data is not predicted by this model.

Motivated by these measurements, we have incorporated into POSINST a model of the RFA geared toward reproducing the geometry of the devices installed in the vacuum chambers of the CesrTAwigglers. The motion of the electrons within the RFA, including the electrostatic force from the retarding field, is tracked using a special routine. The grid is modeled realistically, and secondary electrons can be produced there, with the same secondary yield model used for normal vacuum chamber collisions. The peak secondary electron yield and peak yield energy can be specified separately for the grid.

Because the actual retarding field is included in this model, the retarding voltage must be specified

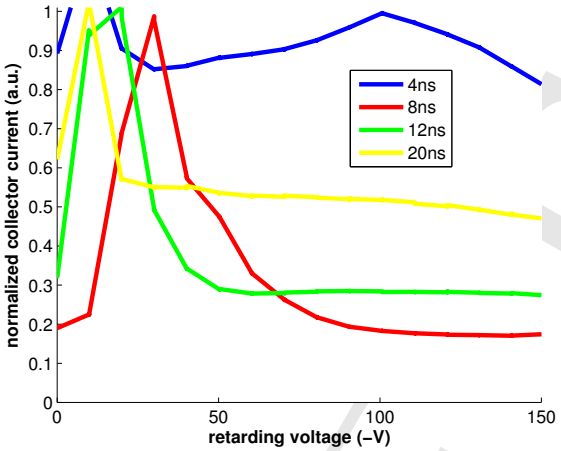

Figure 1.16: Resonant spike location at different bunch spacings, 1x45x1.25 mA e+, 5GeV. Only the signal in the central collector is plotted

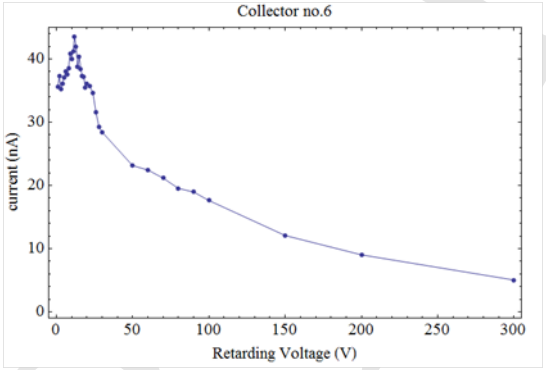

Figure 1.17: POSINST simulation showing resonant enhancement, 1x45x1.2 mA e+, 2.1GeV, 14ns, central collector

in the input file, and a separate simulation must be run for each voltage desired. Fig 1.17 shows the result of running this simulation for a series of different retarding voltages, for one set of beam conditions. Notably, the simulation reproduces the resonant enhancement seen in the data, at approximately the same voltage (10V for 14ns spacing).

The resonant enhancement is present in much of the wiggler data, so an integrated RFA model will be needed to obtain a more complete understanding of the cloud behavior in a wiggler magnet. This effect is also present to a lesser extent in our dipole data, indicating that a postprocessing model may not be sufficient there either.

1.1.4 EC Mitigation Observations and Comparison with Simulations

1.1.4.1 Measurements

We have used RFAs to probe the local behavior of the cloud in different magnetic field elements, and in the presence of different mitigation schemes. Table 1.1 gives a list of the various RFA types

Table 1.1: RFA styles deployed in CESR

Type	Magnetic Field	Grids	Collectors
APS	Drift	2	1
Insertable I	Drift	2	5
Insertable II	Drift	3	11
Thin	Drift, Dipole	1	9
SLAC	Dipole	3	17
Quad	Quadrupole	1	12
Wiggler	Wiggler	1	12

Table 1.2: Common beam conditions for electron cloud mitigation studies

Parameter	Typical Values	Units
Number of bunches	9, 20, 30, 45	-
Bunch current	.75, 1.25, 2.8, 3.8, 10	mA
Bunch spacing	4, 14, 280	ns
Species	Electron, positron	-
Beam energy	2.1, 4, 5.3	GeV

discussed in this section. Most of the data presented here is one of two types: "voltage scans," in which the retarding voltage is varied while beam conditions are held constant, or "current scans," in which the retarding grid is set to a positive voltage (typically 50V), and data is passively collected while the beam current is increased.

At CesrTA, we have been able to study the electron cloud under a wide variety of beam conditions, varying the number of bunches, bunch current, bunch spacing, beam energy, and species. As described in Section 1.1.4.2, this is very helpful for independently determining the photoelectron and secondary electron properties of the instrumented chamber. Table 1.2 lists some of the more common (but by no means only) beam parameters used for electron cloud mitigation studies with RFAs.

Drift Data Many of our earliest detailed measurements were done with "Insertable I" style RFAs (Table 1.1). Fig 1.18 shows an example of a voltage scan done with one of these RFAs, in typical CesrTAbeam conditions. It plots the RFA response as a function of collector number and retarding voltage. Roughly speaking this is a description of the transverse and energy distribution of the cloud. In this example, the signal is fairly broad across all five collectors, indicating that the cloud density is not strongly peaked around the beam. It also falls off quickly with retarding voltage, indicating that the majority of cloud particles have low energy. The RFA signal is expressed in terms of current density in nA/mm^2, normalized to the transparency of the RFA beam pipe and grids. In principle, this gives the time averaged electron current density incident on the beam pipe wall. The beam conditions are given as "1x45x1.25 mA e+, 14ns, 5.3 GeV." This notation, which will be used throughout this section, indicates one train of 45 bunches, with 1.25mA/bunch (1mA $= 1.6 \times 10^{10}$ particles), with positrons, 14ns spacing, and at beam energy 5.3GeV.

Fig 1.19 compares a current scan measurement done with two adjacent RFAs, one in a bare Copper chamber, and one in a TiN coated Copper chamber. Here we compare the average collector current density in the two detectors, as a function of beam current, and find that it is lower in the coated

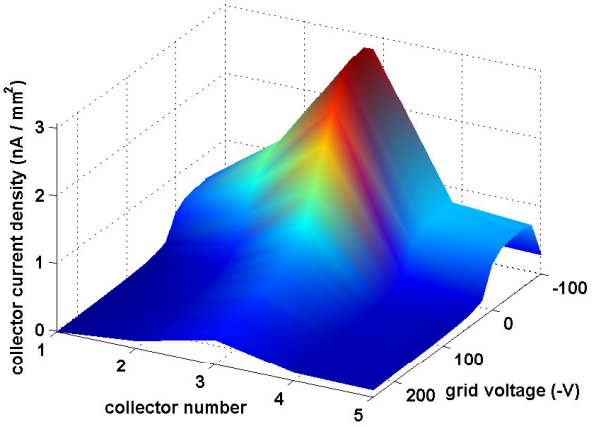

Figure 1.18: RFA voltage scan with an insertable segmented drift RFA in a Cu chamber, 1x45x1.25 mA e+, 14ns, 5.3 GeV

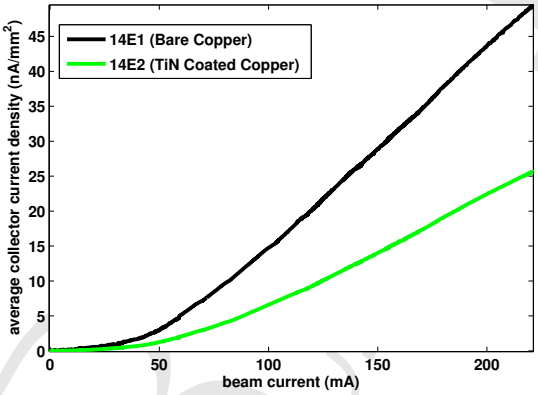

Figure 1.19: Comparison of insertable drift RFAs, 1x20 e+, 5.3GeV, 14ns

chamber by a factor of two.

"Thin" style RFAs (Table 1.1) were developed to fit inside the aperture of a CESR dipole, but they have also been deployed in drift regions. These RFAs have since been replaced by "Insertable II" style detectors, which have more collectors and can support higher voltages. Example measurements done with both of these RFA styles, in a TiN coated chamber, can be found in Fig. 1.20.

We have installed RFAs in arc drift sections adjacent to the 15E and 15W quadrupoles in CESR. The photon flux for a positron beam at 15W is about twice that of 15E, and vice versa for an electron beam. Measurements have been taken at both locations with TiN and amorphous carbon coatings, as well as with an uncoated aluminum chamber. In addition, a chamber with diamond-like carbon (DLC) coating has recently been installed at 15E. By comparing measurements taken at the same location in CESR, we ensure the comparisons can be made under identical beam conditions, including photon flux. Figs. 1.21 through 1.23 compare the RFA signal with each of these coatings for typical sets of CesrTAbeam conditions. We have generally found that data taken with 20 bunches of positrons at high current shows the biggest difference between the different chambers.

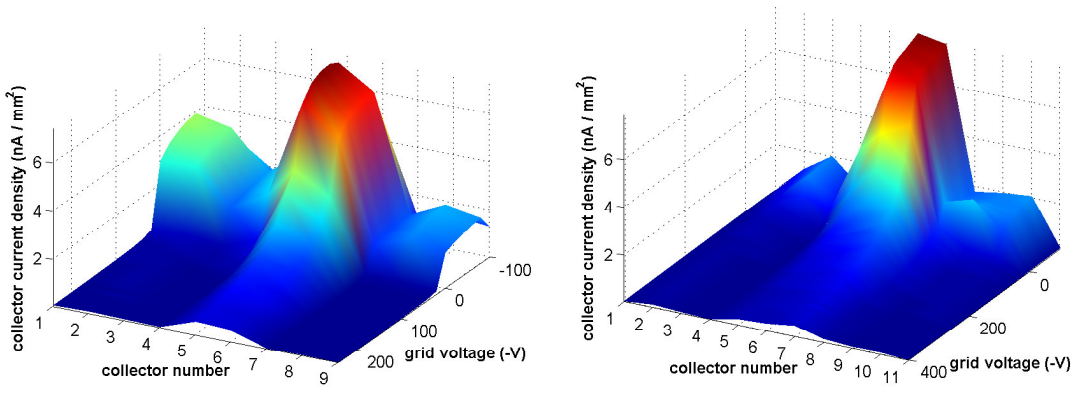

Figure 1.20: Example voltage scans with thin (left) and insertable (right) style drift RFAs in the same location. Both are TiN coated, beam conditions are 1x45x1.25mA, 5.3GeV, 14ns.

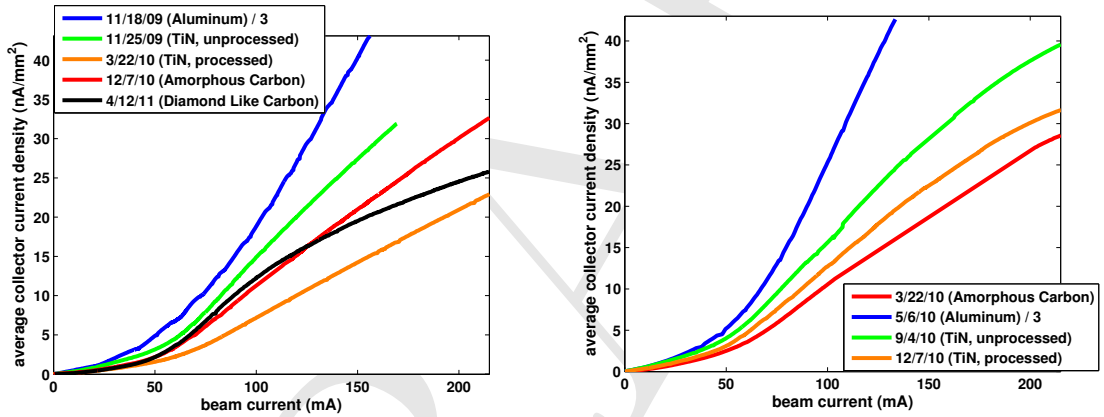

Figure 1.21: Comparison of different beam pipe coatings, 15E (left), and 15W (right) drift RFAs. Plots show average collector signal vs beam current for **20 bunches** of **positrons** with **14ns** spacing, at beam energy **5.3GeV**. Note that the aluminum chamber signals are divided by 3.

It is under these conditions that we expect to be most sensitive to the peak secondary electron yield (δ_{max}).

All coated chambers show a sizeable reduction in signal when compared to uncoated aluminum. After extensive processing, both TiN and amorphous carbon coated chambers show similar mitigation performance. The details of the small difference between 15E and 15W (where in one case TiN appears slightly better and in the other amorphous carbon does) require further analysis to understand fully.

Diamond-like carbon may perform better than other coatings at very high beam current. It should be noted that bench measurements of the Secondary Electron Yield (SEY) of DLC have found that the material can retain charge if bombarded with a sufficiently high electron flux, thus modifying the apparent SEY performance (Section 1.1.6). This effect may also be influencing the in situ measurements presented here.

We have also installed a NEG coated chamber in our L3 straight region. This chamber is in-

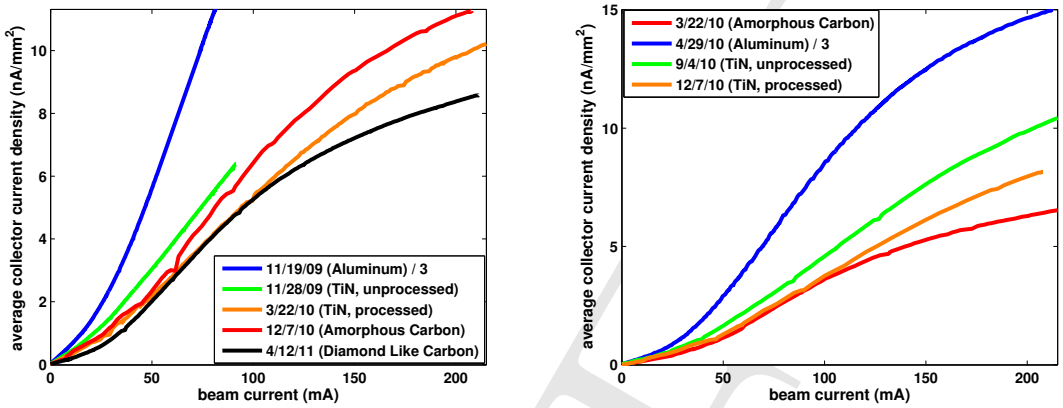

Figure 1.22: Comparison of different beam pipe coatings, 15E (left), and 15W (right) drift RFAs. Plots show average collector signal vs beam current for **20 bunches** of **electrons** with **14ns** spacing, at beam energy **5.3GeV**. Note that the aluminum chamber signals are divided by 3.

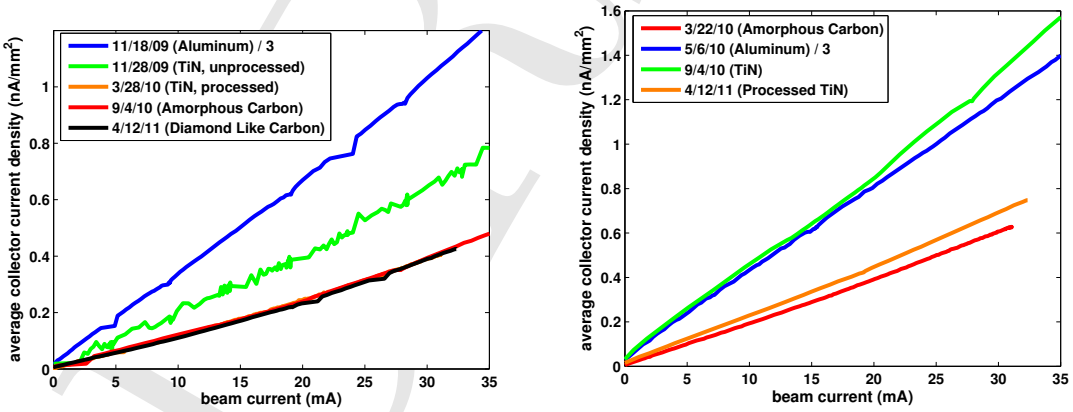

Figure 1.23: Comparison of different beam pipe coatings, 15E (left), and 15W (right) drift RFAs. Plots show average collector signal vs beam current for **9** equally spaced (**280ns**) bunches of **positrons**, at beam energy **5.3GeV**. Note that the aluminum chamber signals are divided by 3.

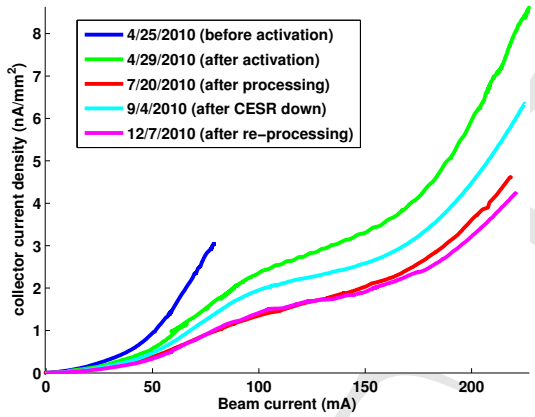

Figure 1.24: NEG RFA comparison, 1x20 e+, 5.3GeV, 14ns

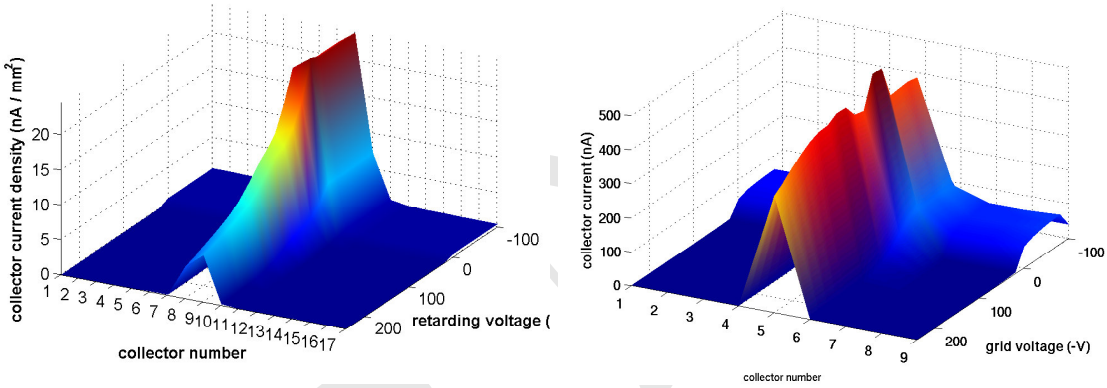

Figure 1.25: Typical Al dipole RFA voltage scans: 1x45x1.25mA e+, 5.3GeV, 14ns. Left: SLAC chicane RFA; Right: CESR dipole RFA

strumented with three single collector RFAs, located at different azimuthal positions. Fig. 1.24 compares the current measured by one of these RFAs on several different dates, corresponding to different states of activation and processing of the NEG coating. It was observed that both activation and initial processing reduced the signal measured by this RFA. After a CESR down (during which the NEG was activated again), the signal rose somewhat, but it processed back down to its minimum value after a few months of beam time. The other two detectors showed a similar trend.

Dipole Data RFA data have been taken in the presence of a dipole field, both in a standard CESR dipole (the "Thin" style in Table 1.1), and in a specially designed chicane which was built at SLAC [42]. The field in the chicane magnets is variable, but most of our measurements were done in a nominal dipole field of 810G. Of the four chicane chambers, one is bare Aluminum, two are TiN coated, and one is both grooved and TiN coated. The grooves are triangular with a depth of 5.6mm and an angle of 20°. Fig. 1.25 shows a retarding voltage scan done with both the CESR dipole and Aluminum chicane RFAs. In both cases, one can see a strong multipacting spike in the central collector.

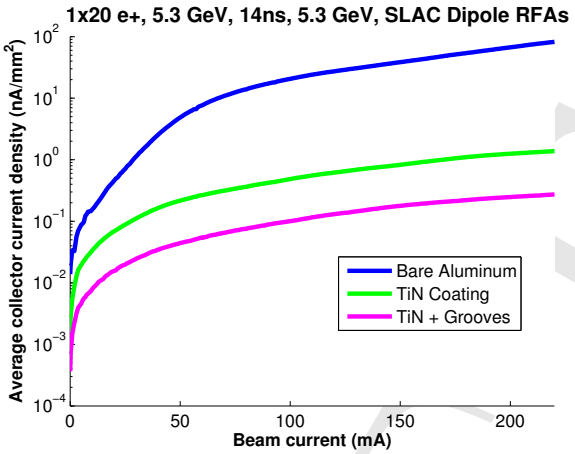

Figure 1.26: Dipole RFA mitigation comparison, 1x20 e+, 5.3GeV, 14ns

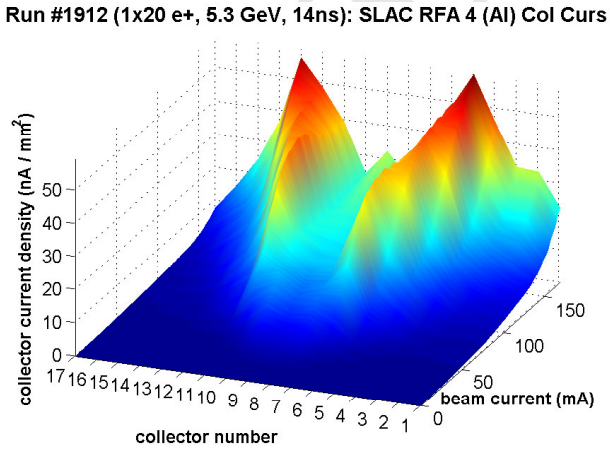

Figure 1.27: Bifurcation of peak cloud density in a Al dipole: 1x20 e+, 5.3GeV, 14ns

Fig. 1.26 shows a comparison between three of the chicane RFAs. We found the difference between uncoated and coated chambers to be even stronger than in a drift region. At high beam current, the TiN coated chamber shows a signal smaller by two orders of magnitude than the bare Al chamber, while the coated and grooved chamber performs better still.

For high bunch currents, we have observed a bifurcation of the central multipacting peak into two peaks with a dip in the middle. This is demonstrated in Fig 1.27, which shows the signal in all 17 RFA collectors vs beam current. Bifurcation occurs when the average energy of electrons in the center of the beam pipe is past the peak of the SEY curve, so that the effective maximum yield is actually off center. The higher the bunch current, the further off center these peaks will be.

By varying the strength of the chicane magnets, we can also study the behavior of the cloud at different dipole magnetic field values. Fig. 1.28 shows an example of RFA data taken as a function of magnetic field strength. The most prominent feature of the data is regularly occurring spikes or dips in all three plotted chambers. These correspond to "cyclotron resonances," which occur whenever the cyclotron period of cloud electrons is an integral multiple of the bunch spacing [43]. For 4ns bunch spacing we expect them every 89 Gauss, which is what is seen in the data. Another

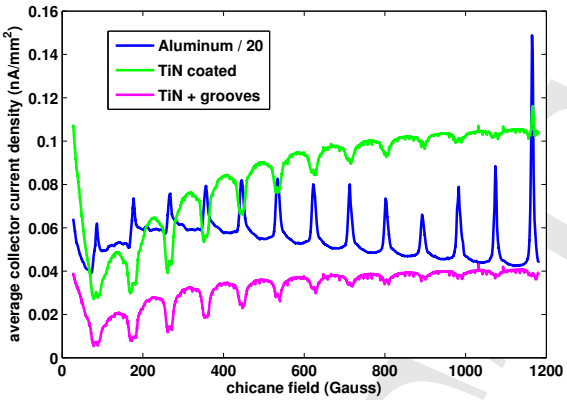

Figure 1.28: RFA signal as a function of chicane magnetic field: 1x45x1mA e+, 5GeV, 4ns. Cyclotron resonances are observed every 89G. Note that the Aluminum chamber signal is divided by 20.

interesting feature of this measurement is that these resonances appear as peaks in the RFA signal in the Aluminum chamber, but as dips in the coated chambers. This aspect of the data is discussed below.

Because the properties of the electron cloud can change over the course of nanoseconds, it is interesting to investigate its behavior as a function of bunch spacing. At CesrTAwe have taken RFA data with bunch spacings varying from 4ns to 112ns.

Fig. 1.29 shows the signal in the central collector of two dipole RFAs as a function of bunch spacing. The left plot is for the Aluminum SLAC chicane RFA; the right is for the CESR dipole RFA (see Fig. 1.25). The SLAC chamber has a half-height of 4.4cm, while the CESR RFA has a half-height of 2.5cm.

For the SLAC RFA, we observe two distinct peaks in the positron data, at approximately 14ns and 60ns. The electron beam data shows almost no signal before 36ns, and is peaked around the same place as second the positron peak. The enhancement of the signal at 60ns could be due to a resonance between the bunch spacing and the cloud development (often called a "multipacting resonance"). This effect will be enhanced by the dipole field, which renders the motion of the electrons mostly one dimensional.

A very simple model for a multipacting resonance is that if the time for a typical secondary electron to travel to the center of the beam pipe is equal to the bunch spacing, this electron will be kicked strongly by the beam, and is likely to produce more secondary electrons. In reality, peak secondary production will occur when this electron is given an amount of energy corresponding to the peak of the SEY curve. However, for aluminum the SEY is greater than 1 well into the keV range, so an electron anywhere near the beam is a candidate to produce more secondaries. Thus we expect the "resonance" to be somewhat broad.

If we ignore the time for the kicked electron to travel to the beam pipe wall (which will be small if the kick is strong), the resonance condition is simply $t_b = a/v_{sec}$, where t_b is the bunch spacing, a is the chamber half-height (i.e. the distance from the wall to the beam), and v_{sec} is a characteristic secondary electron velocity. For a 1.5eV electron, this peak will occur at 61ns. The fact that there is a finite width to the secondary energy distribution will further smear out the peak.

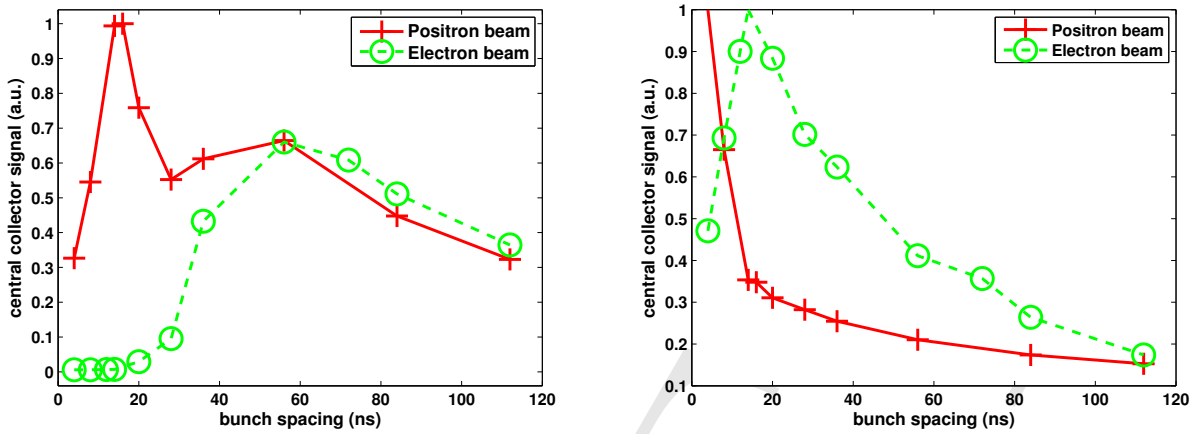

Figure 1.29: Central collector signal in a dipole RFA as a function of bunch spacing, for a 20 bunch train with 3.5mA (5.6×10^{10} particles) per bunch, at 5.3 GeV. Left: SLAC chicane RFA, right: CESR dipole RFA

The lower energy peak in the positron data could be a higher order multipacting resonance, where it takes two bunches to set up the resonance condition. Here we consider the case where the first bunch gives some additional energy to the electron, so that it makes it to the center of the chamber in time for the second bunch. If we again neglect the time for the kicked electron to reach the beam pipe wall, the resonance condition becomes:

$$t_{b,2} = \frac{a-r_1}{v_{sec}} = \frac{r_1}{v_2} \tag{1.1}$$

$$v_2 = v_{sec} + \frac{2cN_b r_e}{r_1} \tag{1.2}$$

Here r_1 is the distance from the electron to the beam during the first bunch passage, v_2 is the velocity of the electron after it is kicked by the first bunch, N_b is the bunch population and r_e is the classical electron radius. Solving for $t_{b,2}$ gives us Eq. 1.3, where we have defined $k \equiv 2cN_b r_e$.

$$t_{b,2} = \frac{k + 3av_{sec} - \sqrt{k^2 + 6kav_{sec} + a^2 v_{sec}^2}}{4v_{sec}^2} \tag{1.3}$$

For a 1.5eV secondary electron, $t_{b,2}$ is 11ns, somewhat less than the 14ns that is observed. A more sophisticated model (which would include, among other things, the time for the kicked electron to reach the wall) may yield a more accurate result. Note that this resonance condition applies only to positron beams, so only one peak is predicted for the electron data (which is what we find). Overall, a multipacting scenario with a 1.5eV peak secondary energy is approximately consistent with the SLAC chicane data, for both the positron and electron beam data.

The predictions for our CESR dipole (Fig. 1.29, right) would then be $t_b = 34$ns and $t_{b,2} = 4$ns. The former is higher than what is observed, though the latter is consistent with the data. A better fit would be for an 8eV electron, then $t_b = 15$ns and $t_{b,2} = 3$ns. It is also possible that a more sophisticated model would fit the CESR dipole data better.

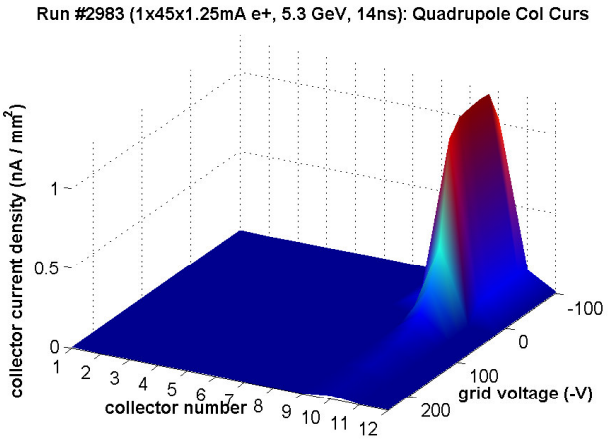

Figure 1.30: Quadrupole RFA voltage scan: 1x45x1.25mA e+, 5.3GeV, 14ns

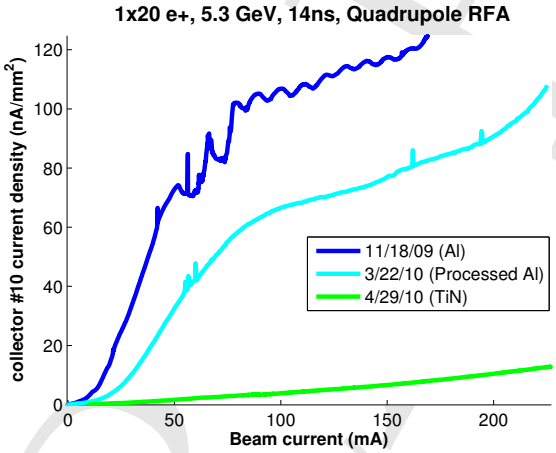

Figure 1.31: Quadrupole mitigation comparison, 1x20 e+, 5.3GeV, 14ns

Quadrupole Data Another development at CesrTAhas been the incorporation of an RFA into a quadrupole chamber. This RFA wraps azimuthally around the chamber, from about 70 to 150 degrees (taking zero degrees to be the source point). A typical quadrupole RFA measurement is shown in Fig. 1.30. We find that the collector that is lined up with the quad pole tip (no. 10) sees a large amount of current, while the rest of the collectors see relatively little. This suggests that the majority of the cloud in the quad is streaming between two pole tips.

Fig. 1.31 shows a comparison of a bare Aluminum (both processed and unprocessed) quadrupole chamber with the TiN coated chamber that has replaced it. In this comparison only collector 10 is being plotted. The signal in the TiN chamber was found to be reduced by well over an order of magnitude.

One potential side effect of the cloud mirroring between the quad pole tips is that it may become trapped for a long time. As seen in Fig. 1.32, for a positron beam we do not observe a strong dependence on bunch spacing, though there does seem to be a modest enhancement around 14ns. The data for an electron beam is even more surprising, actually showing a monotonic increase with bunch spacing. Both of these measurements point to a timescale for cloud development in the quad

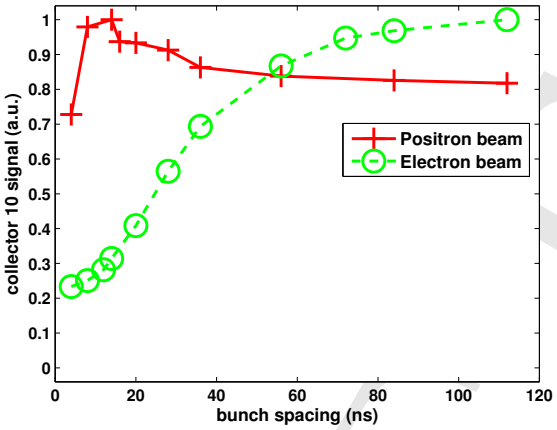

Figure 1.32: Signal in a quadrupole RFA as a function of bunch spacing, for the same beam conditions as in Fig. 1.29. The collector which is in line with the quad pole tip is plotted.

that is much longer than 100ns.

Wiggler Data The L0 straight section of CESR has been reconfigured to include six superconducting wigglers, three of which are instrumented with RFAs (see Section **??**). Each wiggler has three RFAs: one in the center of a wiggler pole (where the field is mostly transverse), one in between poles (where the field is mostly longitudinal), and one in an intermediate region. Fig. 1.33 shows a typical voltage scan done in the center pole RFA of a Cu wiggler chamber, for a 45 bunch train of positrons at 1.25mA/bunch, 14ns spacing, and 2.1 GeV. The signal is fairly constant across all the collectors at low retarding voltage, but does become peaked at the center at high energy. There is also an anomalous spike in current at low (but nonzero) retarding voltage; we believe this is due to a resonance between the bunch spacing and retarding voltage (see Section 1.1.3.4).

As with the drift RFAs, cycling the location of the different wigglers has allowed us to compare the RFA response with different mitigation techniques at the same longitudinal position in the ring. We have tested chambers with bare Copper, TiN coating, triangular grooves, TiN coating on grooves, and a clearing electrode. Fig. 1.34 shows an example voltage scan from the grooved chamber; it is interesting to note that the RFA is sensitive to the grooved structure. The grooves have 2mm depth and 20° angle.

Fig. 1.35 compares the average collector current (in the center pole RFA) vs beam current for different mitigation schemes, at both the 2WA and 2WB locations. These locations have slightly different photon fluxes, but as the TiN coated chamber has been installed in both, it can be used (roughly) as a reference. Note that TiN coating by itself does not appear to lead to a reduction in the wiggler RFA current relative to bare copper. Grooves do lead to an improvement, and TiN coated grooves are better still. The chamber instrumented with a clearing electrode shows the smallest signal by a wide margin, improving on TiN by approximately a factor of 50. The electrode was set to 400V for this measurement.

Very little dipole radiation is expected to reach the downstream vacuum chambers in the L0 straight, but they will be illuminated by radiation from the wigglers. Therefore, by varying the field in the wiggler magnets, we can vary the number of photons striking the wall at a given point along

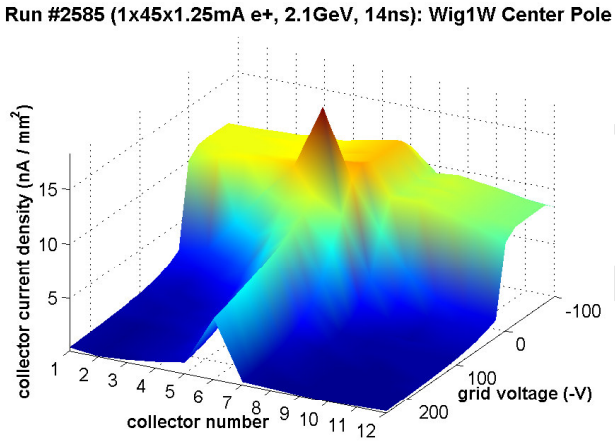

Figure 1.33: Cu wiggler RFA measurement: 1x45x1.25mA e+, 2.1GeV, 14ns

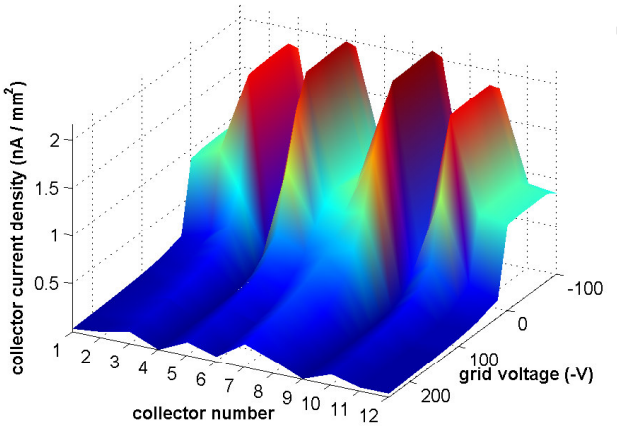

Figure 1.34: Grooved wiggler RFA measurement: 1x45x1.25mA e+, 2.1GeV, 14ns

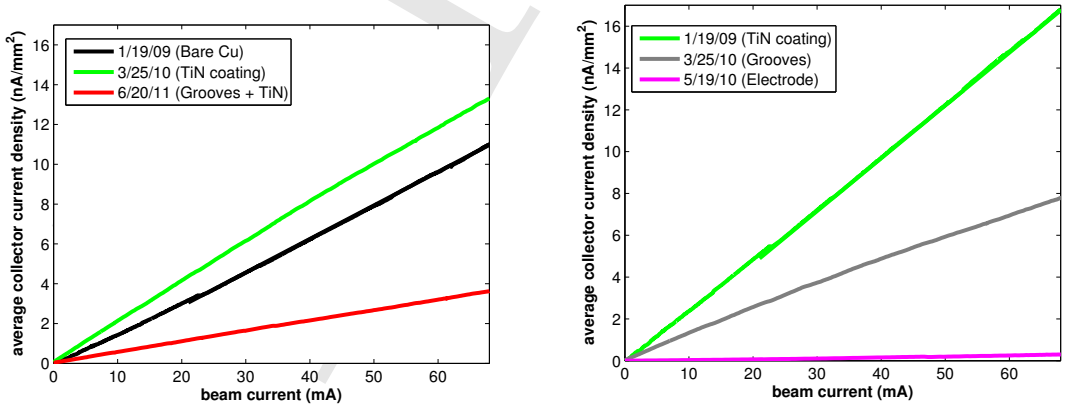

Figure 1.35: Wiggler RFA mitigation comparison: 1x45 e+, 2.1GeV, 14ns. Left: 2WA location, right: 2WB location. The 2WB location is further downstream in the wiggler straight, and therefore has a slightly higher photon flux.

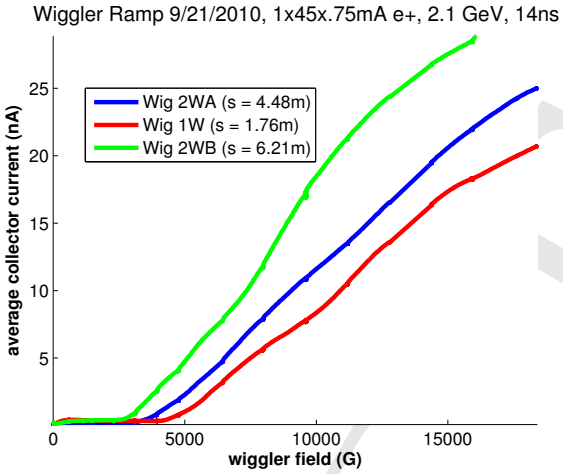

Figure 1.36: Wiggler ramp measurement: 1x45x.75mA e+, 2.1GeV, 14ns

the straight. This will also vary the number of photoelectrons produced there, so electron cloud diagnostic devices located in L0 can provide an indirect measurement of the properties of the wiggler photons.

Fig. 1.36 shows the signal in three center-pole wiggler RFAs as a function of wiggler field strength. We observe a "turn on" of the signal in each detector at a specific wiggler field value. Note that the detectors that are further downstream (i.e. those with a higher s value) turn on first. This is because as the wiggler field is increased, the radiation fan becomes wider. The farther downstream a detector is, the less wide the fan must be for photons to hit at that location. This measurement can help us understand the scattering of photons in L0, since only photoelectrons produced on the top or bottom of the beam pipe can initiate the build-up of the part of the cloud detected by the RFA.

During normal operation, essentially no signal is observed in longitudinal field detectors, because there are no electrons with sufficient energy to cross the field lines. Fig. 1.37 shows the signal in a longitudinal field RFA (in the uncoated Copper wiggler), as a function of magnetic field strength. The signal is effectively gone by 1000 Gauss, well below the 1.9T full field value.

Mitigation Summary In terms of the effectiveness of mitigation types, several qualitative comments can be readily made:

- We have found beam pipe coatings (TiN, amorphous carbon, diamond-like carbon, and NEG) to be effective at mitigating the cloud in drifts.
- TiN coating was also found to be effective in a dipole and quadrupole; using a grooved and coated chamber in a dipole is even more effective.
- In a wiggler, a clearing electrode appears to be the most effective mitigation technique.

A systematic study to obtain more quantitative information about the different chambers, in particular their primary and secondary electron yield properties, is discussed in the next section.

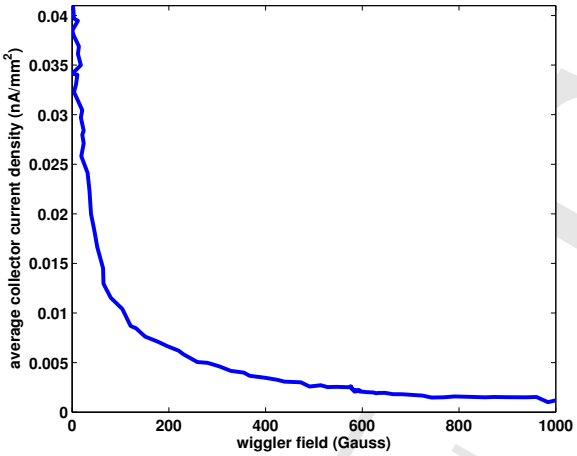

Figure 1.37: Wiggler ramp measurement in longitudinal field region: 1x45x.75mA e+, 2.1GeV, 14ns

1.1.4.2 Comparison with Simulation

The large quantity of RFA data obtained during the CesrTAprogram necessitates a systematic method for detailed analysis. The goal is, given a set of voltage scan data, to find a set of simulation parameters that bring data and simulation into as close to agreement as possible.

A chi squared analysis has been employed to accomplish this. In short, we want to minimize χ^2, as defined in Eq. 1.4. Here $\mathbf{y}$ a vector containing the difference between the data and a nominal simulation, $\mathbf{X}$ is the Jacobian matrix, and β is the a vector contiaing the change in each of the parameters under study. $\mathbf{W}$ is a diagonal matrix whose elements are $\frac{1}{\sigma_i^2}$, where σ_i is the error on data point i. Note that both the data and simulation can contribute to this error. The value of β which will minimize χ^2 is given in Eq. 1.5. Once a new set of parameter values is obtained, the process can be repeated with this new set as the "nominal" values. This method will generally need to be iterated a few times before it converges on the actual minimum value of χ^2.

$$\chi^2 = (\mathbf{y} - \mathbf{X}\,\beta)^T\,\mathbf{W}\,(\mathbf{y} - \mathbf{X}\,\beta) \tag{1.4}$$

$$\beta = (\mathbf{X}^T\,\mathbf{W}\,\mathbf{X})^{-1}\,\mathbf{X}^T\,\mathbf{W}\,\mathbf{y} \tag{1.5}$$

There are many subtleties in the precise definitions of the terms in Eq. 1.5. For the RFA analysis, the points in the vector $\mathbf{y}$ come from voltage scan data. To determine the parameters independently, one should use several different voltage scans, which cover a wide range of beam conditions. Since a voltage scan is actually a measurement of the integrated energy spectrum, once should differentiate the signal to obtain a set of independent data points. These points may not individually have enough signal to be meaningful, so one can group them together (i.e. make energy "bins" of varying width) to get one element of the $\mathbf{y}$ vector.

The choice of which simulation parameters to fit is also essential. There are many parameters that characterize the production of secondary electrons in POSINST [34], but a few stand out as being

especially important. Among them are:

- **dtspk**, the peak true secondary electron yield
- **P1epk**, the low energy elastic yield
- **P1rinf**, the rediffused yield at infinity
- **E0epk**, the energy at which peak secondary production occurs
- **powts**, the "shape parameter," which determines the rise and fall of the SEY curve
- **pangsec**, the angular distribution of secondary electrons
- **enpar** and **pnpar**, which determine the energy distribution of secondary electrons

In general, primary photoelectrons are less well understood than secondary electrons. Some important primary emission parameters include:

- **queffp**, the quantum efficiency
- **ek0phel** and **eksigphel**, the peak energy and width of the photoelectron energy distribution
- **refleff**, the photon reflectivity

Generally speaking, **dtspk** and **queffp** need to be included in the fitting procedure to get good agreement with the RFA data. Other strong parameters include **P1epk**, **P1rinf**, and **powts**, but they are highly correlated with each other (i.e. have similar effects on the RFA simulation), so only one of the three is needed.

The starting points for several SEY parameters (**dtspk**, **E0epk**, **powts**), were chosen based on fits to the in-situ SEY measurements in CESR (Section 1.1.6).

We have found that in order to have any RFA signal for a high current electron beam, one needs to produce some high energy photoelectrons. Currently this is accomplished by using a Lorentzian photoelectron energy distribution (rather than the default Gaussian distribution), with a low peak energy (**ek0phel** = 10eV), but a large width (**eksigphel** = 150 eV). However, the drift RFA data does not seem to constrain the exact shape of the distribution. Measurements with a shielded pickup detector (Section 1.2.2) provide a method to probe these parameters in more detail.

The photon flux and reflectivity at the RFA are fixed, based on a 3 dimensional simulation of photon production and reflection in the CesrTAvacuum chamber (Section **??**). Photoelectron parameters were allowed to be different for different beam energies and species, because the photon energy spectrum at any given location in CESR will be different for the two species. Plans are underway

Table 1.3: List of beam conditions used for one round of fitting, and which parameter(s) they help determine

Bunches	Bunch current	Species	Bunch Spacing	Beam Energy	Parameter(s)
45	2.3	e+	14	2.1	dtspk
20	2.8	e+	4	4	dtspk
20	7.5	e+	14	2.1	dtspk
20	2.95	e+	14	4	dtspk
45	2.67	e+	14	5.3	dtspk
45	1.25	e+	4	5.3	dtspk
45	2.89	e-	4	5.3	dtspk, queffp
20	2.6	e-	14	2.1	queffp
45	0.8	e-	14	5.3	queffp
45	0.75	e+	14	5.3	queffp
45	0.75	e-	14	2.1	queffp, P1epk
9	3.78	e+	280	2.1	queffp, P1epk
45	0.75	e+	14	4	queffp, P1epk
9	3.78	e-	280	2.1	P1epk
9	3.78	e-	280	5.3	P1epk
9	3.78	e+	280	4	P1epk
9	4.11	e+	280	5.3	P1epk

to develop a model for photoelectron production which takes into account the energy of the incident photon.

In order to get a good fit to the data, one should choose parameters which have a strong effect on the simulations, and are relatively independent of each other. We have found that a reasonable fit can be obtained with as little as three parameters- typically the true secondary yield (**dtspk**), elastic yield (**P1epk**), and quantum efficiency (**queffp**). The true secondary yield has the strongest effect on data taken with short bunch spacings, high bunch currents, and positron beams. The elastic yield, meanwhile, is best determined by data with large bunch spacing, while the quantum efficiency prefers low beam current. Table 1.3 gives a list of data sets used in one round of fitting, and indicates which parameter is most strongly associated with it.

Several sources of error must be taken into account when constructing the error matrix (**W** in Eq. 1.4). They include:

- Noise in the measurements (typically quite small)
- Statistical errors in simulations. This is a major source of error. It can be reduced by increasing the number of macroparticles used in the simulation, at the cost of increased the run time.
- A general error of 10% was added to account for systematic uncertainties in the data. One such uncertainty is unevenness in bunch currents along the train, which is not accounted for in the simulation.
- We have observed a slow drift of baseline (zero current value) in measurements, on the order of $\sim 2\%$ of full scale. This amounts to $\sim$20nA on the lowest gain setting, and $\sim$.02nA on the highest one.

- An extra 20% error was added to signal in the simulation caused by beam pipe hole secondaries, to account for uncertainty in the modeling of this phenomenon.
- Since the gradient for Jacobian matrix ($\mathbf{X}$) is determined by simulation, it will also have an associated error. This cannot be included in the $\mathbf{W}$ matrix, because it will be different for each parameter. However, it can still be calculated, and its effect on the final parameter errors can be estimated.

We have found that, in general, one can obtain a reasonable fit to the data with only three (well chosen) parameters. As mentioned above, one good set consists of the true secondary yield, elastic yield, and quantum efficiency. Using more parameters does allow for a slightly better fit, at the cost of uniqueness and clarity.

Fig. 1.38 shows some of the results of the parameter finding method for an uncoated aluminum drift chamber. The plots compare the data and simulation for the signal across the 9 RFA collectors at three different retarding voltages. Overall there is good agreement between data and simulation for a wide variety of beam conditions.

In principle, errors on the final parameter values are readily obtainable during the course of the analysis. The covariance matrix for the parameters is $(\mathbf{X}^T \mathbf{W} \mathbf{X})^{-1}$. Standard errors on each parameter can be derived from the diagonal elements of the covariance matrix, and the correlations between each parameter from the off-diagonal elements. However, it should be noted that this analysis will only seek out the nearest local minimum in parameter space. It is always possible that a better fit can be achieved with a different set of values, especially if one uses many parameters in the fit. Therefore, these errors should be understood as the width of the local minimum, rather than an absolute determination of the uncertainty in the parameter. Nonetheless, the ability of this method to achieve a good fit for data taken under a wide variety of beam conditions strongly implies that the PEY and SEY models used are reproducing reality to a reasonable degree.

The best fit values and confidence intervals for an Aluminum chamber are shown in Table 1.4. This chamber was installed in the 15W location (see Section 1.1.4.1), and the fit used the data taken during May 2010 (listed in Table 1.3). The values listed for the error bars also include an estimate of the uncertainty introduced by errors in the Jacobian matrix, which is added in quadrature to the standard error. Table 1.5 lists the best fit values for the 15E amorphous Carbon coated chamber, using the same data sets. Finally, Table 1.6 gives the values for a TiN coated chamber, installed at 15W during December 2010. As mentioned above, the starting point for all the listed SEY parameters were taken from fits to measured in-situ data. It is worth noting that this analysis indicates a very low secondary yield for both coated chambers.

One somewhat strange result of this analysis is that the quantum efficiency at 2.1GeV was found to be quite low for positron beams at 15E, and electron beams at 15W. The value for the other species, and for 4 and 5.3GeV, are all consistent with each other. The anomalous value is quoted separately from the other best fit values. This discrepancy appeared for both the 15W Al chamber and the 15E carbon coated chamber (it did not appear for the 15W TiN chamber, because no 2.1GeV electron beam data was used in the fit). It is most likely a reflection of the incompleteness of our photon and photoelectron modeling.

Summary A systematic method for fitting RFA simulation to data has been presented, and best fit values for PEY and SEY parameters of some materials have been given. Future work on this topic includes:

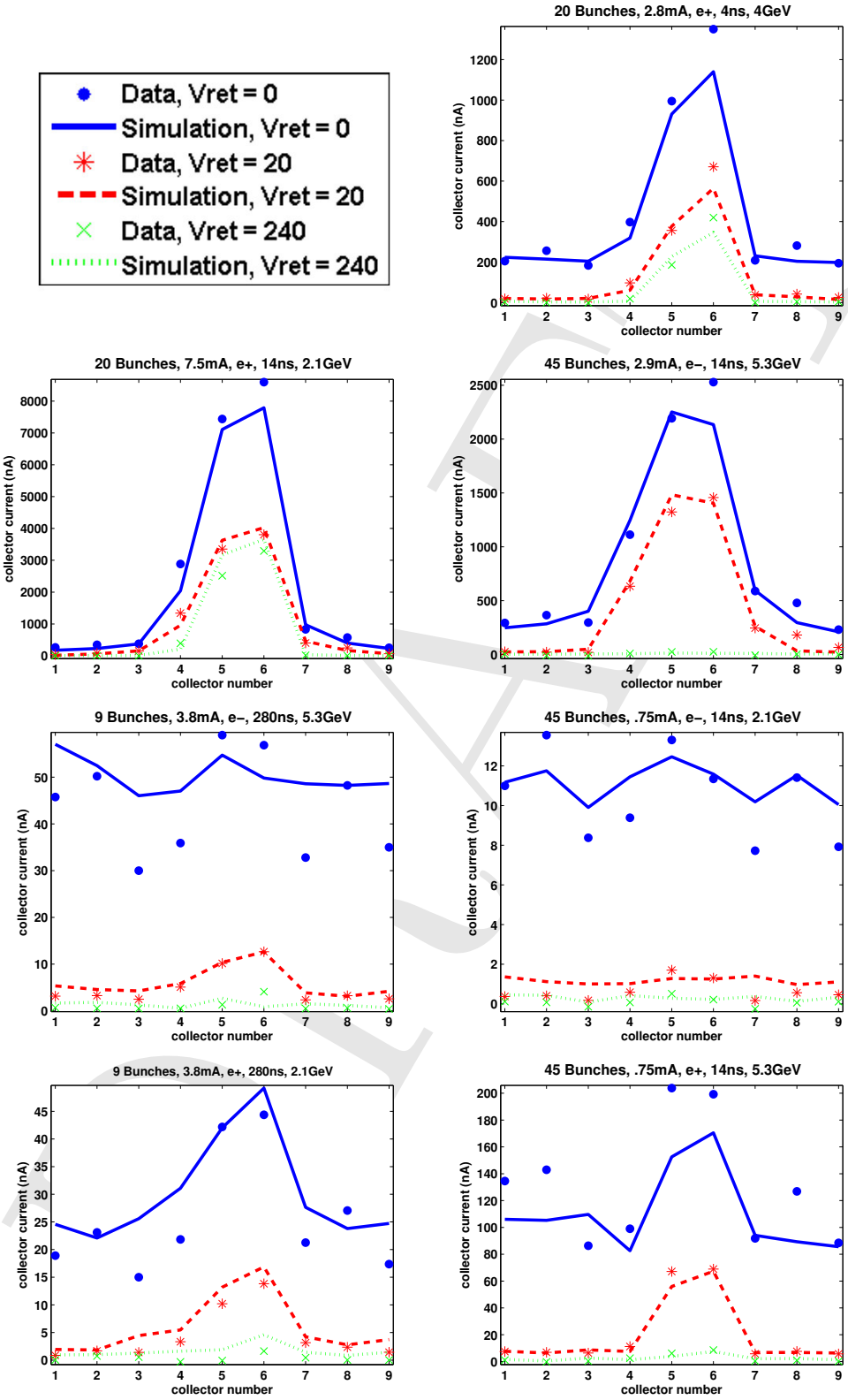

Figure 1.38: Comparison of RFA data and simulation, using best fit parameters. The plots show the signal across the 9 RFA collectors at three different retarding voltages.

Table 1.4: Best fit parameters- 15W aluminum chamber

Parameter	Description	Base Value	Final Value
dtspk	Peak true secondary yield	1.37	1.74 ± .02
P1epk	Elastic yield at E = 0	.5	.43 ± .01
P1rinf	Rediffused yield at E = ∞	.2	.2
E0epk	Peak yield energy	280eV	280eV
powts	Shape parameter	1.54	1.54
queffp	Quantum efficiency, 2.1 GeV, e-	.1	.034 ± .004
queffp	Quantum efficiency, other	.1	.111 ± .006

Table 1.5: Best fit parameters- 15E amorphous carbon coated chamber

Parameter	Description	Base Value	Final Value
dtspk	Peak true secondary yield	.76	.55 ± .02
P1epk	Elastic yield at E = 0	.5	.29 ± .02
P1rinf	Rediffused yield at E = ∞	.2	.2
E0epk	Peak yield energy	300eV	300eV
powts	Shape parameter	1.77	1.77
queffp	Quantum efficiency, 2.1GeV, e+	.1	.021 ± .003
queffp	Quantum efficiency, other	.1	.081 ± .017

Table 1.6: Best fit parameters- 15W TiN coated chamber

Parameter	Description	Base Value	Final Value
dtspk	Peak true secondary yield	.73	.54 ± .01
P1epk	Elastic yield at E = 0	.5	.36 ± .01
P1rinf	Rediffused yield at E = ∞	.2	.2
E0epk	Peak yield energy	370eV	370eV
powts	Shape parameter	1.32	1.32
queffp	Quantum efficiency	.1	.068 ± .007

- Repeating the analysis for other surface types
- Repeating the analysis for RFAs in magnetic fields, including dipoles, quadrupoles, and wigglers
- Comparing with other local cloud measurements, such as shielded pickups
- Incorporating a more complete description of photoelectron emission

The end result of this analysis will be a detailed and self-consistent description of the in situ primary and secondary emission properties of the materials under investigation.

Investigations into Modelling the Chicane Cyclotron Resonance Measurements The cyclotron resonance measurements described above corroborated the earlier SLAC measurments made under very different beam conditions [42, 43]. The electron cloud modeling program POSINST successfully modeled the SLAC measurements, showing that the resonant cloud buildup enhancements observed for the uncoated aluminum vacuum chamber can follow from higher energy electrons striking the bottom and top of the vacuum chamber at more grazing angles [43]. We have undertaken similar modeling studies with the ECLOUD program package, extending them to describe the resonant suppression mechanism observed in the TiN-coated chamber which is shown in Fig. 1.28. Figure 1.39 shows the ECLOUD result around the first cyclotron resonance (n=1, B=89 G) in 2 G steps for the case of an uncoated aluminum chamber. This simple model defines each collector signal by the impact position of electrons on the top of the vacuum chamber. The collector current is derived by the collector area, a transparency factor of 15%, and the size of the time interval. No kinematic RFA acceptance function is applied, nor is any interaction between the RFA and the cloud taken into account. Collector signal sums are accumulated over a time span of 360 ns, the first half of which comprises 45 4-ns-spaced bunches populated with 1.44E10 2 GeV positrons. A secondary yield value of 2.0 is assumed, as is an elastic yield of 1.0. No rediffused component in the secondary yield is included in the model. The sum of the 17 collector signals clearly show the resonant behavior. The individual collector contributions show that the central collectors (collector 7-11) signal varies little with magnetic field, while the resonant effect is clear in the outer collectors. Figures 1.40 and 1.41 show how the increased signal on resonance arises. The upper plots show the secondary yield as a function of incident electron energy, while the lower plots show the distribution of incident energies. On resonance there is a class of electron with increased energies, resulting in higher yields since for this bunch population the cloud energies are generally below the peak energy of the secondary yield curve (300 eV). In addition, the spread in true secondary yields near the peak energy is larger. This spread shows the range of incident angles, since the peak yield value of 2.0 is increased by a factor of up to 1.5 at more grazing incidence. The resonance is enhanced by the circular shape of the vacuum chamber in the chicane, since the beam kicks from the centered beam are radial. A model with an elliptical vacuum chamber showed no resonant behavior since the incident angles were more grazing both on and off resonance.

This simple explanation for the resonant RFA signals is apparently contradicted by the resonance suppression exhibited in a TiN-coated chamber (see Fig. 1.28) under the same beam conditions. Since the cloud electron energy distribution and incident angles must be very similar, we investi-

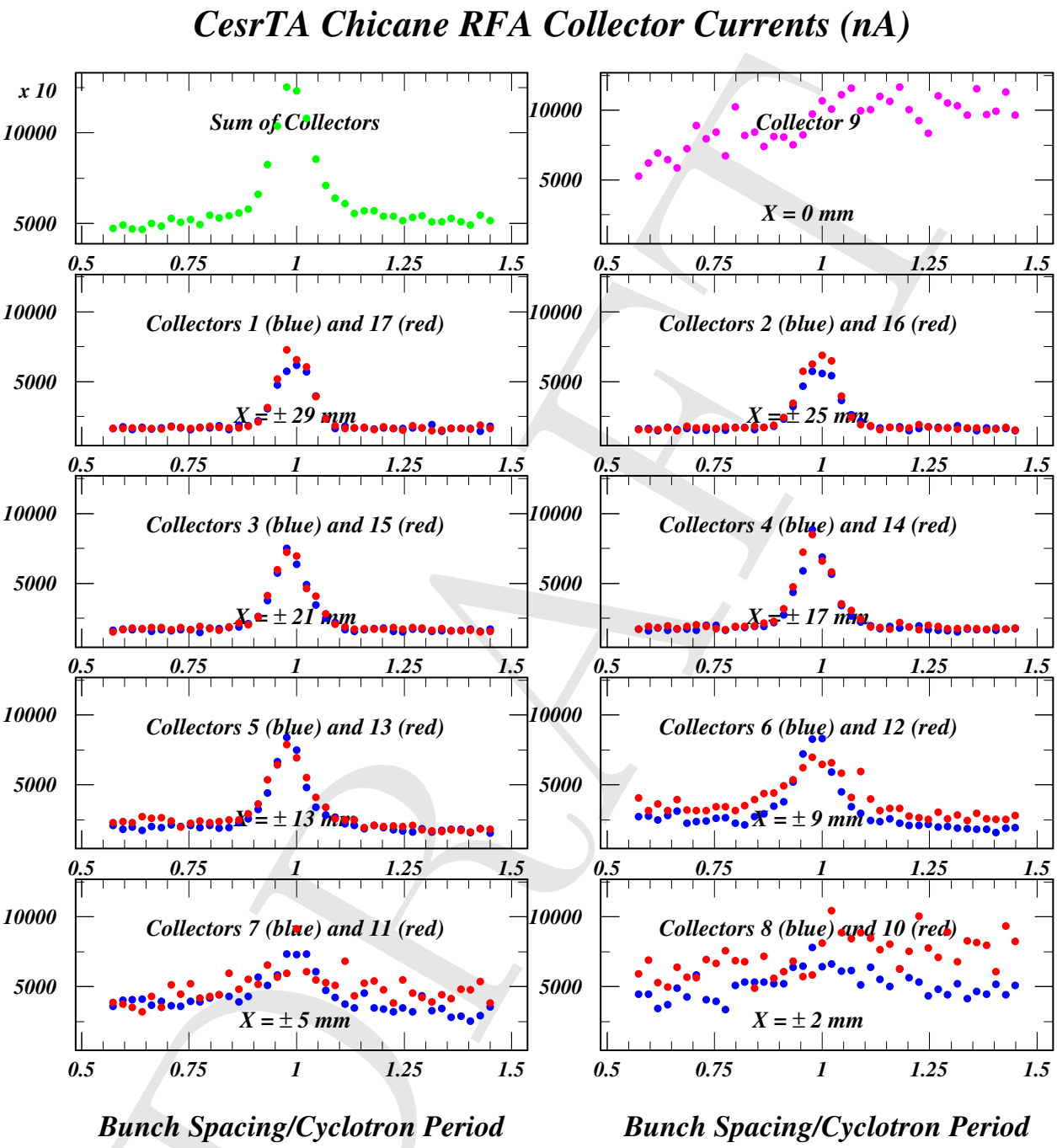

Figure 1.39: ECLOUD model for the RFA signals measured with the SLAC RFA in the PEP-II chicane for a 45-bunch train of 2 GeV positrons. The sum of the 17 collector signals is shown in green in the upper left plot as a function of the ratio of bunch spacing to dipole magnetic field as the field is varied in 2 G steps around the resonant value of 89 G. The central collector signal is shown in the upper right plot. The signals from the remaining 16 collectors are shown in left-right symmetric pairs. This result showing the resonant enhancement of the RFA signal was obtained with a secondary yield model appropriate for an uncoated aluminum chamber.

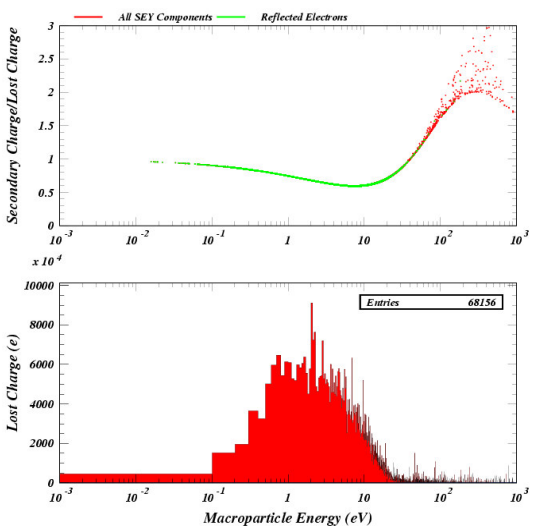

Figure 1.40: Population of the modeled secondary yield curve for the case of an uncoated aluminum chamber and a chicane magnetic field value of 129 G, halfway between the first and second cyclotron resonances for the 4-ns bunch spacing.

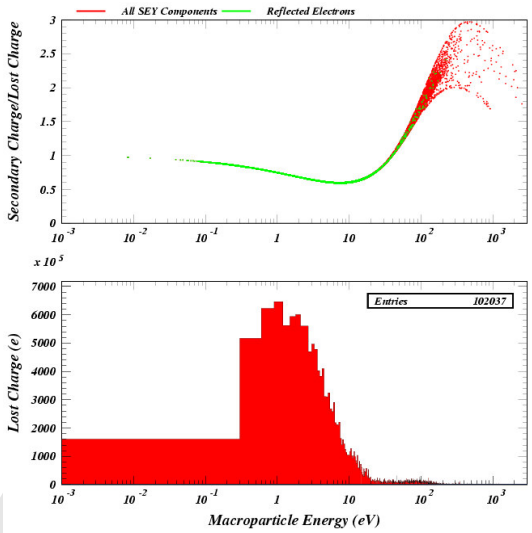

Figure 1.41: Population of the modeled secondary yield curve for the case of an uncoated aluminum chamber and a chicane magnetic field value of 89 G, which corresponds to the first cyclotron resonance for the 4-ns bunch spacing.

gated the possibility of a secondary yield curve decreasing with energy below the peak yield. We chose a value of 1.0 for the elastic yield at low incident energy and a value of 0.5 for the peak true secondary yield. The result, shown in 1.42, demonstrates that the resonant suppresion effect can be modeled in this manner. Figures 1.43 and 1.44 show the corresponding secondary yield population curves. Further modeling studies showed the transition from resonant suppression to enhancement observed in the PEP-II data [42] in the same field scan over multiple resonances can also be reproduced. However, there is no independent empirical evidence for such behavior in the secondary yield for a TiN-coated chamber. The *in situ* measurements of TiN-Al samples described below have measured true secondary yield values near 1.0, not 0.5. And the shielded pickup measurements of cloud lifetime described in Sect. 1.2.2 clearly exclude values for the elastic yield great than 0.1. Further modeling studies will be needed to understand the physical basis for the resonant suppression.

1.1.4.3 Conclusions

1.1.5 Vacuum Performance Issues

1.1.6 In-situ SEY Studies

We used the in-situ SEY station described in Section **??** to take measurements on samples roughly once a week. Measurements were done on samples coated with SEY-reducing films and bare metal samples.

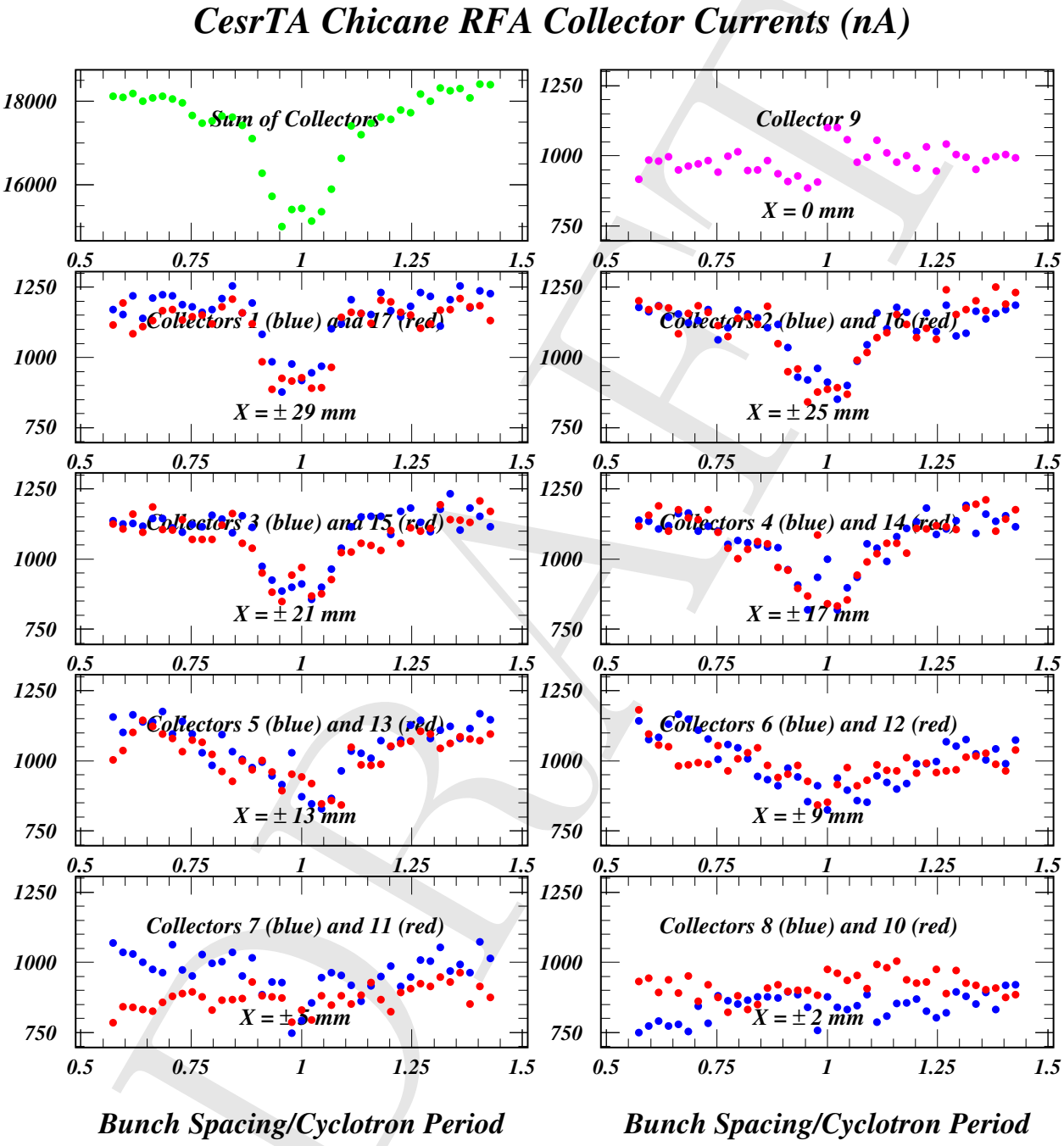

Figure 1.42: ECLOUD model for the resonant suppression observed in the TiN-coated chamber in the PEP-II chicane. This result was obtained under the assumptions of a peak secondary yield of 0.5 and an elastic yield value of 1.0.

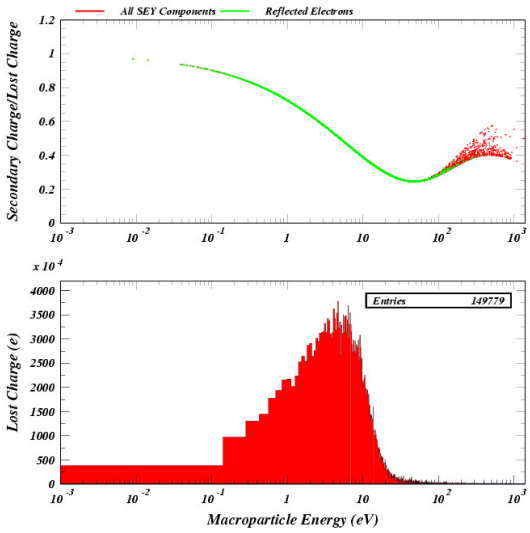

Figure 1.43: Population of the modeled secondary yield curve for the case of a TiN-coated aluminum chamber and a chicane magnetic field value of 129 G, halfway between the first and second cyclotron resonances for the 4-ns bunch spacing.

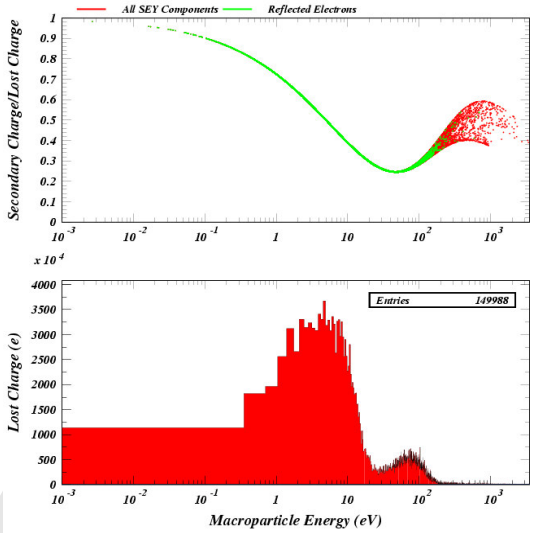

Figure 1.44: Population of the modeled secondary yield curve for the case of an TiN-coated aluminum chamber and a chicane magnetic field value of 89 G, which corresponds to the first cyclotron resonance for the 4-ns bunch spacing.

1.1.6.1 Secondary Electron Yield

The SEY is defined as

$$SEY = I_{SEY}/I_p \,, \tag{1.6}$$

where I_p is the current of the primary electrons incident on the sample and I_{SEY} is the current of the secondary electrons expelled by the bombardment of primary electrons. The SEY depends on the energy and angle of incidence of the primary electron beam. The primary current I_p is measured by firing electrons at the sample with the electron gun and measuring the current from the sample with a positive bias voltage. A high positive biasing voltage of ∼150 V is used to recapture secondaries produced by the primary beam, so that the net current due to secondaries is zero.

The current I_{SEY} due to secondary electrons is measured indirectly. The total current I_t is measured by again firing electrons at the sample, but with a low negative bias (~ -20 V) on the sample to repel secondaries produced by the primary electron beam, and also to repel secondaries from "adjacent parts of the system that are excited by the elastically reflected primary beam" [28]. Since I_t is effectively the sum of I_p and I_{SEY} ($I_t = I_p + I_{SEY}$, with I_{SEY} and I_p having opposite signs), we calculate SEY as

$$SEY = (I_t - I_p)/I_p \,. \tag{1.7}$$

Some SEY systems include a third electrode for a more direct measurement of I_{SEY}, for example the system at KEK [44]. Our in-situ setup cannot accommodate the extra electrode, so we cannot use the more direct method; we must use the indirect method described above.

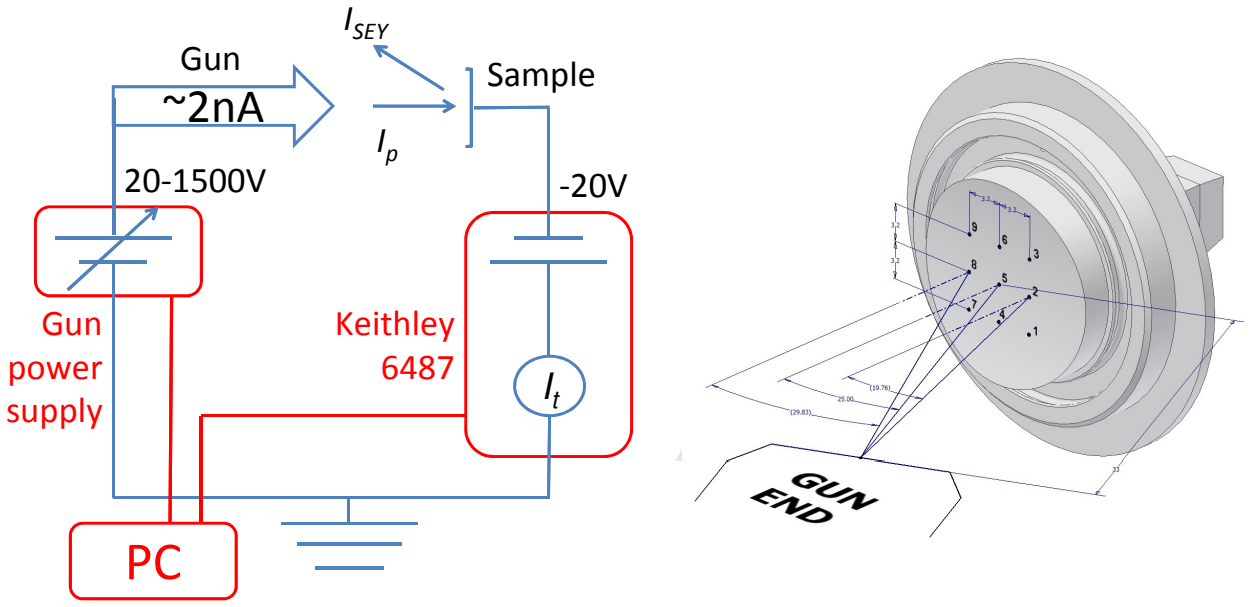

Figure 1.45: Left: Data acquisition schematic. Right: 9 grid points where the SEY is measured.

1.1.6.2 Data Acquisition System

An electrical schematic of the system is shown in Figure 1.45. The current on the sample is measured during three separate electron beam energy scans. Each scan automatically steps the electron gun energy from 20 eV to 1500 eV in increments of 10 eV. For each energy, the focusing voltage is set to minimize the beam spot size on the sample, based on previous measurements. This process is controlled by a LabVIEW interface we developed [45] incorporating existing software from Kimball Physics and Keithley. The first scan is done with a 150 V biasing voltage on the sample to measure I_p, with gun settings for $I_p \approx 2$ nA. This measurement is taken between grid points 5 and 9 to avoid processing the measurement points with the electron beam during the I_p measurement.

The second scan steps through the same gun energies with a bias voltage of -20 V on the sample to measure I_t. At each gun energy, the beam is rastered across all 9 grid points while the program records the current for each point.

To minimize error due to drift in the gun output current, we take a second I_p scan after the I_t scan. The two I_p sets are averaged and the SEY is calculated at each energy. Identical measurements are performed on the 45° system and the horizontal system.

1.1.6.3 Results

In-situ measurements have been done on bare aluminum, titanium nitride, and amorphous carbon surfaces. Additional SEY measurements have been done on diamond-like carbon (DLC) surfaces, but no measurements on DLC samples have been done in-situ yet.

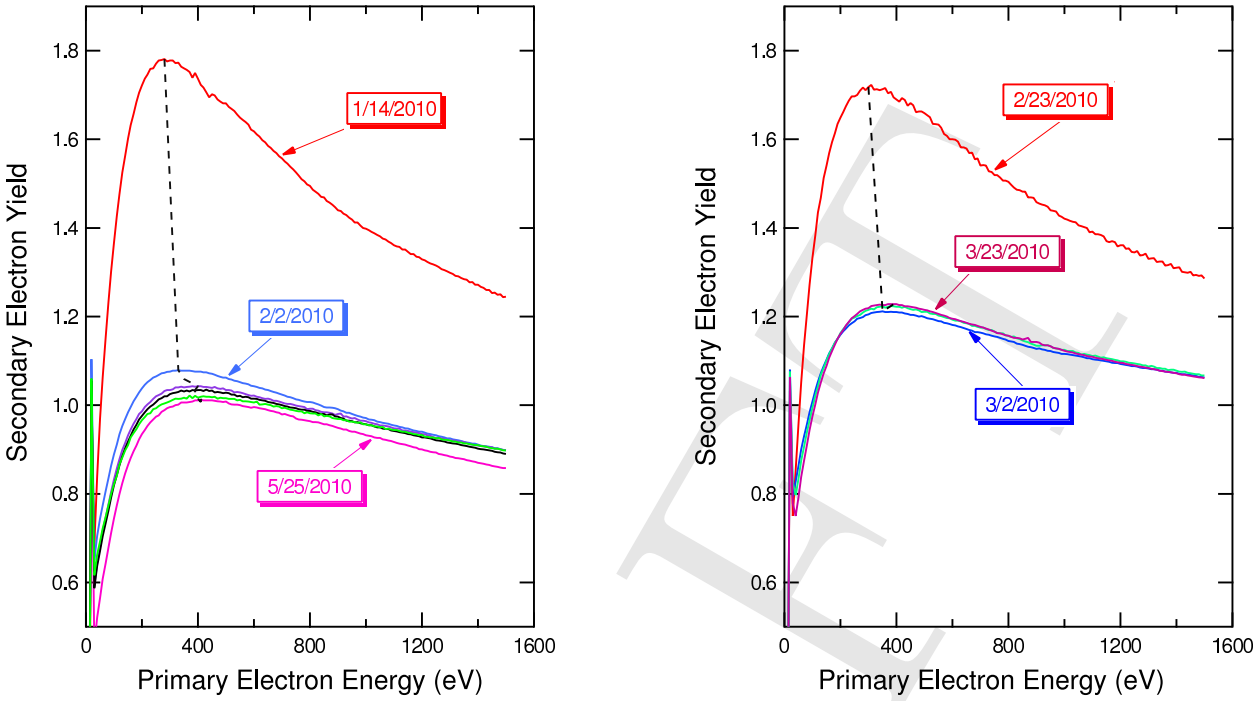

Figure 1.46: Repeated measurements of SEY as a function of energy for TiN-Al samples in the horizontal station (left) and the 45° station (right).

Aluminum Samples with TiN Coatings Aluminum samples with titanium nitride coatings provided by M. Pivi (SLAC National Accelerator Laboratory) were installed in CESR in both the horizontal and 45° stations from January to August 2010 and their SEYs were measured roughly once a week. These results are summarized in Figure 1.46. There is a peak in the SEY for an incident electron energy near 400 eV. A significant decrease in the SEY is evident between the first round of measurements and subsequent measurements. As the SEY decreases, there is a slight upward shift in the energy at which the peak in the SEY occurs, as indicated by the dotted lines in Figure 1.46.

The value of the SEY peak and the energy E_{max} at which the peak occurs are useful metrics for tracking the SEY behavior as a function of exposure. The beam conditioning behavior of the samples is illustrated in Figure 1.47, which shows the peak SEY and E_{max} for the center grid point as a function of accumulated dose. The bottom axis indicates the electron beam current integral in ampere·hours; the top axis indicates the calculated SR dose to the vacuum chamber wall in photons per meter. Neither of these values includes a contribution from the positron beam, because the dominant source of SR for the SEY stations is the electron beam. The SR photon dose in Figure 1.47 accounts for direct SR from the beam onto the chamber wall at the location of the SEY stations: it represents the "source term" and does not attempt to include the effects of scattering of photons (or production of photo-electrons). The dose calculation does not differentiate between the horizontal and 45° stations, even though the 45° station does not receive direct SR and the stations' distance from the bending magnet is not exactly the same.

As can be seen in Figure 1.47, the "fresh" sample in the horizontal setup began with a peak SEY of almost 1.8 and reached a minimum SEY peak of just under 1. At this point the sample remained under ultra-high vacuum (high 10^{-9} torr) for 2 weeks without exposure to beam. Under these

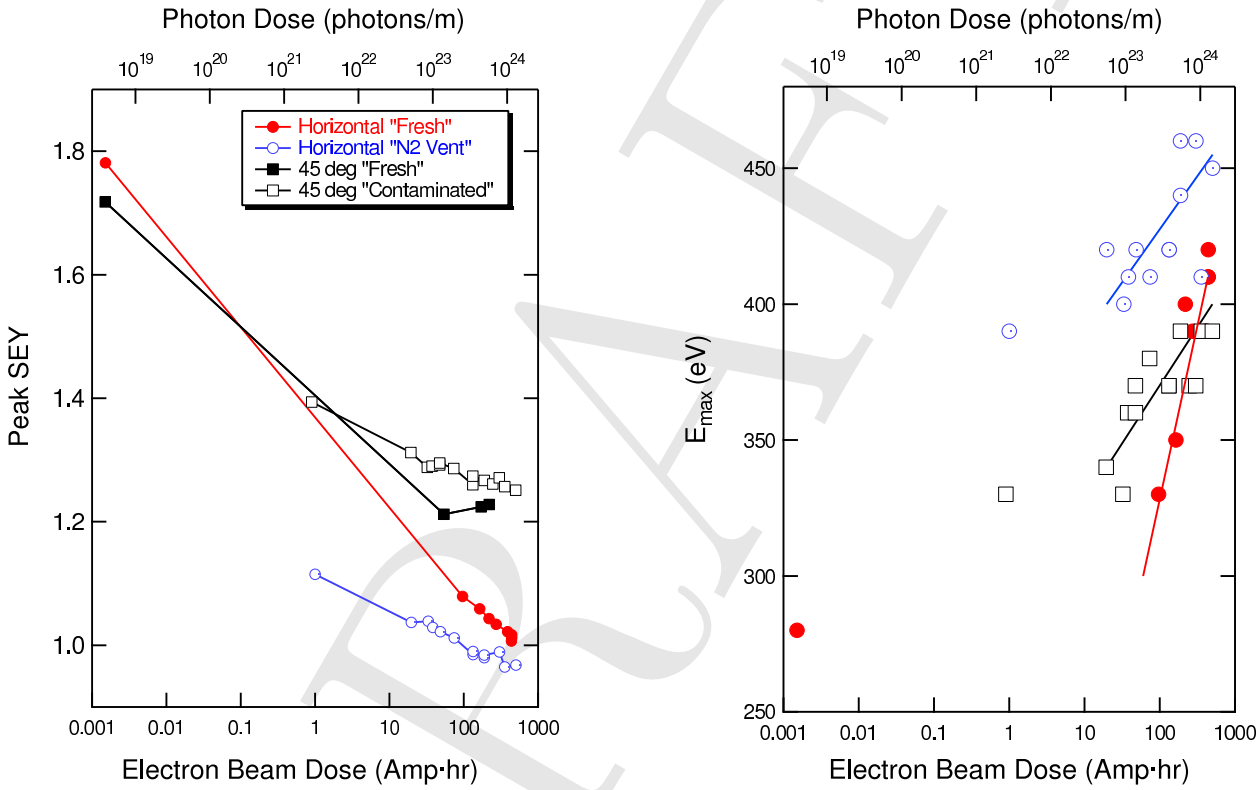

Figure 1.47: Dependence of SEY peak (left) and E_{max} (right) on dose for TiN-Al samples in the horizontal and 45° stations.

conditions, the SEY increased by about 1%. After that, the sample was exposed to nitrogen gas for 1 hour and then the system was pumped down again. The measured peak SEY increased from 1 to 1.12 after exposure to nitrogen. The sample was once again processed in CESR for about 10 weeks, with weekly SEY measurements; the peak SEY decreased to about 1.

The "fresh" sample in the 45° station started with a peak SEY of just above 1.7 and reached a minimum SEY peak of around 1.2. After that the sample in the 45° was left under ultra-high vacuum in the SEY system for 2 weeks, the peak SEY increased from 1.2 to 1.4. At that point we have realized that the miniature hot filament vacuum gauge of the system had been left on, and that this could explain why the peak SEY of the fresh sample after it reached a peak SEY of about 1.2 was increasing by few percent every week instead of decreasing as the horizontal sample had been by a 1 to 2 percent per week. At that point, we have turned the miniature hot filament gauge off and processed the sample in CESR for about 10 weeks. The peak SEY decreased to about 1.2, as can be seen in the 45° "contaminated" curve in Figure 1.47. In a separate check, we have found that the emission from a hot-filament vacuum gauge can contaminate the sample and causes the SEY to increase.

Aluminum Alloy Samples In August 2010, aluminum alloy samples (Al6061-T6) were installed in the in-situ systems. The results are summarized in Figure 1.48. The sample in the horizontal setup began with a peak SEY of 2.5 for the center grid point, and reached a minimum SEY peak of around 1.6 after 3 ampere·hours of exposure. The sample in the 45° station began with a peak SEY of 2.25 in the center and reached a peak SEY of 1.6 after the same exposure. At this point the horizontal SEY system was removed because of a malfunction and the spare SEY system with a new Al6061-T6 sample was installed in the horizontal position. This new Al6061 sample had an initial SEY of about 2.9 and, after processing in CESR for about 6 weeks, the peak SEY decreased to 1.9. The peak SEY of the 45° sample decreased from 1.6 to 1.5 during these 6 weeks of processing in CESR. The peak SEY value of 1.5 was achieved after 20 ampere·hours of exposure. There was very little change in the SEY (a slight increase was observed) with additional exposure up to 120 ampere·hours. Similarly, the second sample in the horizontal system had a nearly constant peak SEY (with a slight increase) after 50 ampere·hours of exposure, up to about 100 ampere·hours.

The difference in the initial SEY between aluminum samples is presumably due to differences in the initial surface condition. The Al6061-T6 samples were installed "as received" after cleaning in an ultrasonic bath with alcohol to remove oil residues from machining. The initial peak SEY of bare aluminum samples can vary a lot depending on the surface oxide layer.

Amorphous Carbon-Coated Samples In November 2010, the samples were replaced with amorphous carbon-coated samples provided by S. Calatroni and C. Yin Vallgren (CERN). The substrates were Al6061 (installed in the horizontal station), copper (installed in the 45° station) and stainless steel (not installed in CESR, but measured in an off-line SEY system). The peak SEY of the samples as a function of dose in CESR is shown in Figure 1.49. As can be seen, the peak SEY of both samples is hardly affected by the exposure to the beam.

Initial Measurements on Diamond-Like-Carbon-Coated Samples We have done initial SEY measurements on samples with diamond-like carbon (DLC) coatings on aluminum. The DLC samples were provided by S. Kato (KEK). We have not yet installed any DLC samples in CESR;

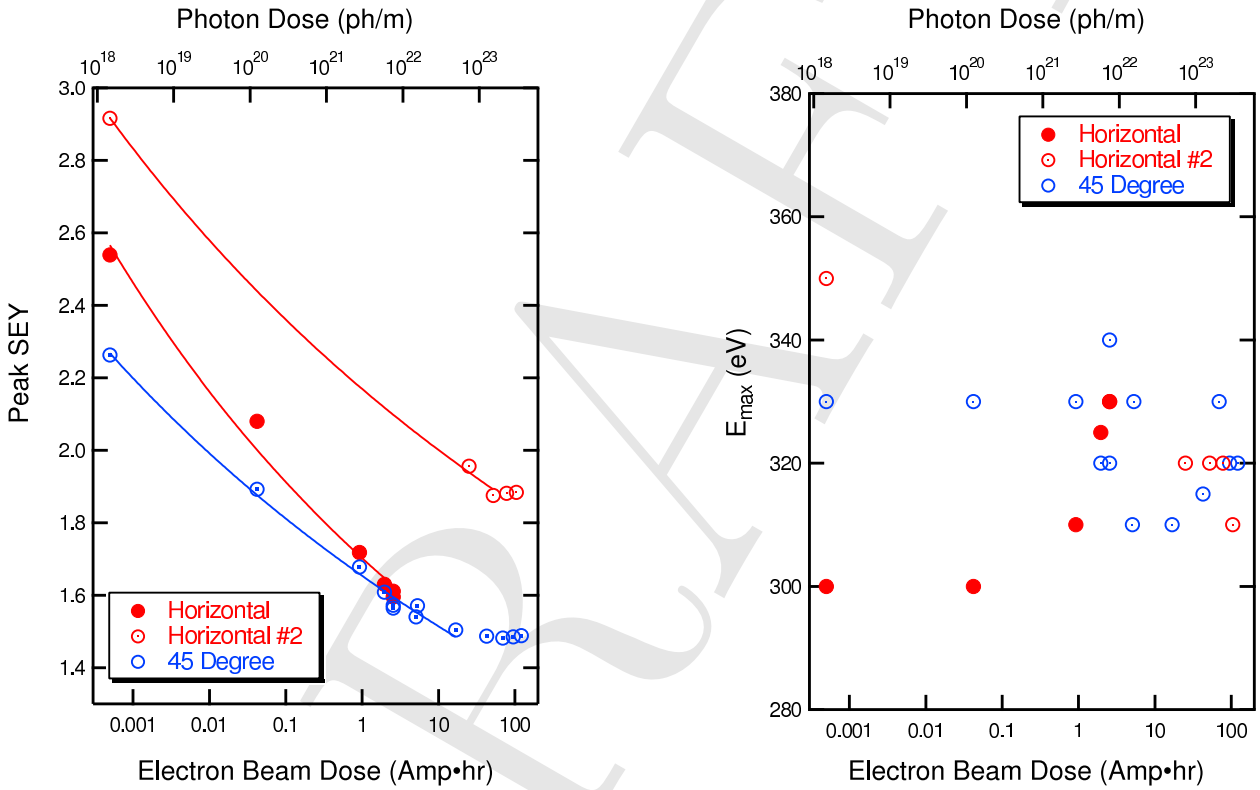

Figure 1.48: Dependence of SEY peak (left) and E_{max} (right) on dose for Al6061-T6 samples in the horizontal and 45° stations.

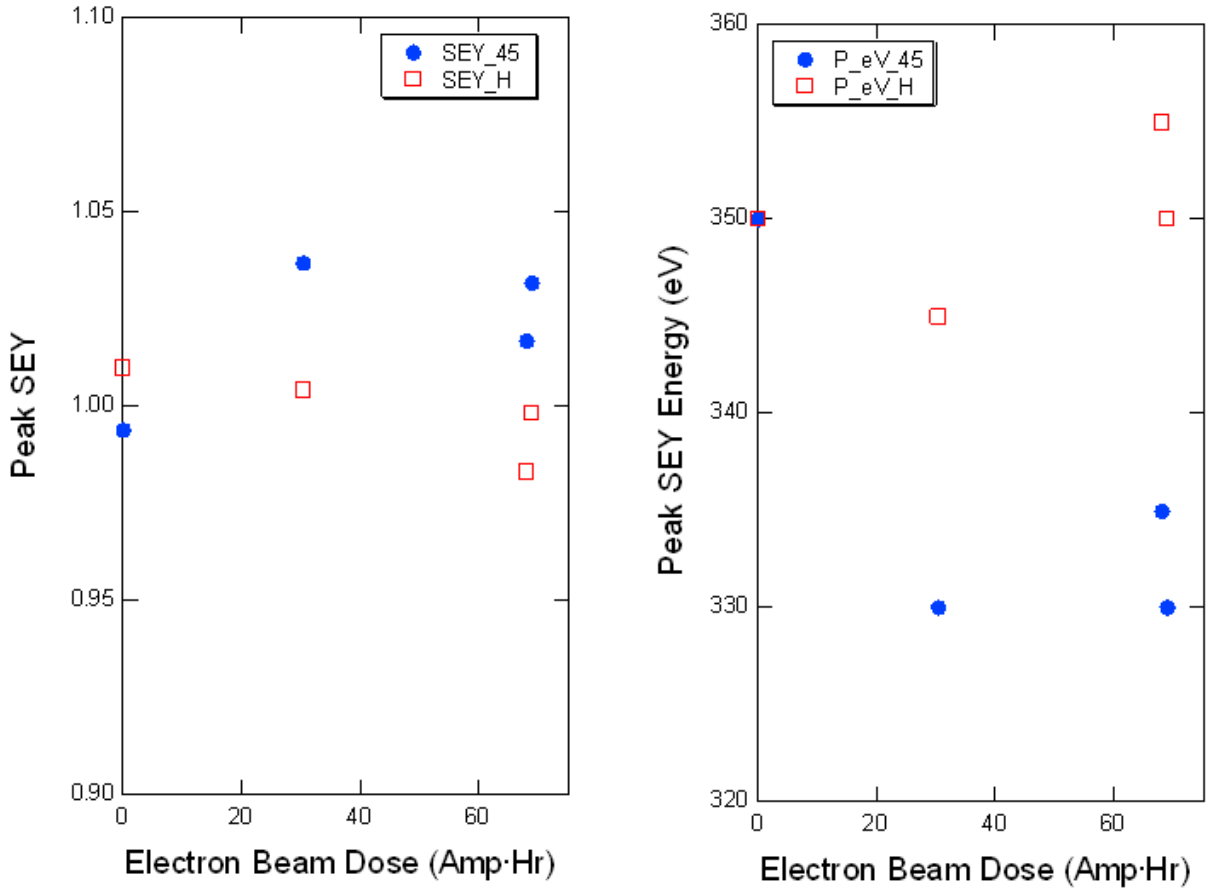

Figure 1.49: Dependence of SEY peak (left) and E_{max} (right) on dose for amorphous carbon-coated samples in the horizontal and 45° stations. **[Need to make this plot consistent with other plots and use vector graphics]**

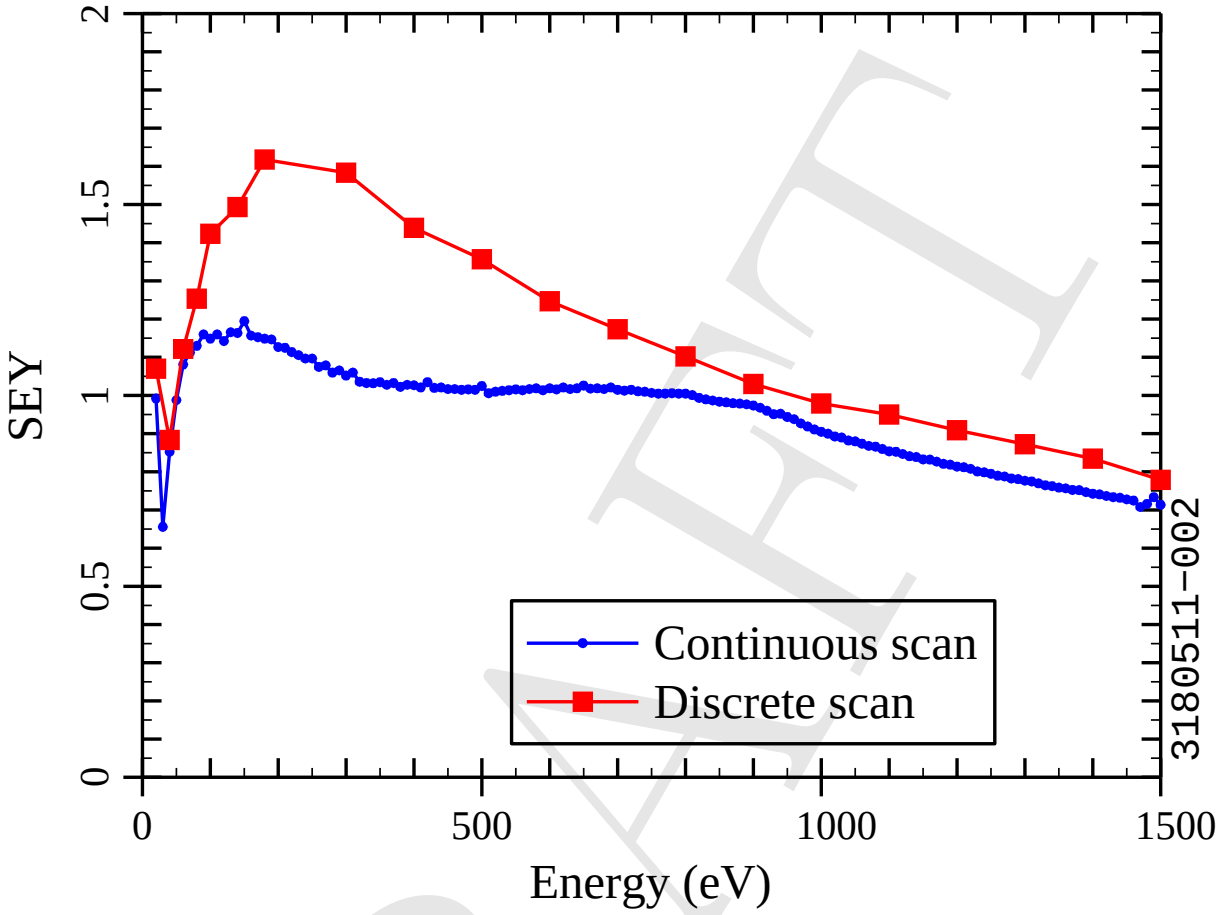

Figure 1.50: SEY as a function of incident electron energy for a diamond-like carbon-coated aluminum sample. The blue circles correspond to a "continuous" scan in energy (5 seconds for each energy, with all 9 grid points; Point 5 is shown). The red squares correspond to a "discrete" scan in energy (3 to 4 minutes waiting period with the electron beam deflected away from the point of interest before each measurement; only Point 9 was measured).

we have only measured the SEY in the off-line system so far. The measured SEY as function of beam energy for one of the DLC samples is shown in Figure 1.50 (blue circles). The SEY is strongly distorted due to charging of the DLC-coated surface by the electron beam. To measure the true SEY, we waited a long time (3 to 4 minutes) between each increment in the electron beam energy to allow the surface to discharge and did the scan with a beam current of about 0.5 nA. The results are shown in Figure 1.50 (red squares). As can be seen, the delay time produces a significant change in the measured SEY.

1.1.6.4 Discussion

Our results shows that the initial 80% to 90% decrease in the peak SEY occurs within the first 2 weeks of processing, with a total photon dose of 10^{22} photons/m. This is true for both the horizontal

and the 45° systems. After the rapid SEY decrease in the first 2 weeks, the peak SEY decreases about 1 to 2% per week with processing for both the TiN-Al samples and the bare Al6061 samples. On average the peak SEY decreases with increasing beam dosage, D, proportional to $D^{-0.030}$ for both the bare aluminum and the TiN-coated aluminum samples.

At this point we do not have enough data to draw any conclusions about the difference in processing between samples placed in the horizontal system and the 45° system. For the TiN-Al, the sample placed in the horizontal system reached a lower SEY value: a peak SEY of 1 compared to 1.2 in the 45° system. For the bare Al6061 samples, one set of samples reached the same peak SEY of 1.6. A third sample in the horizontal system started at a higher initial SEY value of 2.9 and reached a minimum peak SEY of 1.9 after an additional 6 weeks of processing in the horizontal system. For comparison, in studies done at PEP-II, a bare Al6063 sample was processed in PEP-II beam line had an initial peak SEY of 3.5 and reached a peak SEY of 2.4 after processing [46]. These measurements suggest that, for bare aluminum samples, the initial value of the peak SEY varies from sample to sample and the final value of the peak SEY after processing depend on the initial value.

The amorphous carbon-coated samples had initial peak SEY values of about 1. They showed almost no change in the peak SEY either in the horizontal or the 45° system.

We observed small, consistent differences in the peak SEY corresponding to the angle θ between the incident electron gun beam and the normal to the sample surface. We have $\theta = 20°$ for points 1, 2, and 3; $\theta = 25°$ for points 4, 5, and 6; and $\theta = 30°$ for points 7, 8, and 9 (see Figure 1.45). Higher SEYs were observed at points with larger θ. An example is shown in Figure 1.51 for one of the amorphous carbon-coated samples (a stainless steel sample). The measurements for $\theta = 0$ were done at CERN by S. Calatroni and C. Yin Vallgren on a different sample. These measurements indicate that, at $E_{max} = 300$ eV, the SEY dependence on incident angle θ is $\exp[1 - 0.45\cos(\theta)]$.

Our observation that the SEY depends on angle of incidence is qualitatively consistent with the observations that, as the primary electron angle goes from normal incidence toward grazing incidence, the SEY increases; this has been reported in recent secondary emission studies [28] as well as early experiments [47].

1.1.6.5 SEY Studies Summary and Future Plans

For TiN-Al samples and bare Al6061 alloy samples, we observed that the main processing occurred within the first 2 weeks, with a total photon dose of 10^{22} photons/m, while, after that, the SEY decrease was about 1% per week. For Al6061, we observed that the SEYs after processing are lower than the minimum SEY value of 2.4 for Al6063 reported by SLAC [46].

We are able to observe a small dependence of the SEY on the angle of the incident electron beam. This indicates that the statistical errors are small enough for us to be able to resolve differences of a few percent.

We are working on mitigating the effects of the current drift of the electron gun. The drift causes a systematic error of around 2 to 4% in the calculated SEY. One method we are investigating is to measure I_p for a given gun energy, and then change the bias voltage to measure I_t at the same energy, before stepping to the next energy and repeating the process. However, we must account for the discharging time of the capacitance of the SEY system and cables when we switch the biasing voltage from 150 V to −20 V (and vise-versa), which can dramatically distort our current

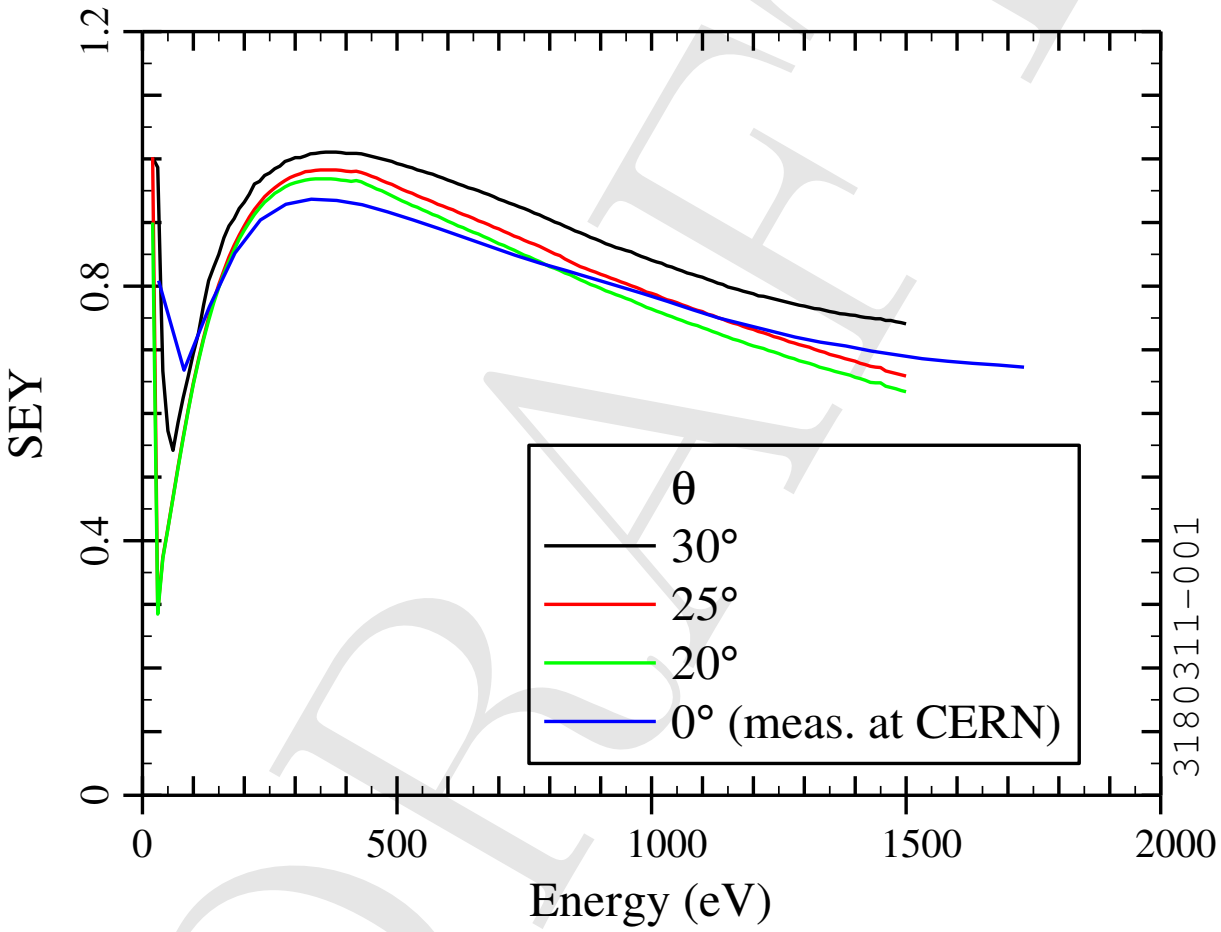

Figure 1.51: Angular dependence of SEY as a function of incident electron energy for amorphous carbon-coated stainless steel sample.

readings. The discharging of the system can be on the order of minutes. In our present method, the biasing voltage is only switched twice, adding just a few minutes to the measurement time. However, the method we are investigating switches the bias voltage at every energy—with 150 gun energy changes per scan, the measurement time may be prohibitively long. We are investigating modifications to minimize the stray capacitance and take fewer energy points.

We plan to compare the Al6063 and Al6061 alloys to better understand the large difference in the peak SEY achieved after processing. Other future work will include the study of other material samples, including samples cut from an extruded, aged (30+ years) 6063 aluminum CESR chamber. In addition, we plan to measure the SEYs of materials coated in non-evaporable getter (NEG) thin film, and continue to study amorphous/diamond-like carbon samples.

We plan to check the reproducibility of the results on TiN-Al samples and do additional checks for systematic effects. We are designing additional experiments to determine whether SR bombardment or electron cloud bombardment is the main source of processing.

1.2 Other Methods to Characterize EC Build-Up

While the RFAs provide the largest number of detectors at CesrTA, other techniques for measuring the electron cloud density are being used at a subset of locations. TE Wave and Shielded Pickup detectors provide data that is complimentary to that of RFAs. The Shielded Pickups have a geometry that is similar to that of an RFA, but are designed to measure time resolved signals, while the RFAs measure integrated current. The TE Wave technique - where the periodic electron cloud modulates a carrier transmitted through the beampipe - is sensitive to the cloud density in the center of the pipe, while both the RFA and Shielded Pickups measure the cloud current that is normal to the pipe surface. The comparison of data taken using these complimentary techniques should result in consistent measurements and modeling.

1.2.1 TE Wave Studies

Two versions of TE wave measurements were made at CesrTA. Initial measurements were based on the transmission of microwaves between two points in the accelerator, using the beampipe as a waveguide. In the course of taking this data, it became clear that a different interpretation of the signals was needed in most cases - due to the presence of resonances in the frequency response of the beampipe. This resulted in the recent development of TE wave resonant measurements where the beampipe and its reflections are treated as a resonant cavity. Both techniques will be discussed in the sections below. The transmission technique would be most relevant for regions of an accelerator where there are few reflections; the resonant technique for regions where the reflections are significant. These sections also show the historical development of TE wave studies.

1.2.1.1 TE Wave Transmission Measurements

Improvements to the theoretical model The theoretical model of the TE wave measurement proposed by Caspers et al. in [48] only took into account the phase delay induced by the electron cloud on a propagating TE wave. Moreover, changes in the cloud density were supposed to have a

simple sinusoidal evolution. Under such a hypotheses the modulation sidebands amplitude, relative to the carrier SB_c, is simply given by

$$SB_c = \frac{\Delta\Phi}{2} \tag{1.8}$$

if $\Delta\Phi$ is the modulation index, with only one upper and one lower sideband present for low index modulation, which is always the case with cloud densities normally encountered in particle accelerators. In the course of our experimental work, we encountered situations were amplitude modulation, and more in general simultaneous phase and amplitude modulations, were present. Additionally, the purely sinusoidal modulation model turned out to be an excessive abstraction in most cases, so that an effort to generalize the theory proved to be necessary. We summarize the result of our effort in the following subsections.

AM/PM modulation To increase the measurement sensitivity, it is good practice to choose the TE wave frequency in correspondence of a peak maximum in the beampipe transmission function. In most cases those peaks correspond to standing waves trapped by discontinuities in the vacuum chamber [49], may contain a simultaneous amplitude modulation component. The general formulation for an AM/PM modulation is reported in Ref. [50]. If the standing wave has a narrow resonance (high quality factor Q_0), the modulation indexes are given by

$$\begin{aligned} \Delta M &= \frac{Q_0^2}{2}\left(\frac{\omega_p}{\omega_{res}}\right)^4 \\ \Delta\Phi &= Q_0\left(\frac{\omega_p}{\omega_{res}}\right)^2 \end{aligned} \tag{1.9}$$

where $\Delta M = \Delta\Phi^2/2$ is the amplitude modulation index and ω_{res} is the center frequency of the resonance. In the hypothesis $\omega_p << \omega_{res}$ the modulation sidebands amplitude can be written as

$$SB_c \approx \Delta\Phi\left[1 + \frac{1}{2}\left(\frac{\Delta\Phi}{2}\right)^2\right]|F(\omega)| \tag{1.10}$$

where $|F(\omega)|$ is the Fourier transform of the cloud normalized density. In the case of a sinusoidal modulation we can compare Eqs. 1.8 and 1.10 and see that the corrective term in brackets accounts for the AM/PM modulation.

Time evolution of the electron cloud density From Eq. 1.10 one can easily see that the temporal evolution of the electron cloud density is described by the function $F(\omega)$ in the frequency domain, which being the transform of a periodic function will be composed of discrete lines separated by the ring revolution frequency ω_{rev}. In practical cases one usually observes a number of sidebands, even for small modulation depths, as shown in Fig. 1.52. A fairly good approximation can be obtained assuming that rise and fall times of the EC density are much shorter than the bunch train length, but still at least comparable with the bunch spacing. In such a case, a rectangular modulating function with duty factor equal to the train length divided by the machine length, can obviously be seen as a more accurate representation than a sinusoidal one.

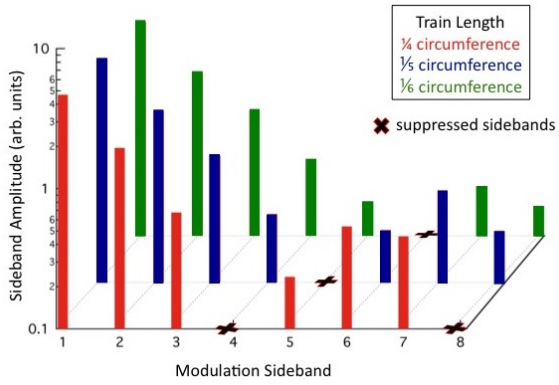

Figure 1.52: Cancellation of modulation sidebands due to different bunch train lengths. Suppressed modulation sidebands due to the rectangular modulation function are indicated for various train lengths.

This hypothesis can find a degree of experimental verification by looking at the sidebands with different train lengths. Figure 1.52 shows a detail of measurements in a dipole region of CesrTA with bunch trains of different lengths equal to one fourth, one fifth and one sixth of the ring circumference. One can see that correspondingly every fourth, fifth and sixth beam harmonic is suppressed. The general properties of the Fourier transform point out how this behavior is evidence of a strong rectangular modulation component. In such a case we can modify Eq. (1.8), by introducing a correction factor that takes into account the rectangular nature of the modulation and we have

$$\Delta\varphi = \frac{1}{2} \cdot \mathrm{SB}_c \frac{\pi}{\sin(t_b \omega_{rev}/2)} \tag{1.11}$$

where t_b is the bunch train length. Applying *Carson's Bandwidth Rule* [51] an approximate evaluation of the EC density rise and fall times (t_r) is given by

$$t_r \approx \frac{2}{3} \frac{2\pi}{\omega_{rev} \cdot N_{SB}} \tag{1.12}$$

where N_{SB} is the number of visible sidebands.

Beampipe attenuation compensation Experimental data showed a substantial difference in signal attenuation for different frequencies even on a relatively narrow frequency span such as the 390 kHz between TE wave frequency and first modulation sidebands. These differences need to be compensated in order to correctly evaluate the modulation depth. It is worth stressing that we frequently measured differences of several dB, which would easily cause significant errors if unaccounted for. Furthermore, the attenuation can change substantially with varying beam conditions, due principally to thermal effects, so that a continuous monitoring is necessary.

The relative amplitude of upper and lower sidebands (USB and LSB, respectively) have to be corrected for the difference in transmission function of the measuring system at the carrier and USB and LSB frequencies. This can be done with separate measurements, but we have recently

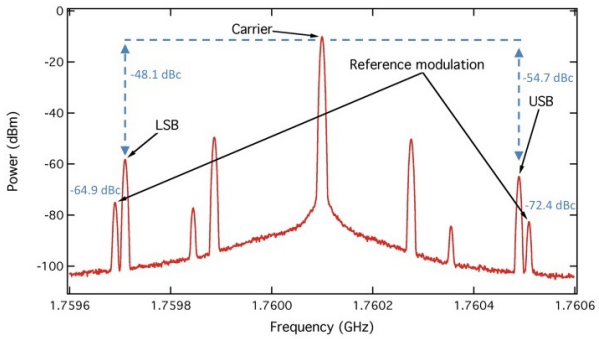

Figure 1.53: Example of sidebands measurement in the wiggler straight. 45-bunch positron train of 60 mA total beam current with 14 ns bunch spacing, with reference modulation sidebands (1 mrad modulation depth at 410 kHz).

introduced a calibration phase modulation of known index at a frequency close to the e-cloud modulation frequency, so that the transmission function is about equal to that for the nearby modulation sidebands. In this case, the reference phase modulation index at 410 kHz was chosen to be 1 mrad, which should generate sidebands at -66 dBc. We observe lower values from which it is possible to infer the attenuation, with respect to the carrier frequency, at the USB and LSB frequencies (390 kHz). We calculate a correction factor equal to $-66.0 - (-64.9) = -1.1\ dB$ for the LSB and, analogously, +6.4 dB for the USB. The corrected value for the LSB is -49.2 dBc and -48.3 dBc for the USB. It is worth noticing that, while before correction the two sidebands were rather different (6.6 dB), after the correction is applied their values are almost identical, as expected. An example of sideband measurement in the wiggler straight (L0) is shown in Fig.1.53, where we are measuring the sidebands generated by a 45-bunch positron train of 60 mA total current in a TE wave traveling along the Eastern half of the L0 wiggler straight.

As previously stated, being able to continuously monitor the transmission function at the frequencies of interest is quite important during some experiments when beam and/or machine conditions undergo large variations. In such cases the transmission changes due mostly to thermal effects can disrupt the measurement as shown in Fig.1.54: While ramping the wigglers magnetic field, the emitted synchrotron radiation increase can change the beampipe transmission function at the sidebands frequency so that USB and LSB amplitudes actually appear to diverge during the experiment until the correction is applied.

To estimate the EC density from the sidebands measured in Fig.1.53, we can use the average of the two sidebands -48.8 dBc.

1.2.1.2 TE Wave Resonance Measurements

TE wave resonance measurements treat the beampipe and its reflections as a resonant cavity. Data is generally taken by exciting and receiving at the same detector - so that the value of L used in the transmission technique would be zero, making that interpretation invalid.

As originally proposed, the TE wave technique was based on transmission and reception of microwaves from one point in the accelerator to another using the beampipe as a waveguide. Button detectors, normally used as part of the beam position monitor (BPM) system are used to couple

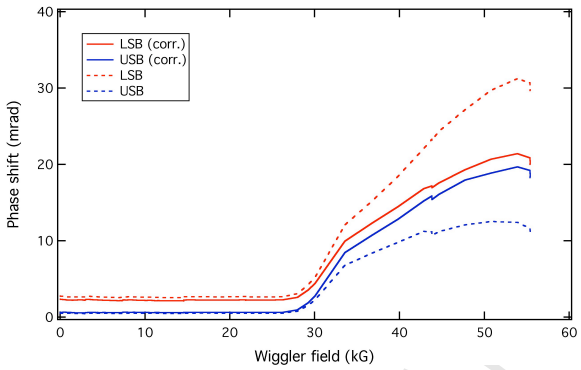

Figure 1.54: Sideband levels relative to the carrier during wiggler ramp in the L0 straight with (solid lines) and without (dashed) correction applied.

microwaves in/out of the beampipe. In the presence of a plasma (the electron cloud), transmitted microwaves will be phase shifted and the EC density measured [50, 52–54].

However, in applying this technique to the data at CesrTA it was noticed that transmission through the beampipe does not have a flat frequency response. In fact, the large variations in response suggest the presence of resonant excitation of the beampipe rather than single pass transmission. This interpretation was confirmed by the response when exciting and receiving at the same location, where very large resonances are often seen.

Reflections and Standing Waves The beampipe at CesrTA was not designed to be a waveguide. In devices such as vacuum pumps, longitudinal slots were used to provide a reasonable vacuum connection, while minimizing the effect of beam-induced fields. However, these longitudinal slots present an obstacle to the propagation of a TE waves. A simple example was found at 43E in CesrTA where a BPM coupler/detector is located between two ion pumps (with slots). The response shown in Fig. 1.55 is consistent with a waveguide of length L having a cutoff frequency f_c and n half wavelengths in the distance L between the pumps [49, 55].

The effect of dielectrics and plasmas on the resonant frequency of a cavity is well established [56]. The effect of small dielectrics on resonant frequency is very useful in mapping the fields of accelerating cavities and plasma densities are routinely measured using resonant cavities [56, 57]. Perturbation techniques provide the following approximation for the shift in resonant frequency due to a dielectric in a resonant cavity [58].

$$\frac{\Delta\omega}{\omega} = \frac{\int_V (1-\varepsilon_r)\, E_0^2\, dV}{2\int_V E_0^2\, dV} \tag{1.13}$$

The effective dielectric constant of a plasma has real and imaginary parts. The imaginary part gives a change in the Q of the resonance, the real part a change in its frequency. For low density plasmas ($\omega_p^2 \ll \omega^2$) with a small collision frequency ($\nu \ll \omega$) and no magnetic field, the real part of the dielectric constant of a plasma can be written as [57]

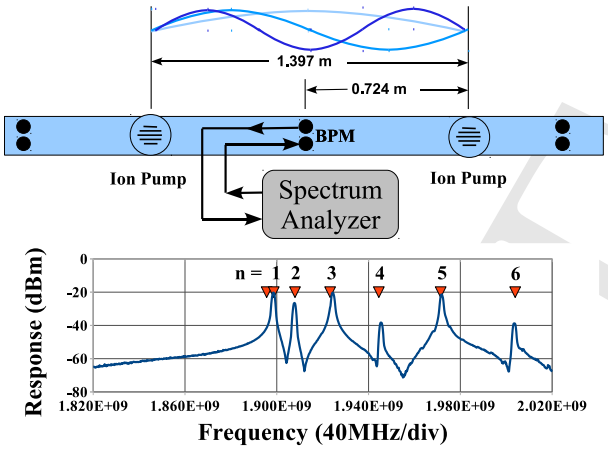

Figure 1.55: Sketch of 43E at CesrTA where a BPM Detector is located between two ion pumps with longitudinal slots. The measured resonances follow the expected $f^2 = f_c^2 + \left(\frac{nc}{2L}\right)^2$ of a rectangular cavity.

$$\varepsilon_r = \left[1 - \frac{\omega_p^2}{\omega^2\left(1 + (\upsilon/\omega)^2\right)}\right]. \tag{1.14}$$

The plasma frequency ω_p is related to the electron cloud density by $n_e = \omega_p^2 \varepsilon_0 m/e^2$ [56]. Let the collision frequency be vanishingly small $\nu \to 0$. The change in resonant frequency becomes

$$\frac{\Delta\omega}{\omega} = \frac{e^2}{2\varepsilon_0 m_e \omega^2} \frac{\int_V n_e E_0^2 \, dV}{\int_V E_0^2 \, dV}. \tag{1.15}$$

The resonant frequency shift is proportional to the local electron cloud density weighted by E_0^2. If there are high local densities where the cavity electric field is zero, they will not have an effect on $\Delta\omega$. If the density is uniform, $\Delta\omega$ is independent of the details of the electric field, since the same integral appears in the numerator and denominator [51]. An EC density of $10^{12}(m^{-3})$ would give a frequency shift of about 20 kHz.

With a train of bunches in the storage ring, the electron cloud will grow and decay each time the bunch train passes a given point - at the revolution frequency f_{rev} (390kHz at CesrTA). The quantity $\Delta\omega$ is the modulation in the resonant frequency of the waveguide cavity produced by the electron cloud. We now need to determine the effect that this modulation has on the observed signals.

Effect on Signals For most of the TE Wave measurements made at CesrTA the resonant beampipe is driven at a fixed frequency and its response measured with a spectrum analyzer. The steady state solution for a driven oscillator is given in the following equations and illustrated in Fig. 1.56.

$$x(t) = A_n sin(\omega t + \phi_n) \tag{1.16}$$

$$A_n = Q\frac{A}{[(\omega_n^2 - \omega^2)^2 + \omega^4]^{1/2}} \tag{1.17}$$

$$\phi_n = tan^{-1}Q\frac{(\omega_n^2 - \omega^2)}{\omega^2} \tag{1.18}$$

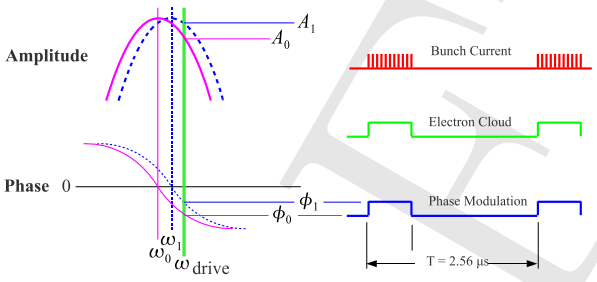

Figure 1.56: Steady state amplitude and phase response as the cavity resonant frequency changes from ω_0 to ω_1

To obtain a rough estimate of the EC density, a number of approximations will be made: that the steady state solution above applies, the drive frequency ω is close to resonance (this results primarily in phase modulation), the phase modulation, from Eq. (1.18) using the measured Q of about 3000, is small and a cw modulation would give a ratio of the first sideband to carrier amplitude of $\frac{1}{2}\Delta\phi$. Also, the phase modulation is not sinusoidal but modulated by the EC density, so a further approximation needs to be made. Let the duration of the EC density *and its effect on the phase* be of fixed amplitude for the length of the bunch train and zero otherwise. Given these crude approximations, Fig. 1.57 is a plot of the EC density measured in the wiggler region at 2 GeV during a wiggler ramp. The stored beam was a positron 45 bunch train spaced at 14 ns with a total current of 35 mA.

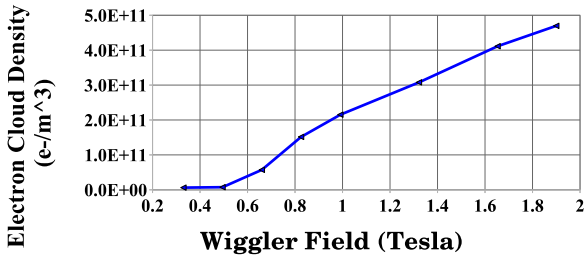

Figure 1.57: Estimate of EC density during a ramp of wigglers

One concern with this approximation is that the beampipe cavity has damping time of about 500 ns. So the duration of the cloud and the damping time of the cavity are of the same magnitude. We are working on a more correct analysis that would include transient effects. For example, a step in the resonant frequency of the cavity at $t = 0$ would be described by

$$x(t<0) = A_0 sin(\omega t + \phi_0) \tag{1.19}$$

$$x(t\geq 0) = A_1 sin(\omega t + \phi_1) + e^{-\gamma t}[A_0 sin(\omega_1 t + \phi_0) - A_1 sin(\omega_1 t + \phi_1)]. \tag{1.20}$$

For $t \gg 0$, the exponential vanishes and only the first term (steady state) remains. In the steady state solutions for $t < 0$ and $t \gg 0$ there is a difference both in the amplitude $A_0 \rightarrow A_1$ and in phase $\phi_0 \rightarrow \phi_1$. But, especially near the resonant frequency, the amplitude change will be quite small and the phase difference will dominate the signal.

The two terms in the brackets are at the new resonant frequency ω_1. For small changes in amplitude and phase this term will be close to zero and decays exponentially with time. To get a better sense of its effect, suppose that the drive frequency ω is between the old and new resonant frequencies. Then the amplitudes $A0$ and A_1 will be nearly equal.

Using the $A_0 \approx A_1$ and the trig identity $sin(a) - sin(b) = 2[cos(\frac{a+b}{2})sin(\frac{a-b}{2})]$,

$$\begin{aligned}
x(t) &= A_1 sin(\omega t + \phi_1) + e^{-\gamma t}[A_0 sin(\omega_1 t + \phi_0) - A_1 sin(\omega_1 t + \phi_1)] \\
&\approx A_1 sin(\omega t + \phi_1) + A_1 e^{-\gamma t}[sin(\omega_1 t + \phi_0) - sin(\omega_1 t + \phi_1)] \\
&\approx A_1 sin(\omega t + \phi_1) + 2A_1 e^{-\gamma t}[cos(\omega_1 t + \frac{(\phi_0 + \phi_1)}{2})sin(\frac{(\phi_0 - \phi_1)}{2})] \\
&= A_1 sin(\omega t + \phi_1) - 2A_1 e^{-\gamma t}[cos(\omega_1 t + \frac{(\phi_0 + \phi_1)}{2})sin(\frac{(\phi_1 - \phi_0)}{2})] \\
&\approx A_1 \left\{ sin(\omega t + \phi_1) \; - \; [\phi_1 - \phi_0]e^{-\gamma t} cos(\omega_1 t + \frac{(\phi_0 + \phi_1)}{2}) \right\}.
\end{aligned} \tag{1.21}$$

So the term that contains the new resonant frequency is multiplied by the phase difference before/after the change in resonant frequency, which is small. So the change in signal will be primarily that of a phase (and amplitude) shift.

The expression of Eq. (1.21) is more or less of the form $Asin(x) + Bcos(x)$. This should be worked out in detail, but for the moment: for $\omega \approx \omega_1$ and ignoring the fact that the phase terms are not quite equal,

$$\begin{aligned}
&\approx A_1 \left\{ sin(\omega t + \phi_1) \; - \; [\phi_1 - \phi_0]e^{-\gamma t} cos(\omega_1 t + \frac{(\phi_0 + \phi_1)}{2}) \right\} \\
&\approx\approx A_1 sin[\omega t + \phi_1 - (\phi_1 - \phi_0)e^{-\gamma t}] \\
&= A_1 sin[\omega t + \phi_1(1 - e^{-\gamma t}) + \phi_0 e^{-\gamma t}].
\end{aligned} \tag{1.22}$$

With all of these approximations, this looks like a rotation of the phase angle from ϕ_0 to ϕ_1 over the damping time. This will have the effect of adding transitions to both the rising and trailing

edges of the phase modulation shown in Fig. 1.56, and have a corresponding effect on the Fourier transform of the modulation.

1.2.1.3 TE Wave Alternative Techniques

Finally, we give some other examples of measurements connected to alternative techniques we are developing.

The Cutoff Resonance Bench measurements were made using WR284 waveguide which has a cutoff frequency very similar to the beampipe of CesrTA near 2 GHz. A 4 meter long section was driven near its longitudinal center using buttons similar in geometry to those in CesrTA. Using metal blocks near the waveguide ends to generate reflections, cavity modes were excited. The $\Delta f \propto E^2$ of these modes were plotted vs. longitudinal position using a dielectric bead, making use of Eq. (1.13) and observing the shifts in resonant frequencies. For measurements with a uniform waveguide, the resonances showed E^2 varying as multiples of half wavelengths, including the lowest $n = 1$ mode.

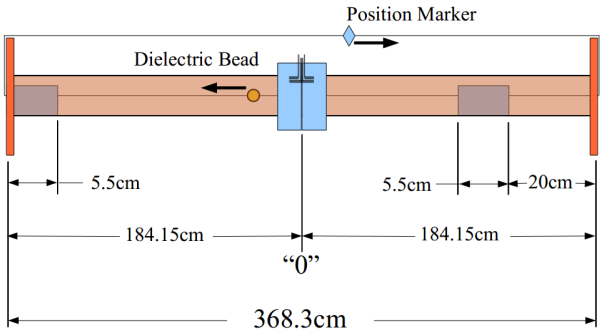

Figure 1.58: For bead pull measurements, a thin monofilament line varies the position of a dielectric bead in WR284 waveguide. The center flange has BPM-like buttons that are used to couple microwaves in/out of the waveguide.

However, a slight modification of the flange used at the drive point resulted in a significant change in the bead pull measurement of the lowest resonance as shown in Fig. 1.62. The inside width of the drive point flange was made 3 mm wider than the waveguide. This portion of the flange is about 2cm long. The lowest '$n = 1$' resonance was then shifted slightly below the cutoff frequency. But rather than a half-sine wave, it has a response consistent with an exponential decrease in E, as with an evanescent wave.

If excited in this mode, the response to EC density will occur over a distance of only about two meters and provide a very localized measurement, following Eq. (1.15). This can be a great advantage, especially when trying to cross calibrate with other localized EC density measurement techniques.

There are many details about this cutoff mode that we need to understand. Primarily, we need to be able to tell - without performing a bead pull experiment in the storage ring - whether or not we have excited this resonance vs. the usual half wave $n = 1$ cavity mode. One indication should be

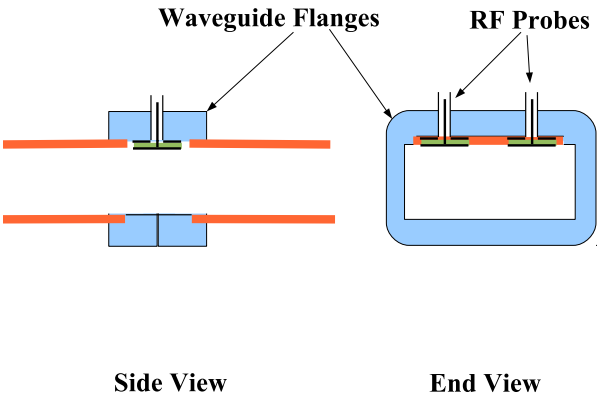

Figure 1.59: Sketch of straight drive flange

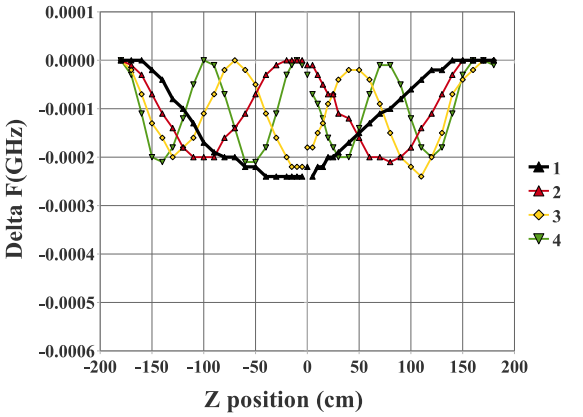

Figure 1.60: Multiple half-wavelength resonances are observed in a section of WR284 waveguide.

the effect on the sequence of resonant frequencies and the extent to which they are different from $f^2 \propto n^2$. For example, the $n = 1$ resonance should be lower than normally expected.

At present, an extensive archive of resonant BPM measurements is available and efforts are underway (Ref [49, 51, 55]) for a full theoretical model of the relationship between sidebands amplitude and electron cloud density in these conditions.

TE Magnetic Resonance During measurements in the chicane in the L3 region we observed a strong enhancement in the modulation sidebands in correspondence of the upper hybrid resonance, when propagating a TE wave polarized with its electric field normal to the chicane magnetic field.

Figure 1.63 shows the change in modulation sideband amplitude when the chicane magnetic field is changed so that the TE wave frequency corresponds to the upper hybrid frequency $\omega_{uh} = \sqrt{\omega_p^2 + \omega_{cycl}^2}$ for the electron cloud plasma. Because in all practical situations, for a wave above cutoff, $\omega_p << \omega_{cycl}$ making the evaluating the plasma frequency from the upper hybrid frequency measurement problematic, we are currently studying the phenomenon for waves below cutoff. Preliminary results give us the hope of being able to effectively turn on and off transmission between two BPMs by applying a relatively small dipole magnetic field to the portion of vacuum chamber between them. This could be easily achievable by employing external air-coil magnets, for instance. At that point, the evaluation of the electron cloud density in that region would essentially reduce to the measurement of a resonance peak.

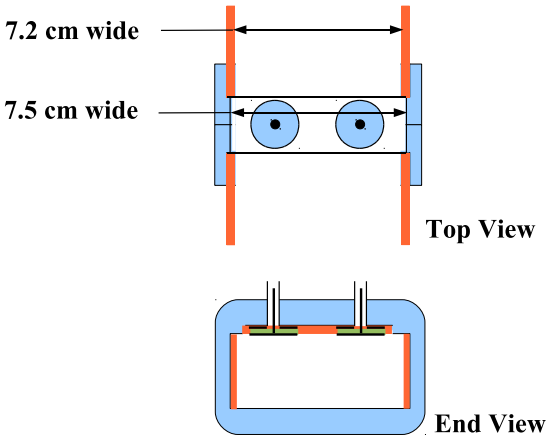

Figure 1.61: Sketch of drive flange modification.

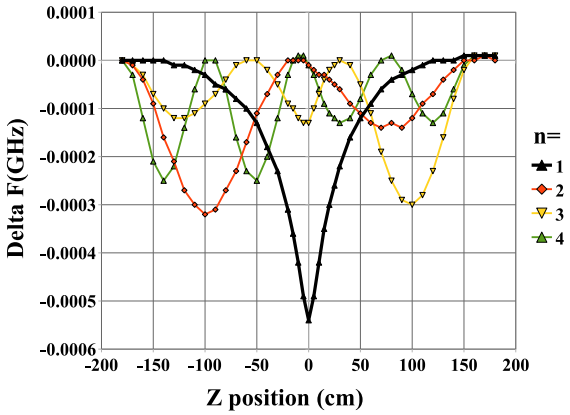

Figure 1.62: The cutoff resonance was observed using a modified drive flange in a measurement with WR284 waveguide.

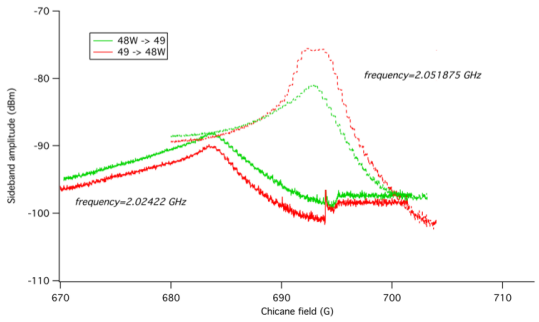

Figure 1.63: Modulation sideband amplitude near the upper hybrid resonance at two different frequencies. Red and green traces correspond to opposite direction of propagation of the TE wave.

1.2.1.4 TE Wave Modeling

1.2.2 Shielded Pickup Studies

1.2.2.1 Measurements

Time-resolved shielded-pickup measurements provide time structure information on cloud development, in contrast to the time-integrated RFA measurements [59]. However, they have relatively primitive energy selection, since they have no retarding grid and position segmentation is more coarse, the charge-collecting electrodes being of diameter 18 mm. Data has been recorded with biases of 0 and ±50V relative to the vacuum chamber. The studies described here address exclusively the data a with bias +50 V in order to avoid contributions to the signal from secondary electrons escaping the pickup. Such secondaries generally carry kinetic energy insufficient to escape a 50 V bias. This choice of bias obviously provides sensitivity to cloud electrons which enter the port holes with low kinetic energy. The front-end readout electronics comprise RF amplifiers with 50 Ω input impedance and a total voltage gain of 100. Digitized oscilloscope traces are recorded with 0.1 ns step size.

Two Bunch Data The data shown in Fig. 1.64 was taken with two bunches of equal positron currents, 36ns apart. With a ring revolution period of 2.5 μs, the cloud has presumably fully decayed by the time of the arrival of the first bunch. This first bunch produces a fairly small signal in the detector. The signal from the second bunch is much larger, not because it has produced more photoelectrons, but because its electric field kicks electrons that were produced by the first bunch into the detector.

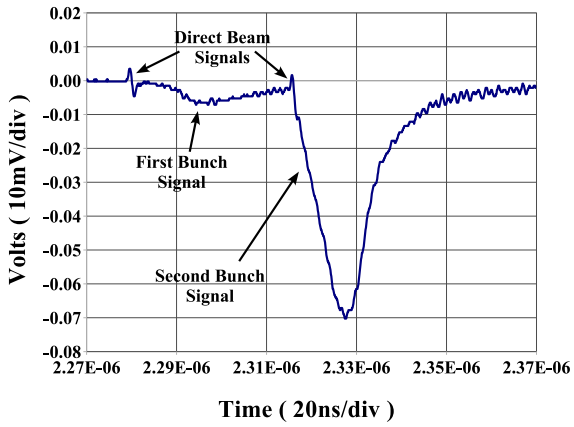

Figure 1.64: Shielded pickup signal from two bunches of positrons spaced at 36 ns

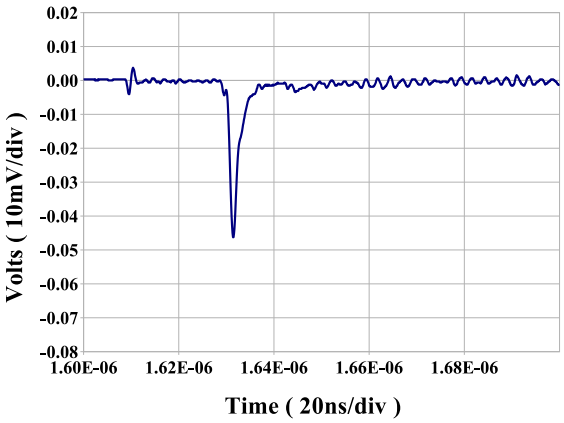

Figure 1.65: The signal from two bunches of electrons spaced at 20 ns

Another feature of the plot in Fig. 1.65 is the presence of what is presumed to be a small direct beam signal. The geometry of the detector holes give reasonably good (but not complete) isolation from the electromagnetic field of the beam. This signal provides a convenient fiducial that can be used to measure the time-of-flight of cloud electrons.

For example, notice that the peak of the signal from the first bunch occurs about 15 ns after its direct beam signal. Given the detector geometry, most of these electrons must be coming from the floor of the beampipe, a distance of 5 cm, which would require an energy of roughly 30 eV.

After the passage of the second positron bunch in Fig. 1.64, the cloud electrons enter the detector almost immediately. Since this is a positron beam, the electrons kicked into the detector must come from below the beam height in the chamber, at least 2.5 cm from the detector. These initial electrons must have energies of many hundreds of eV and originate close to the beam.

Fig. 1.65 is the signal produced by two electron bunches spaced at 20 ns. Notice that the signal from the first bunch is not visible (except for the direct beam signal) and that the signal from the second bunch has a faster rise time than that of a positron beam.

Two Bunches with Different Spacings The much larger signal after the passage of the second bunch suggests that this signal is dominated by cloud electrons that are already in the pipe and are being kicked into the detector. This kick has an effective duration that is set by the sum of the length of the bunch and the size of the button, about 120 ps. So the second bunch signal is effectively a sample of the electron cloud in the chamber at the time of the second bunch's transit. Following this idea, pairs of bunches with equal currents were injected with different spacings. The result was a mapping of the electron cloud density produced by the first bunch as a function of

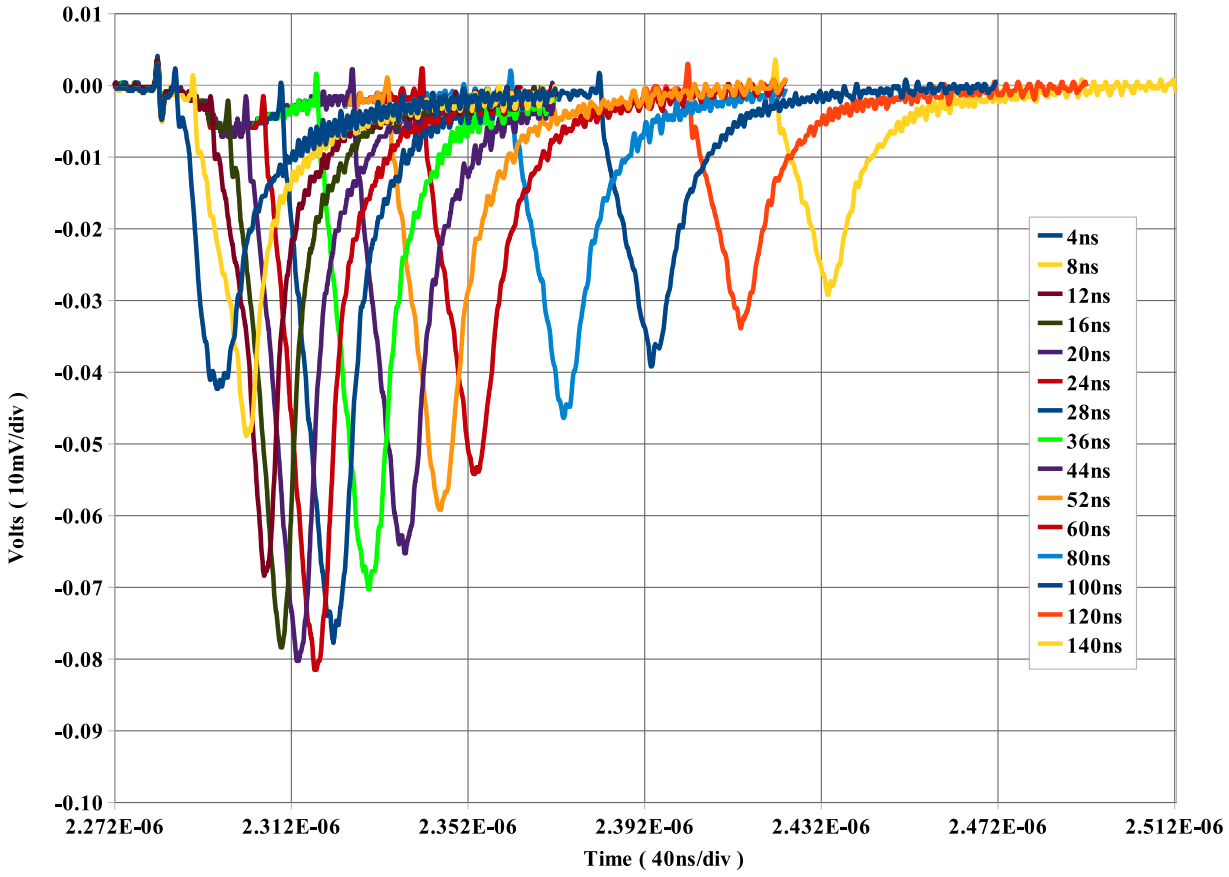

Figure 1.66: Overlay of two bunch data with spacings in multiples of 4 ns at 2.1 GeV with an aluminum chamber

time as the second bunch samples the cloud. In Fig. 1.66, a number of these measurements are plotted on the same time scale, showing the decay of the cloud.

Single Bunch with Solenoid When the solenoid surrounding the shielded pickup is energized, there is a noticeable effect on the detector signal that generally depends on the sign of the magnetic field. The four plots in Fig. 1.67 show the signal vs. solenoid field for 15E, 15W, both with positron and electron beams. In the top left plot of Fig. 1.67 there is a large signal when the sign of the magnetic field positive. This positive magnetic field is such that primary electrons produced at the outside wall would be directed upward into the detector. It is likely that this signal is due to the synchrotron light stripe in the mid-plane of the beampipe producing a concentration of photoelectrons along that stripe. The magnetic field that gives the largest signal, -14 G, can be used to estimate the electron energy at approximately 150 eV.

So when used with a solenoid, the 15E detector seems to function as a crude spectrometer with an electron bunch. However, data from positrons at 15E or either beam at 15W is inconsistent with this simple interpretation. So while there is hope that the use of a solenoid field can give useful information about electron energies, there are inconsistencies in data interpretation that need to

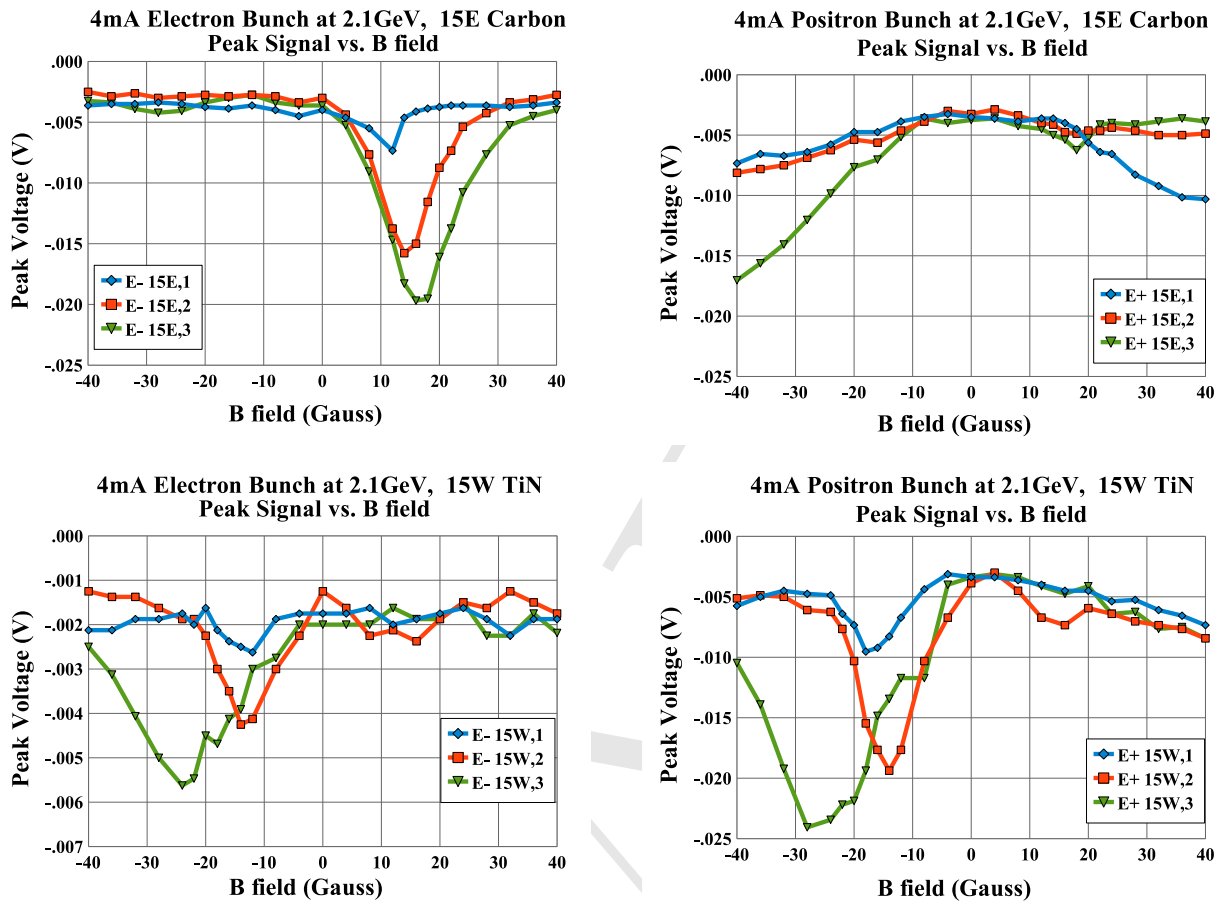

Figure 1.67: Pickup signal vs. solenoid field with a single bunch

be resolved through more careful modeling.

1.2.2.2 Shielded Pickup Modeling

Sensitivity to Photoelectron Energy Distribution The upper row of Fig. 1.68 shows examples of shielded pickup signals for two bunches of 5.3 GeV positrons (left) and electrons (right) separated by 14 ns. The population of the first bunch is $1.3x10^{11}$ while that of the trailing bunch varies up to a similar value. The trailing bunch accelerates cloud particles into the detector, producing the second signal. The arrival time and structure of the earlier signal corresponds to photoelectrons produced at the time of bunch passage on the lower chamber wall. The kick from the positron bunch accelerates such photoelectrons toward the detector, whereas in the case of an electron beam the signal electrons must carry sufficient kinetic energy to overcome the repulsion of the beam bunch.

The lower row of Fig. 1.68 shows an initial attempt to model the case of two 1.3E11e bunches using the electron cloud simulation code ECLOUD [39]. The calculation of cloud kinematics including space charge forces and beam kicks determines arrival times, momentum vectors and charges of the macroparticles reaching the upper surface of the chamber at the positions of the pickups. This early attempt at simulating the observed signals included a rather crude model of the port hole

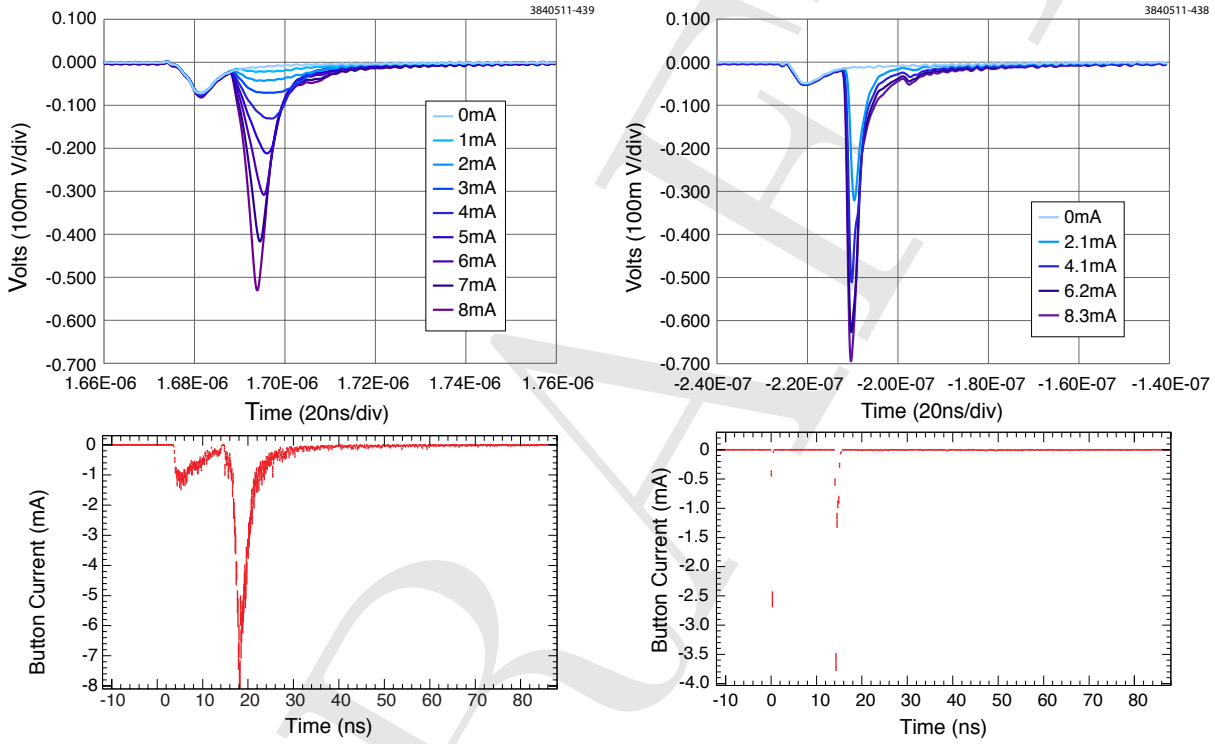

Figure 1.68: Upper row: shielded pickup signals produced by two 5.3 GeV positron (left) and electron (right) bunches separated by 14 ns. The leading bunch population is 1.3E11e . The population of the second bunch varies up to a similar value. Lower row: initial ECLOUD model results exhibiting discrepancies with the measured signals which are quite dramatic in the case of the electron beam.

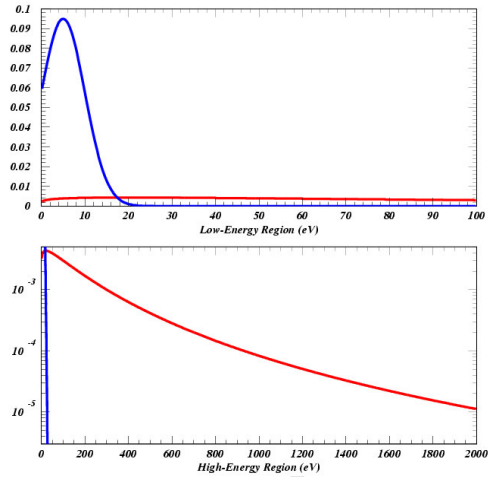

Figure 1.69: Low- and high-energy regions of the photoelectron energy distributions used to model the measured signals shown in Fig. 1.68. The original low-energy distribution shown in blue results in dramatic discrepancy with the signals observed in the case of an electron beam. The modified distribution shown in red provides good agreement with the observed signals.

acceptance, leading to poor approximation of the magnitude of the signal, but it was sufficient to diagnose the obviously discrepancy with the observed signals. The positron case shows moderate time structure differences, but the modeling of the electron beam kick exhibited a dramatic discrepancy. The arrival times of the observed signals indicate photoelectron production on the lower wall of the chamber, which is effected in the simulation via a reflectivity parameter distributing 20% of the photoelectrons uniformly in azimuth. The prompt signal from each electron bunch corresponds to photoelectrons produced on the upper wall repelled into the detector during the bunch passage. The photoelectrons produced on the lower wall in the ECLOUD simulation are similarly reabsorbed, and these are the ones needed to produce the observed signal! In other words, the measurement shows that photoelectrons of sufficient energy to overcome the repulsion of the beam bunch must be present. The photoelectron energy distribution in this original default model is common to many successful simulations of a wide variety of experimental observations [39, 60, 61], namely a gaussian with average and rms values of 5 eV limited by truncation to positive values. Figure 1.69 compares such a distribution (blue) to a power-law modification adequately reproducing the observed signal shapes (red). Low-energy and high-energy regions are shown normalized on logarithmic scales to illustrate the dramatically higher energies needed.

This new high-energy distribution was determined by matching single-bunch models to the measured signals for various electron bunch currents as shown in Fig. 1.70. The measured signals for a single bunch of 5.3 GeV electrons are shown in the left column. A bunch current of 1 mA corresponds to a bunch population of $1.6x10^{10}$. The model successfully reproduces the increase of signal magnitude with bunch current. While some time structure discrepancies remain, the improvement relative to the results shown in Fig. 1.68 is remarkable. The overall normalization of the modeled signals is proportional to the assumed reflectivity value, which in this case was 20%. In addition, the model also exhibits a prompt signal arising from photoelectrons produced nearby the detector repelled into it during the passage of the bunch, increasing with bunch current similarly to the observed signals.

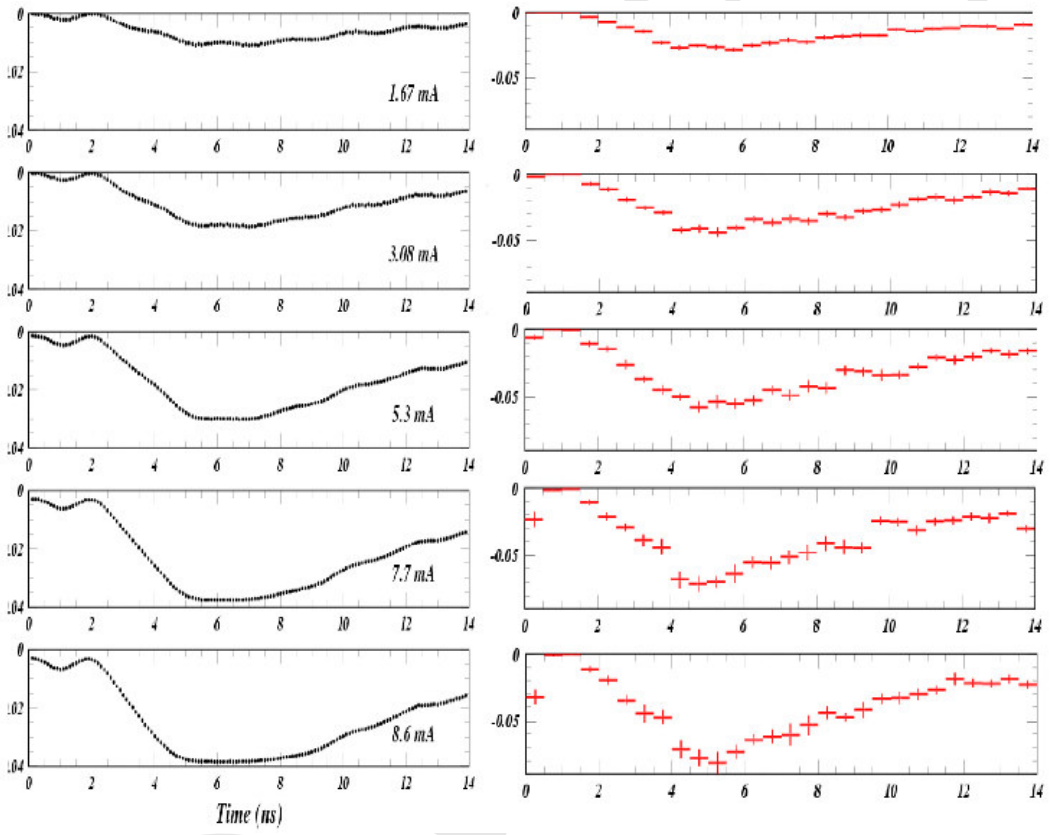

Figure 1.70: Comparison of measured single bunch signals for various electron bunch currents (left column) to the ECLOUD model (right column) after improving the modeled photoelectron energy distributions.

Detailed Photoelectron Energy Modeling using Bunch Current Scans A detailed model of the photoelectron kinetic energy distribution for photoelectrons produced by reflected photons can be obtained by exploiting SPU data recorded for different bunch current levels. The early SPU signal from the leading bunch for a positron beam is largely due to photoelectrons produced on the bottom of the vacuum chamber. This is the closest production point where the beam kick attracts the photoelectrons toward the SPU. Thus the size and shape of the leading bunch signal is determined by the reflected photon rate, azimuthal distribution, the quantum efficiency for producing photoelectrons, the kinetic energy distribution of the photoelectrons and the strength of the attractive beam kick for a positron beam. In particular, the arrival time distribution determines the shape. By modeling the shape for different strengths of beam kick, we can extract the photoelectron energy distribution. An example of such an analysis is shown in Fig. 1.71. Note that the signal begins just a few nanoseconds after bunch passage even for weak beam kicks, indicating that high-energy photoelectrons were produced (hundreds of eV).

This level of modeling accuracy was achieved with a photoelectron energy distribution, consisting of the sum of two power law distributions each parameterized by values of P_1, P_2, and E_0:

$$f(E_{pe}) \propto \frac{E_{pe}^{P_1}}{\left(1+\frac{E_{pe}}{E_0}\right)^{P_2}} \tag{1.23}$$

where the parameter E_0 is related to the value of the energy at the maximum of the distribution E_{peak} by

$$E_0 = E_{peak}\frac{P_2 - P_1}{P_1} \tag{1.24}$$

The high-energy component (22%) has a peak energy of 80 eV and an asymptotic power of 4.4 ($P_1 = 4$, $P_2 = 8.4$). Its contribution to the signal is shown as yellow circles in Fig. 1.72. The low-energy component (78%) has a peak energy of 4 eV and an asymptotic power of 2 ($P_1 = 4$, $P_2 = 6$). It's contribution to the signal is shown as pink triangles. The model with the combined energy distribution is shown on three horizontal scales in Fig. 1.73. Note that these comparisons are complicated by the fact that the cloud development for a single photoelectron component is unrealistic. The approximate validity of the superposition shows that space charge forces are weak, as is any contribution from photoelectrons produced at the primary source point on the outside wall of the chamber.

This analysis presents an opportunity to relate the obtained photoelectron energy distribution to the incident synchrotron energy spectrum and thus derive an estimate of the energy dependence of the quantum efficiency. For example, the power law contributions have been determined in this manner for 2.1 GeV positron beams, showing that the high-energy tails are greatly reduced [62]. These studies also allow us to draw qualitative conclusions on the photoelectron energy distributions for various coatings, as described below in the section on vacuum chamber comparisons under under the same beam conditions and radiation environment.

Since these studies pertain to photoelectrons produced by reflected synchrotron radiation photons, the incident photon energy spectrum is a convolution of the critical energy at the source and the energy dependence of the reflection process. Detailed work on modeling reflected photon trajectories is underway [63, 64].

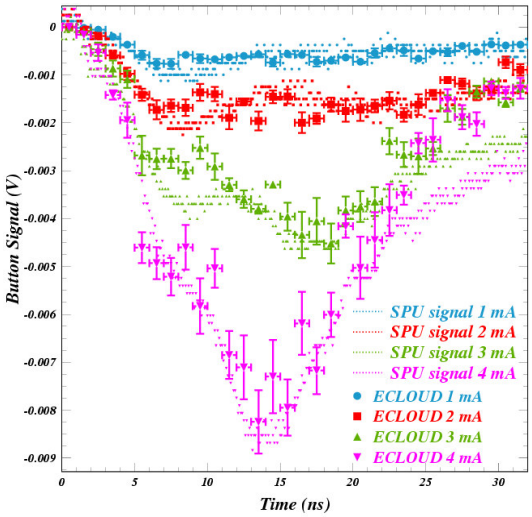

Figure 1.71: Modeled and measured leading SPU signals for bunch currents of 1, 2, 3 and 4 mA/bunch. The dramatically varying amplitudes and shapes are successfully reproduced by tuning the modeled photoelectron energy distribution as described in the text.

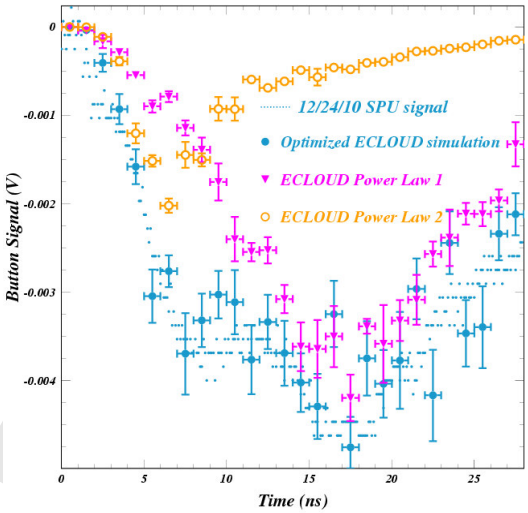

Figure 1.72: Two power-law contributions to the modeled photoelectron energy distribution. The yellow circles show the contribution to the signal from the high-energy photoelectron component, and the magenta triangles the low-energy contribution. The combined result is shown in blue.

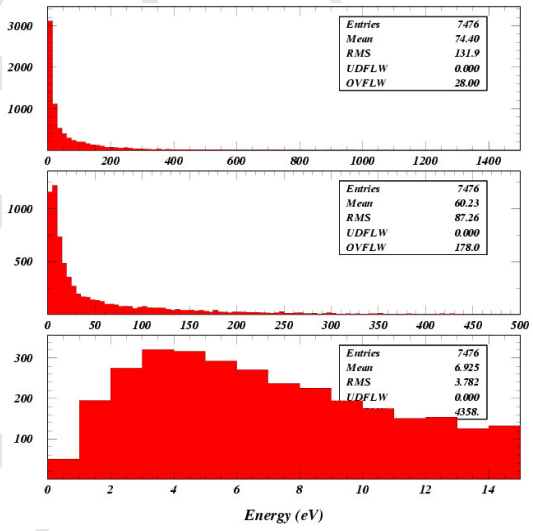

Figure 1.73: Modeled photoelectron energy spectrum resulting from the weighted contribution of the two power laws

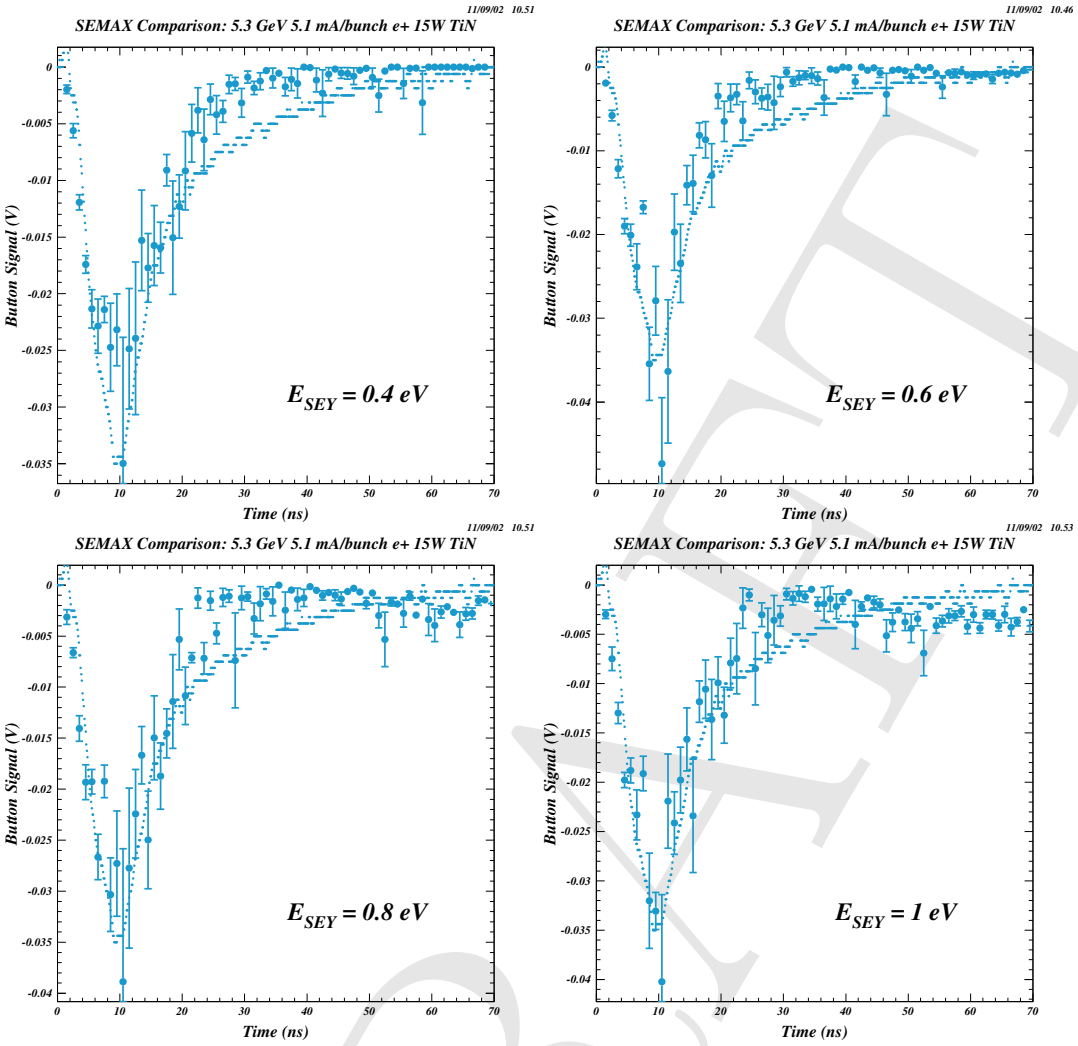

Figure 1.74: Modeled and measured leading SPU signals with differing distributions for the parameter E_{SEY} ranging from 0.4 to 1.0. For values greater than 0.8, a late tail appears in the signal, inconsistent with the measured signal.

Constraints on the Production Energy Distribution for Secondary Electrons Long after the photoelectrons from the bottom of the beampipe have produced the peak of the leading bunch signal, secondary electrons produced by photoelectrons from the primary source point in the horizontal midplane on the outside wall of the chamber begin to enter the shielded pickup detector. Their arrival times depend on many characteristics of the model, such as the photoelectron energy distribution for direct (unreflected) photons, their production angular distribution, and, in particular, the energy and production angle distribution of the secondaries. The ECLOUD code provides for a variety of secondary energy distribution parameterizations, many of which could be excluded by studies such as the one shown in Fig. 1.74. For the best parameterization,

$$f(E_{\mathrm{sec}}) \propto E_{\mathrm{sec}} \exp(-E_{\mathrm{sec}}/E_{\mathrm{SEY}}) \tag{1.25}$$

an upper bound was obtained on the parameter E_{SEY}, which determines the falling exponential slope. A high-energy tail produces a late signal inconsistent with the measured signals.

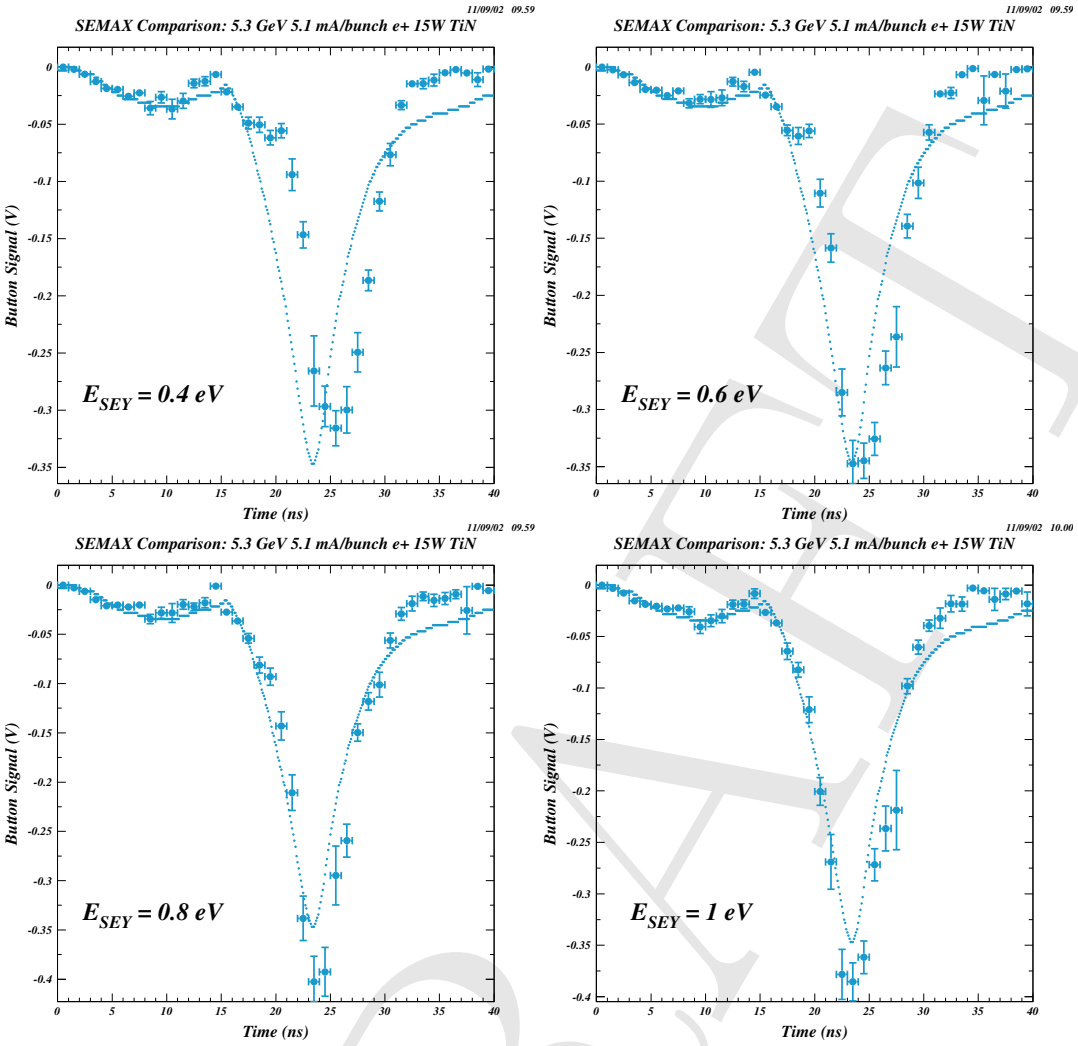

Figure 1.75: Modeled and measured 14-ns witness signals with values for the parameter E_{SEY} ranging from 0.4 to 1.0. For values less than 0.8, the signal shape is distorted in a manner inconsistent with the measured signal.

The signal from a witness bunch following 14 ns after the leading bunch also has a contribution from reflected photons similar to the one that dominates the leading bunch signal. However, it includes additionally a much larger contribution from secondary cloud electrons accelerated into the SPU detector by the witness-bunch kick. Those present near the vertical plane containing the beam below the horizontal midplane at the time the witness bunch passes can arrive even earlier than the photoelectrons from the bottom of the beampipe. Figure 1.75 shows that if the secondary energy distribution does not include sufficiently high energies, the modeled 14 ns witness bunch signal shape is distorted and inconsistent with the measured signal.

Remarkably, the two constraints on the secondary electron production kinetic energy distribution described above restrict the E_{SEY} parameter to a narrow range of values around 0.8 eV.

Cloud Lifetime Studies Using Witness Bunches While the awareness of the sensitivity of the shielded pickup measurements to the parameters of photoelectron production was largely motivated by inadequacies of the model discovered in its application to recent measurements, the original intended use of these time-resolved cloud measurements was to provide a quantitative estimate of the elastic yield parameter in the secondary electron yield model. A similar investigation was performed at RHIC [65]. The basic concept is that the mature cloud long after passage of any beam bunch is dominated by low-energy electrons which suffer predominantly elastic interactions with the vacuum chamber wall. The elastic yield parameter describes the ratio of outgoing to incoming macroparticle charge in probabilistic models [34], and carries a value typically 0.5-0.7, determining the decay time of the cloud density, typically around 100 ns. High-energy electrons of more than 100 eV, produced by synchrotron radiation, beam kicks, or the rediffused component of the secondary yield process, undergo primarily the so-called "true" secondary yield process, in which the produced secondary carries only a few electron volts of kinetic energy, resulting in the dominance of low-energy electrons late in the cloud development.

Figure 1.76 shows an ECLOUD secondary yield population curve typical of the shielded pickup signal simulations.The true secondary yield maximum at 400 eV ranges from a minimum of 0.9 to a maximum of 1.5 owing to the dependence on incident angle. At low energy the yield value is dominated by the elastic interactions with the chamber wall. This case exhibits an elastic yield parameter of 0.55.

The witness bunch experimental method consists of generating a cloud with a leading bunch, then accelerating cloud electrons into the shielded pickup detector with a trailing bunch at various delay times. Table 1.7 shows the witness bunch data sets which were recorded from March, 2010 through June, 2011. Additional data sets with delay times restricted to 14 ns and 84 ns at bunch currents of 1, 2, 4, 6, and 8 mA were also taken for systematic checks of the modeling.

The magnitude and time structure of the signal from the leading bunch is determined by the reflective properties of the vacuum chamber and by the energy-dependent quantum efficiency, as described in the preceding section. The signal induced by the witness bunch has a contribution similar to that of the leading bunch added to the contribution from the existing cloud kicked into the detector. The latter contribution is sensitive to the cloud density and the spatial and kinematic distributions of the cloud electrons. Figure 1.77 shows the results of six sets of simulations with various values for the elastic yield parameter δ_0. In each of the six plots, eleven two-bunch (5.3 GeV, 4.8E10e positrons each) pickup signals are superposed, whereby the delay of the witness bunch varies from 12 to 100 ns. The modeled signals are shown with the statistical error bars corresponding to the number of macroparticles contributing to the signal. The magnitudes of the modeled signals at large witness bunch delay clearly show the dependence on the elastic yield parameter δ_0 as it is varied from 0.05 to 0.75. The most consistent description of the measured signals is given by a value of $\delta_0 = 0.75$. This value can be compared to the value of $\delta_0 = 0.5$ used in the modeling of CesrTA coherent tune shift measurements as described in Refs. [60, 61], where the measurements had much less discriminating sensitivity to the elastic yield.

Figure 1.78 shows a similar study, but for a titanium-nitride-coated aluminum chamber. For each of the six values assumed for the elastic yield, thirteen two-bunch (5.3 GeV, 8.0E10e positrons each) pickup signals are superposed, whereby the delay of the witness bunch is varied from 14 to 84 ns. The optimal value for the elastic yield is clearly less than the value determined for the uncoated aluminum chamber, with $\delta_0 = 0.05$ providing the best description of the measurements.

These comparisons show a number of intriguing discrepancies. The leading bunch signal shape

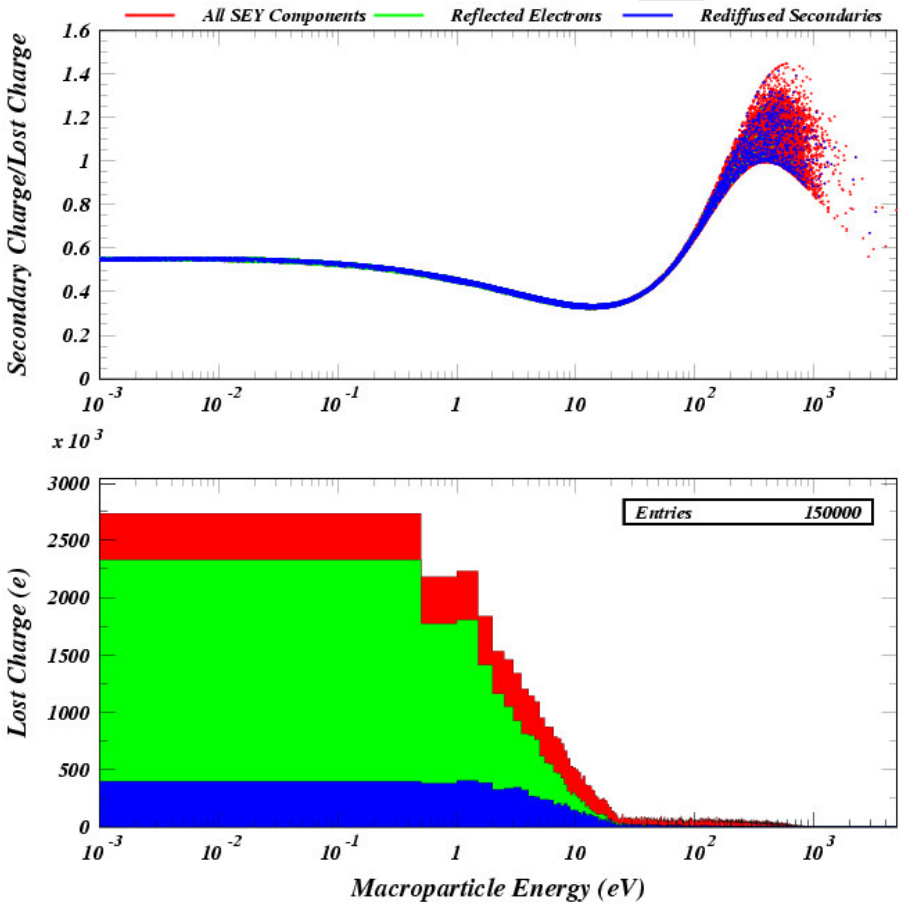

Figure 1.76: Secondary yield population curve typical of the ECLOUD model for the shielded pickup signals. The upper plot shows the yield value (ratio of secondary macroparticle charge to that of the incident charge) as a function of the incident kinetic energy. At low energy the yield value is dominated by the elastic interaction with the chamber wall. This case exhibits an elastic yield parameter of 0.55. The lower plot shows the incident energy distribution. The elastic and rediffused components are shown in green and blue, respectively. The sum of all three components, true, elastic and rediffused, is shown in red. Since the three colors are plotted on top of each other, the upper plot shows primarily blue at low energy, even though the elastic process dominates, as is seen in the lower plot.

Table 1.7: Shielded pickup witness bunch data sets recorded from March, 2010 through June, 2011. Note that the various cloud-mitigating coatings (TiN, a-carbon, and diamond-like carbon) were swapped into the different radiation environments at 15E and 15W. Data sets with differing total radiation dose were obtained as well. Two vacuum chambers with a-carbon coatings were studied, providing information on production reproducibility.

Date	Species	Beam Energy (GeV)	Bunch Current (mA)	15E/W	Mitigation Technique	Bunch Spacing (ns)
03/27/2010	Positrons	5.3	5	W	a-Carbon (1)	14-84
				E	TiN	
	Electrons		5	W	a-Carbon (1)	14-70
				E	TiN	
05/09/2010	Positrons	2.1	3	W	Al	4-140
				E	a-Carbon (2)	
	Electrons		3	W	Al	4-20
				E	a-Carbon (2)	
05/17/2010	Positrons	5.3	3	W	Al	4-100
				E	a-Carbon (2)	
	Electrons		3	W	Al	4-100
				E	a-Carbon (2)	
05/19/2010	Electrons	2.1	1	W	Al	4-120
				E	a-Carbon (2)	
12/24/2010	Positrons	5.3	3, 5	W	TiN	14-84
				E	a-Carbon (2)	
	Electrons		3, 5	W	TiN	14-84
				E	a-Carbon (2)	
04/07/2011	Positrons	5.3	3, 5	W	TiN	14-84
				E	DL Carbon	
	Electrons		3, 5	W	TiN	14-84
				E	DL Carbon	
04/16/2011	Positrons	2.1	3, 5	W	TiN	14-84
				E	DL Carbon	
04/17/2011	Electrons		3, 5	W	TiN	14-84
				E	DL Carbon	
06/11/2011	Positrons	2.1	3, 5	W	TiN	14-84
				E	DL Carbon	
06/12/2011	Electrons		3, 5	W	TiN	14-84
				E	DL Carbon	
06/18/2011	Positrons	5.3	3, 5	W	TiN	14-84
				E	DL Carbon	
	Electrons		3, 5	W	TiN	14-84
				E	DL Carbon	

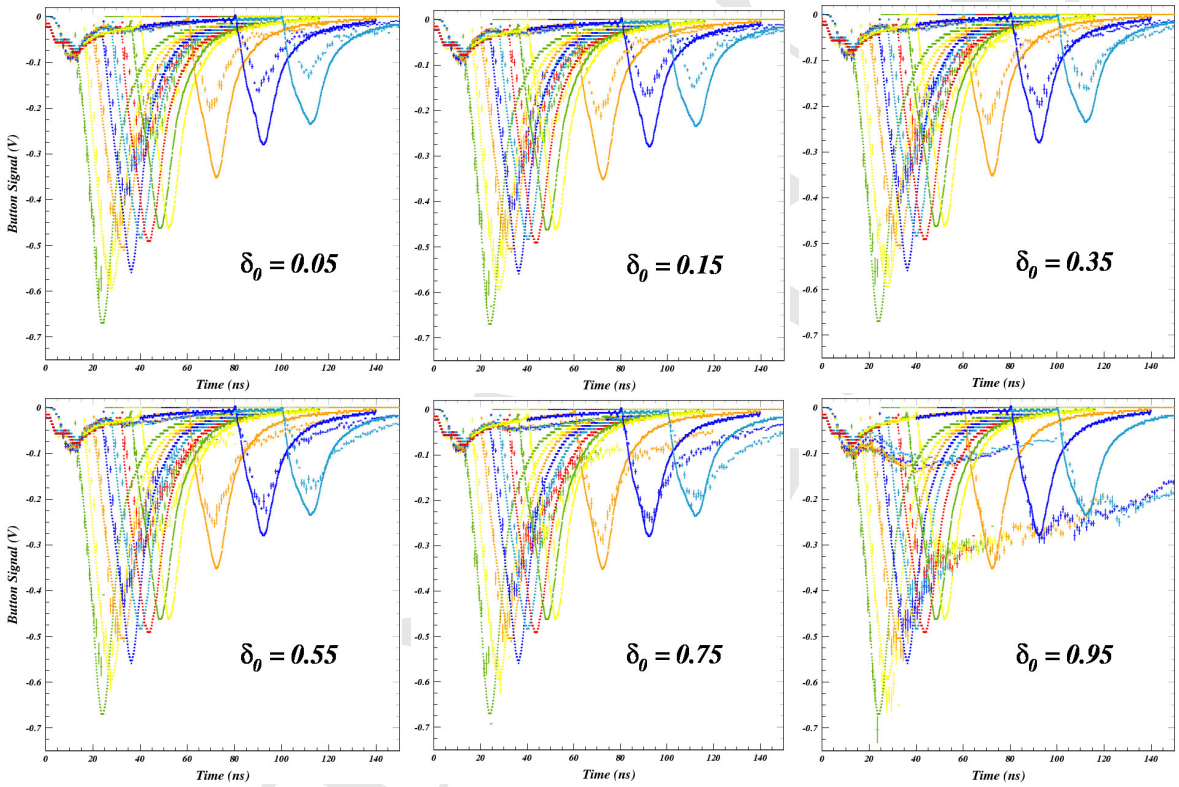

Figure 1.77: Witness bunch study with the uncoated aluminum chamber. Eleven two-bunch scope traces are superposed in each of the six plots, whereby the delay of the witness bunch ranges from 12 to 100 ns. The modeled signals are shown with the statistical error bars corresponding to the number of macroparticles contributing to the signal. The magnitudes of the modeled signals at large witness bunch delay clearly show the dependence on the elastic yield parameter δ_0 as it is varied from 0.05 to 0.75. The most consistent description of the measured signals is given by a value of $\delta_0 = 0.75$.

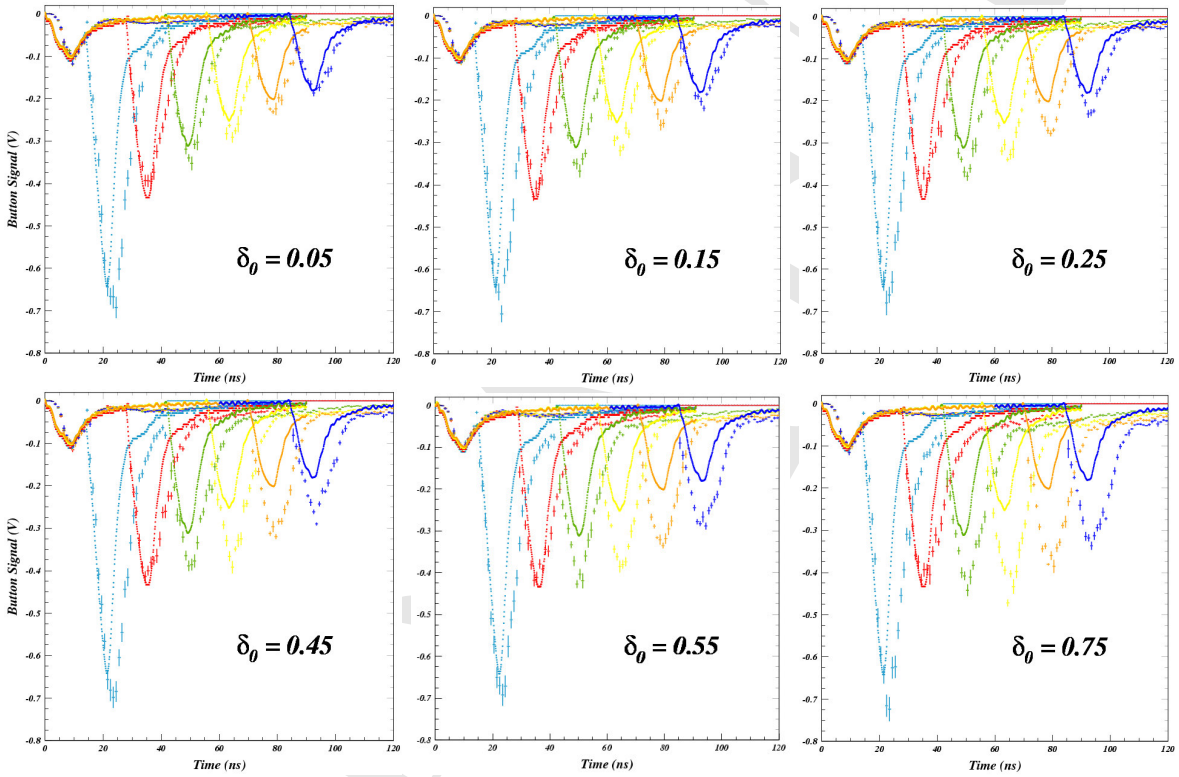

Figure 1.78: Witness bunch study with the titanium-nitride-coated aluminum chamber. The smooth curves are the digitized shield pickup signals. Six two-bunch scope traces are superposed in each of the six plots, whereby the delay of the witness bunch ranges from 14 to 84 ns. The magnitudes of the modeled signals at large witness bunch delay clearly show the dependence on the elastic yield parameter δ_0 as it is varied from 0.05 to 0.95. The most consistent description of the measured signals is given by a value of $\delta_0 = 0.05$.

exhibits the need for further tuning of the photoelectron energy distribution. The signal widths tend to be wider than observed. In addition, such a low value of 0.9 for the secondary yield of an uncoated aluminum surface cannot be easily understood, since the tune shifts measurements require an average value around the CESR ring of about 1.8. A wide variety of systematic studies have been undertaken since the ECLOUD'10 workshop, discovering sensitivity to many detailed characteristics of the cloud. For example, the signal widths for early witness signals depend strongly on the azimuthal production distribution of photoelectrons, as was observed by implementing in ECLOUD the distributions calculated by the photon-tracing reflectivity model for the CESR ring described in Ref. [63]. Nonetheless, the dramatic improvements in consistency obtained via such systematic studies have not changed the quantitative conclusions concerning the sensitivity to the value for the elastic yield. Generally one can say that the choice of peak true secondary yield value relative to the effective reflectivity value determines the ratio of the early witness bunch signal magnitudes to that from the leading bunch. However, for witness bunches late enough that the signal magnitude becomes comparable to that of the leading bunch, there is little sensitivity to the true secondary yield. Instead, those signal magnitudes are determined by the value assumed for the elastic yield.

In situ comparisons of custom vacuum chambers One fruitful analysis strategy has proved to be the comparison of SPU signals in chambers which have been swapped into the same location in the CESR ring and studied under identical beam conditions [66]. The two regions in CESR equipped with SPU detectors differ in radiation environment, since the dominant source points are in dipole magnets of differing strengths. At 5.3 GeV, for example, the source dipole field is 3 kG (2 kG) in the west (east) region for a positron beam, resulting in a critical energy of 5.6 keV (3.8 keV). In addition, the situation with regard to reflected radiation is different. By comparing SPU signals recorded at the same place in the ring with the same beam energy, bunch spacing and bunch population, many systematic contributions to the comparisons are avoided, and relatively simple changes to the modeling suffice to quantify the different properties of the vacuum chambers.

Figure 1.79 shows such a comparison for an a-C-coated chamber in May and December 2010 for two 5.3 GeV 28 ns-spaced bunches each carrying 4.8×10^{10} positrons, corresponding to a bunch current of 3 mA. During the intervening time interval, CESR had operated at high current as an X-ray research facility, with the consequence that synchrotron radiation dose on the chamber had increased by a factor of about 20, from $8.1{\times}10^{23}$ to $1.8{\times}10^{25}$ γ/m. Also shown is the ECLOUD model optimized to reproduce the May measurement. Since the signal from the leading bunch arises from photoelectrons produced on the bottom of the vacuum chamber [66–68], careful tuning of the energy distribution and quantum efficiency (QE) for photoelectrons produced by reflected photons is required to reproduce the size and shape of the signal. The signal from the witness bunch includes additionally the contribution from secondary EC electrons accelerated into the SPU detector by the witness-bunch kick. The modeled witness signal is therefore crucially dependent on the SEY and production kinematics. Since conditioning affects both signals similarly, we can conclude that the change is in the QE rather than in the SEY. The December measurement is reproduced by a 50% decrease in the modeled QE for photoelectron production. A reduction in the SEY of 25% is inconsistent with the observed effect, since the modeled leading bunch signal remains unchanged.

Guided by the above comparisons, we can assess conditioning effects in the TiN- and DL-carbon-coated chambers in similar fashion. Figure 1.80 compares the SPU signals for two 8×10^{10} e^+

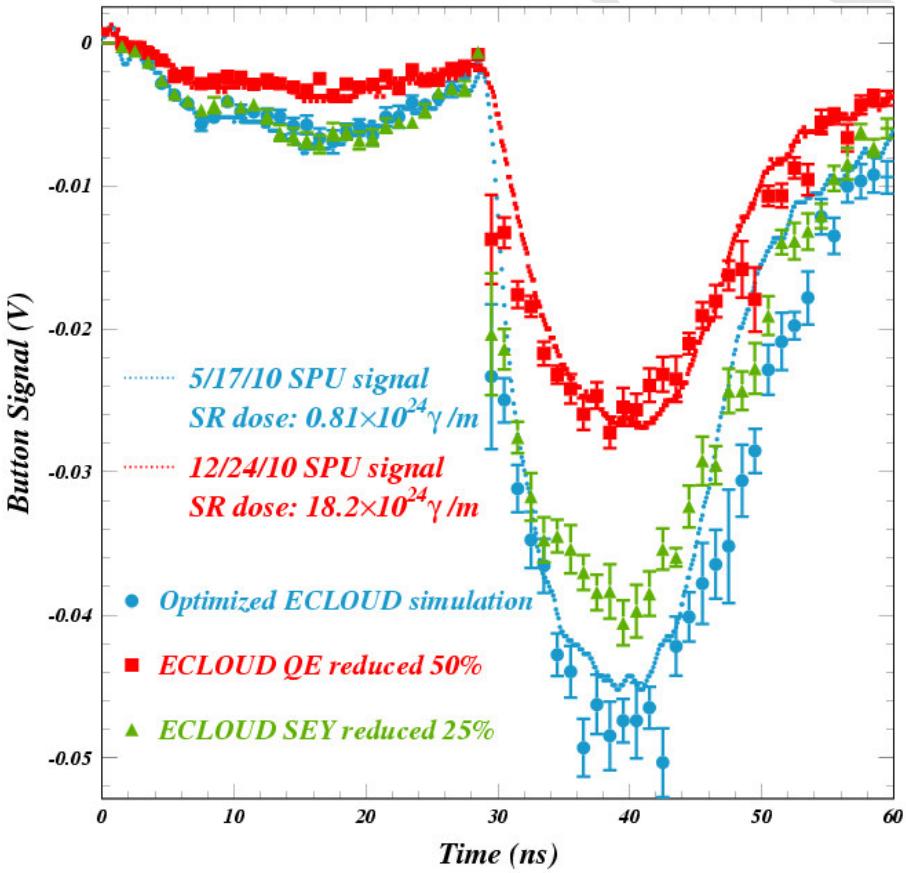

Figure 1.79: Shielded pickup signals measured in an a-C-coated chamber in May (blue dotted line) and December (red dotted line) of 2010 for two 5.3 GeV, 28-ns-spaced bunches each carrying 4.8×10^{10} positrons. The ECLOUD model optimized for the May data is shown as blue circles, the error bars showing the signal macroparticle statistical uncertainties.

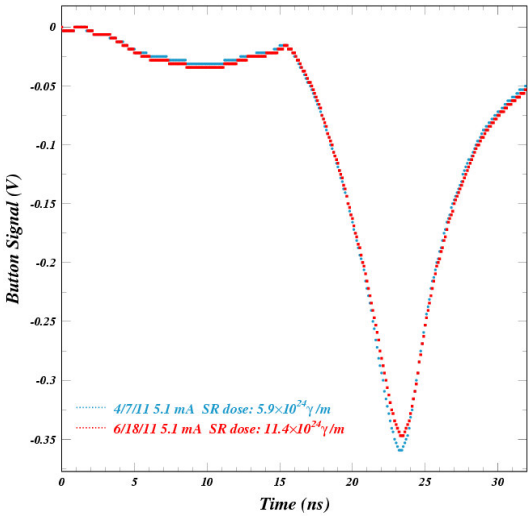

Figure 1.80: SPU signals showing conditioning effects in the TiN-coated aluminum vacuum chamber

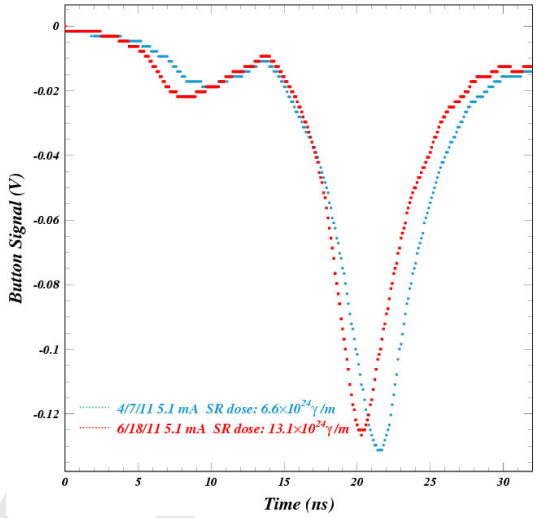

Figure 1.81: SPU signals showing conditioning effects in the aluminum vacuum chamber coated with DL carbon

bunches in the TiN-coated chamber in April and June 2011, with accumulated synchrotron radiation doses of 5.9×10^{24} and 1.1×10^{25} γ/m, corresponding to integrated beam currents up to more than 730 amp-hours. Changes in the QE and SEY are less than a few percent. The conditioning effects in the DL-carbon-coated vacuum chamber are quite different, as shown in Fig. 1.81. Conditioning effects are clearly observed for a radiation dose increasing from 6.6×10^{24} to 1.3×10^{25} γ/m, corresponding to 370 and 730 amp-hours. Remarkably, the size and risetime of the signal from the leading bunch increased, indicating that the QE for photoelectrons produced by reflected photons increased somewhat, and that more photoelectrons were produced at higher kinetic energies. Despite the increase in photoelectron production, the signal from the witness bunch decreased, showing that the conditioned SEY is significantly lower. Future modeling efforts will provide quantitative estimates for these changes.

The method of in situ comparison of custom vacuum chambers can also be used to compare the characteristics of different mitigation techniques. Figure 1.82 compares signals from a TiN-coated aluminum chamber and an uncoated chamber with a factor of ten lower synchrotron radiation dose. The shape and size of the leading bunch signal show that the quantum efficiency for producing photoelectrons from reflected photons is much lower for the TiN coating. The secondary yield is also significantly smaller. A comparison between TiN and amorphous carbon coatings is shown in Fig. 1.83. The later, smaller signal from the leading bunch from the a-carbon chamber shows that the quantum efficiency is lower, particularly for high-energy photoelectrons. However, the similar magnitudes of the signals from the witness bunch indicate that the secondary yield for TiN is somewhat smaller than that for a-carbon. Further modeling promises to provide quantitative results for these qualitative observations.

Use of a Weak Solenoidal Magnetic Field One type of measurement which has been obtained with the shielded-pickup detectors is illustrated schematically in Fig. 1.84. The vacuum chambers have been outfitted with windings to approximate a solenoidal field in the region of the cloud with magnitude up to 40 G. Since signal contributions require nearly vertical arrival angles, the centers of

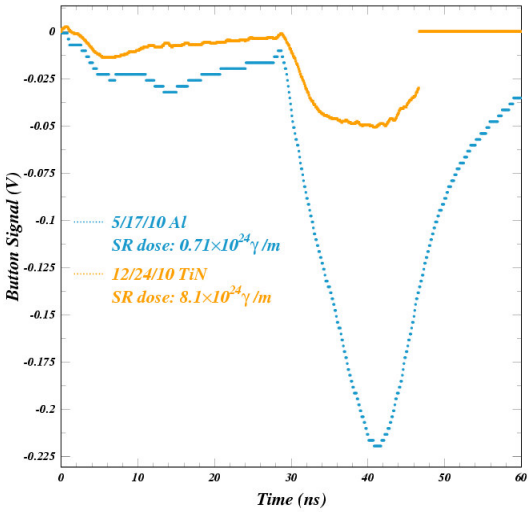

Figure 1.82: SPU signals exhibiting the difference in cloud buildup characteristics between a TiN-coated aluminum chamber and an uncoated aluminum chamber with a factor of ten lower synchrotron radiation dose

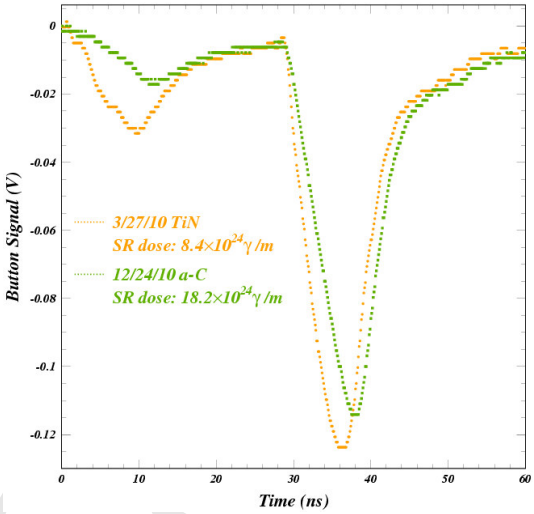

Figure 1.83: SPU signals exhibiting the difference in cloud buildup characteristics between a-carbon-coated and TiN-coated aluminum chambers

the corresponding circular trajectories for any given magnetic field value lie in the horizontal plane of the ports. The three trajectories originating at the primary impact point of the synchrotron radiation and leading to the center of each electrode thus select different regions of photoelectron energy and production angle, as shown. Experiments to date have shown that the 40 G field magnitude range suffices to cover the full energy range of the photoelectrons produced by a 2.1 GeV beam ($E_{critical} \approx 300$ eV) (i.e. no pickup signal is observed for field values of 0 and 40 G), in contrast to the case of a 5.3 GeV beam ($E_{critical} \approx 5$ keV), where photoelectron energies suffice to produce an observable signal even at 40 G. Furthermore, reversal of the solenoidal field provides information on the production of photoelectrons at a point on the vacuum chamber opposite the primary source point and thus relevant to the reflective characteristics of the vacuum chamber wall. This paper does not discuss in detail the measurements obtained with solenoidal field, which remain under analysis,

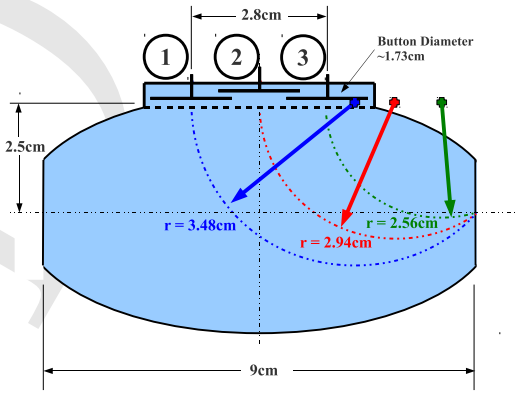

Figure 1.84: Vacuum chamber wall cross section with circular trajectories of photoelectrons contributing to the pickup signals.

but instead concentrates on an alternative method to measure photoelectron energy.

Summary The shielded pickup detectors installed in the CESR ring in 2010 have begun providing a wide variety of time-resolved measurements of electron-cloud-induced signals. Measurements with custom vacuum chambers incorporating cloud mitigation techniques such as carbon and titanium-nitride coatings have been obtained and compared to the case of an uncoated aluminum chamber. Weak solenoidal magnetic fields have been employed to study photoelectron production kinematics. A model for the shielded pickup acceptance has been developed in the context of the electron cloud simulation code ECLOUD. The shielded pickup data have proved remarkably sensitive to model parameters poorly constrained by any other experimental means, such as the azimuthal production distribution for photoelectrons and their energy distributions. The measurements with 5.3 GeV electron and positron beams indicate the need for a high-energy component previously absent in the photoelectron generation model. In addition, the design purpose of the shielded pickup detectors has been experimentally confirmed, as the cloud lifetime has been accurately measured using witness bunches at various delays. Sensitivity to the elastic yield parameter in the secondary yield model has been shown to be less than 0.05 and remarkably robust against variation of other model parameters. Data taken with an uncoated aluminum chamber provide a best estimate for the elastic yield of about 0.75. The cloud lifetime studies in a titanium-nitride-coated aluminum chamber exclude such a high value, yielding an optimal value of 0.05.

1.3 Comparisons Between Methods

1.3.1 Wiggler Ramp Studies

1.3.2 Comparison of RFA and Shielded Button Responses

1.3.3 TE Wave-Driven Resonance Studies with RFAs

1.4 Summary and Further Investigations

Appendix A

Some LaTeXing Examples

This appendix provides some examples of how to do things in LaTeX for the Phase I Report and provides some guidelines for preparing material for the report.

Note for experienced LaTeX users: the Phase I Report will generally follow "standard" usage for LaTeX and BibTeX. Hence, you do not need to peruse the examples below in detail; it is recommended that you skim through the material and make note of the guidelines for the preparation of the report (in particular, see Section A.2.2, Section A.7.1, and Section A.7.3). Note that the additional features provided by the 'graphicx' and 'natbib' packages will be available (as described in some of the examples below), but standard commands for graphics inclusion and citations will still work if you prefer to use them.

We fully expect that some formats will evolve through the course of editing the full document. We will add further examples, as needed, based on questions that come from the contributors. So **check back often!**

A.1 Special Commands

For CesrTA, use the command:

```
\cesrta
```

If you need to force a space after CesrTA, then use:

```
\cesrta\
```

A.2 Figures

A.2.1 Figure Logistics

The following figures show examples of the commands for inserting various types of graphics. Graphics files in JPEG, PDF, EPS, and PNG can be readily incorporated into the document. If you need help including a file of a different type, please consult with the editors. Each figure must include a caption and a label for cross-referencing the figure in the text.

Figure A.1 shows an example in which the graphic is a JPEG photo. In this example, the size is set by specifying the width as an absolute dimension. The height is not specified, which results in the aspect ratio being preserved. The graphic is centered between the left and right margins.

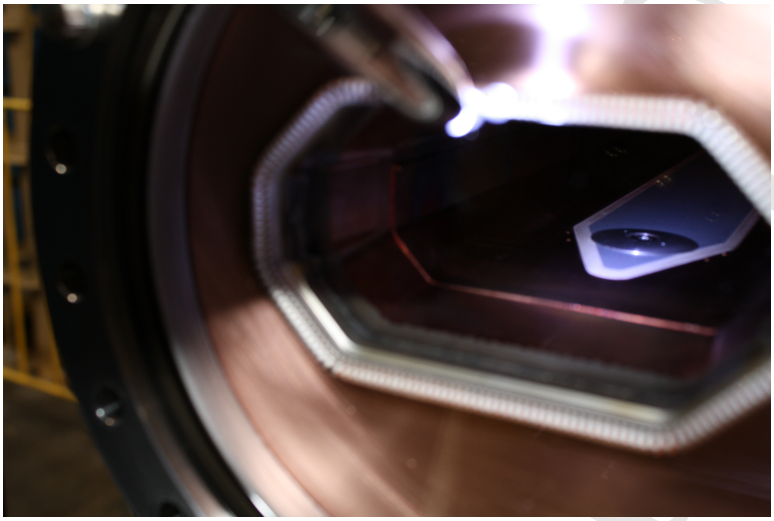

Figure A.1: Example of including a JPEG photo.

Figure A.2 shows an example in which the graphic is a PDF file. In this example, the size is set by specifying the width relative to the column width (the report is one-column, so the column width is equal to the text width).

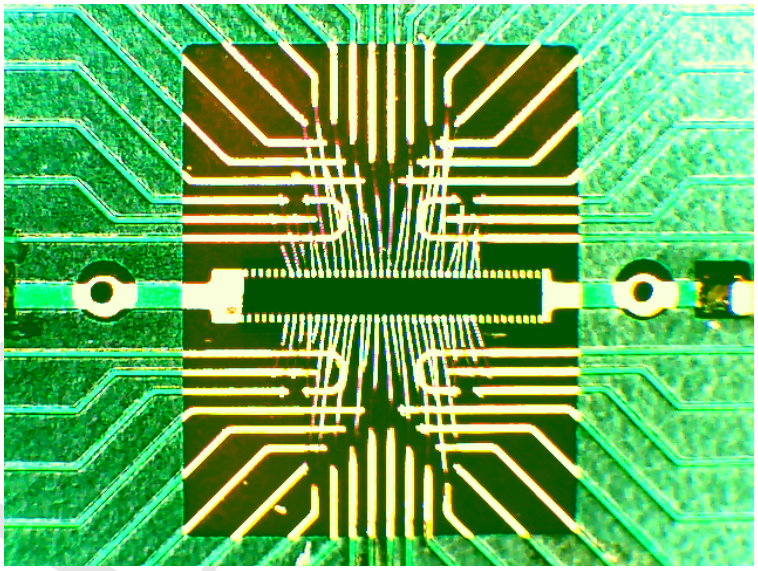

Figure A.2: Example of including a PDF photo. The caption can contain additional information that is relevant to the figure. Although the figure can obviously be discussed in the text of the report, it may be helpful to put some information directly in the caption.

Figure A.3 shows an example in which the graphic is an EPS file. In this example, the height is specified as an absolute dimension, and the aspect ratio is preserved by not specifying the width.

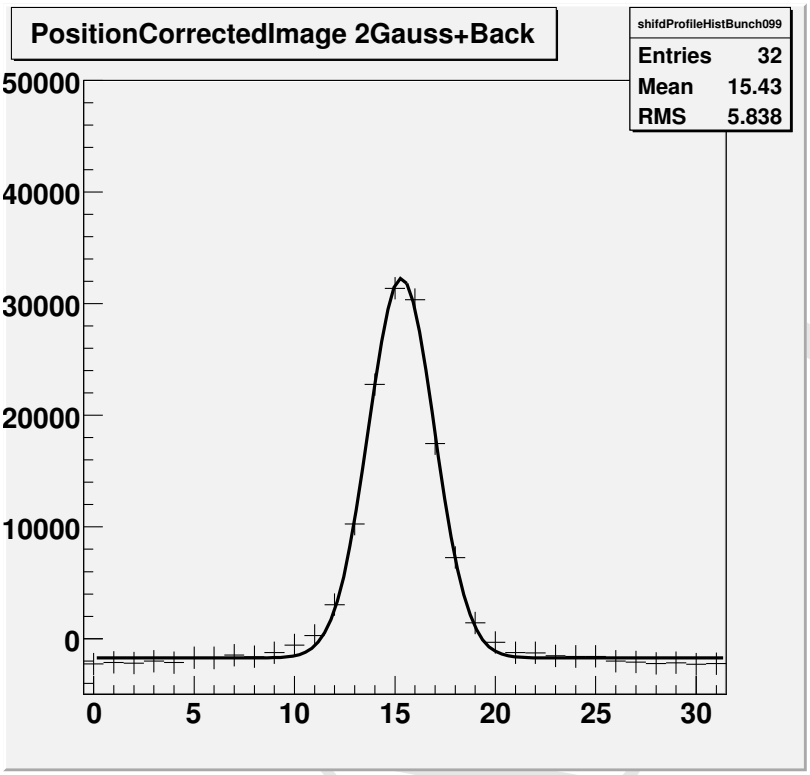

Figure A.3: Example of including an EPS plot.

Figure A.4 shows an example in which the graphic is a PNG file. In this example, the height is specified relative to the text height. The height of the figure should always be smaller than the text height in order to allow room for the figure caption.

Captions are produced with an automatically-generated figure number using the `\caption` command. The caption should be below the graphics. For long figure captions, it is useful to provide a short caption as an optional argument. The short caption is used in the list of figures. This is illustrated in Figure A.2.

Figures may contain more than one graphic. Examples where this option may be useful include different views of the same object, different plots that are related to each other, and so on. Figure A.5 shows an example in which 2 graphics are included.

LaTeX allows for an optional argument to specify the placement of the figure on the page. Placement options include h (here), t (top of page), b (bottom of page), and p (on a separate page with no text). Generally it is better to not worry about the figure placement until the final stages of document preparation, since the figures locations will change as material is added or removed within one section or in preceding sections.

A.2.2 Figure Guidelines

Since the purpose of figures is to supplement the message conveyed in the text, all of the figures that appear in the report should be referenced in the text of the report.

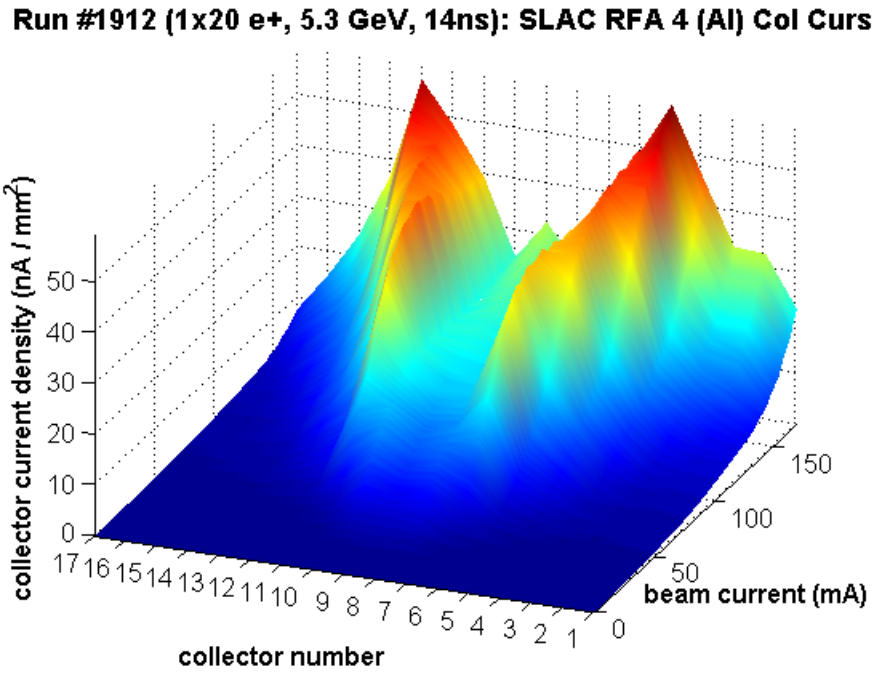

Figure A.4: Example of including a PNG plot.

Common categories of figures are photographs (see Figure A.1 and Figure A.2 for examples), plots (see Figure A.3 and Figure A.4 for examples), and drawings. JPEG is the recommended format for photographs. For plots and drawings, where possible, "vector" formats are recommended in lieu of "bit-mapped" formats. Vector formats generally provide better image resolution and smaller file sizes. JPEG and PNG formats are bit-mapped formats, so they should be avoided for plots and drawings if possible. Vector formats can be produced as EPS or PDF files (note, however, that EPS and PDF files can also be produced with bit-mapped content). Three-dimensional drawings may have to be produced as bitmaps.

Methods for producing graphic files may vary, depending on the software used to produce the graphic. "Save as EPS" is generally a good option, if available. "Save as PDF" may also work. In some case, it may be necessary to select "Print" and then print the graphic to a file, selecting "PostScript" or "PDF Creator" as the printer, and choosing "EPS" as a PostScript feature. If the output file has extension ".prn," this can be changed to ".eps."

Generally is is preferable to place information about the figure in the figure caption, rather than adding a label to the figure itself. According to this line of reasoning, the information at the top of Figure A.4 could be removed from the graphic and added to the caption.

A.3 Tables

This section provides an example table with the style features that are specified for the CesrTA Phase I Report. We appreciate your adherence to this format.

Table A.1 provides the list of chapters and coordinators for this project. Please feel free to contact

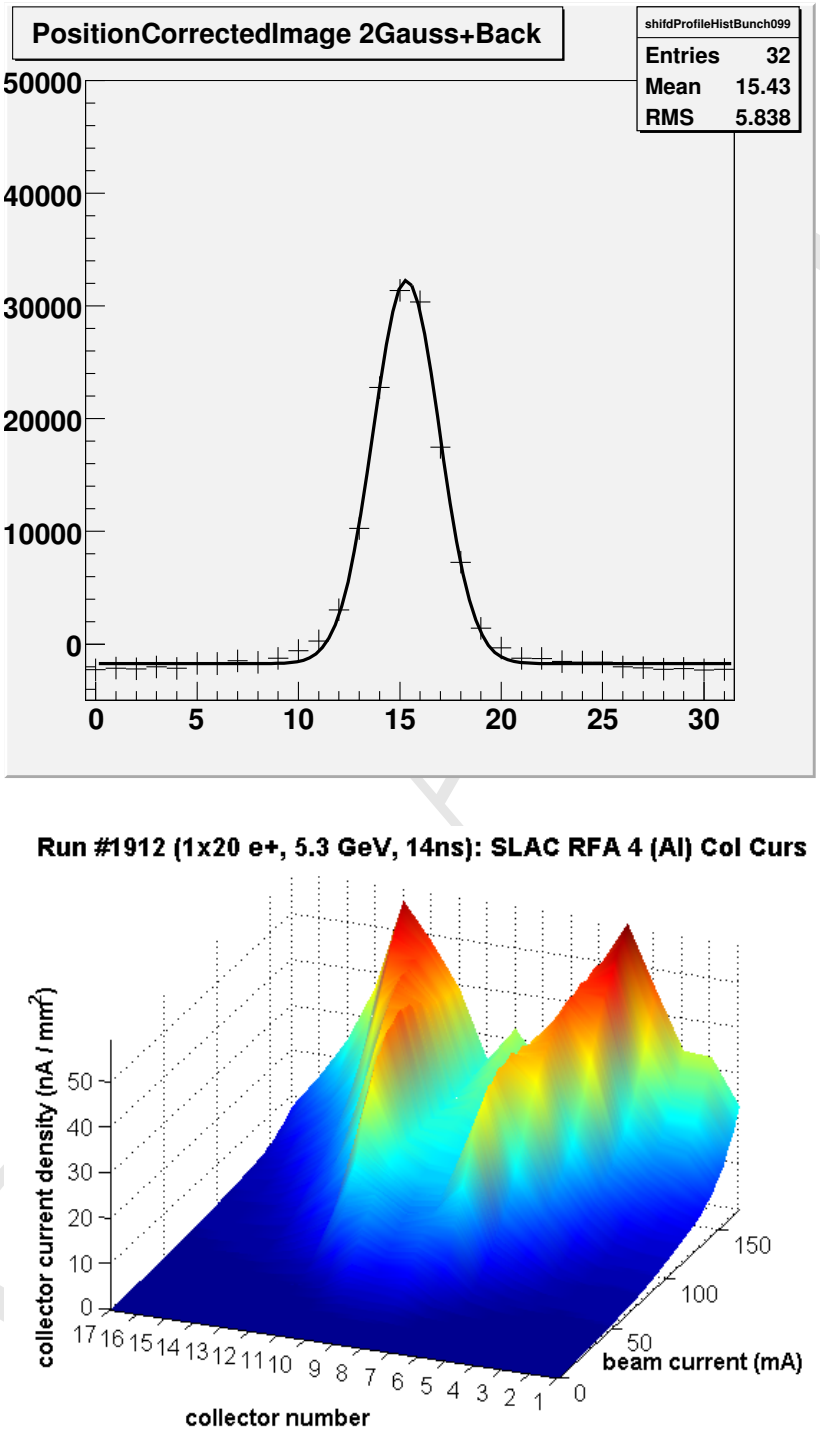

Figure A.5: Example of including two graphics in one figure. Top: top figure in EPS format. Bottom: bottom figure in PNG format.

them with questions about your LaTeX contributions.

Table A.1: List of chapter coordinators.

Chapter	Topic	Coordinator
Ch. ??	Introduction	M. Billing
Ch. ??	CESR Conversion	M. Palmer
Ch. ??	Low Emittance Tuning	D. Rubin
Ch. 1	EC Growth	M. Palmer
Ch. ??	EC Dynamics	G. Dugan
Ch. ??	ILC Recommendations	M. Palmer
Ch. ??	Conclusion	M. Billing
-	Bibliography	W. Hartung

As shown in this example, tables should be centered between the left and right margins. The caption should be placed above the table. A short form of the caption may be provided for the list of tables via the optional argument to the `\caption` command. The placement options and guidelines described above for figures also apply to tables.

A.4 Equations

Equations may be "in-text," such as $E = mc^2$, or displayed. Equation (A.1) is an example of a displayed equation generated by MathType:

$$\Delta a = 2\pi G_{\infty}\alpha\lambda\left(e^{-z/\lambda} - 1\right). \tag{A.1}$$

Please remember to **label** all equations. For a single equation, as in the example above, this can be done by using the `equation` environment, which produces the equation with an automatically-generated equation number. To cross-reference the equation in the text, as above, label it with a key using `\label{key}` inside the `equation` environment and then use `\ref{key}` to generate the equation number. As illustrated above, generally the format of the cross-reference should be something like

```
...as shown in Equation~(\ref{key}).
```

Note the inclusion of parentheses around the equation number.

For a group of two or more equations, use the `eqnarray` environment instead of the `equation` environment.

A.5 List Environments

When creating numbered or un-numbered lists, please use the list environments provided with /LaTeX/ in order to standardize the look and feel of the presentation instead of emulating it yourself. This is accomplished by using the *itemize* or *enumerate* environments. Note that lists can be nested. A bulleted list can be created with the following commands (note that the indentation used is to make the example more easily readable - it's not required):

```
\begin{itemize}
   \item First item
   \begin{itemize}
         \item First sub-item
         \item Second sub-item
   \end{itemize}
   \item Second item
   \item Third item
\end{itemize}
```

which renders as:

- First item
  - First sub-item
  - Second sub-item
- Second item
- Third item

If you prefer a numbered list you can use (note that the indentation used is to make the example more easily readable - it's not required):

```
\begin{enumerate}
   \item First item
   \begin{enumerate}
         \item First sub-item
         \item Second sub-item
   \end{enumerate}
   \item Second item
   \item Third item
\end{enumerate}
```

which renders as:

1. First item
   (a) First sub-item
   (b) Second sub-item
2. Second item
3. Third item

A.6 Cross-References

References to figures, tables, equations, and other parts of the report are all done in a similar way using a key to specify the item of interest. To reference a chapter or section (or subsection,...) of the report, make sure the item of interest has a `\label{key}` associated with it, and then reference it with the `\ref` command using its key, for example, Chapter **??**. The `\label{key}`

declaration should appear inside or just after the sectioning command which defines the beginning of the sectional unit.

A.7 Bibliography and Citations

A.7.1 Bibliography Logistics

The bibliography will be generated using BibTeX. A BibTeX database has been set up, mostly from a search for existing CesrTA papers and from citations therein. The supplementary material for the CesrTA proposal and review has also been included for the most part. Keys have been assigned to all entries in the BibTeX database. Additional keys will be assigned by the bibliography coordinator for new entries.

You may view the BibTeX file (CesrTA.bib) in CesrTA Wiki area for the Phase I Report (or download (check out) with the rest of the files). It is in the `Bibliography/` directory.

You may also view an HTML list of papers in the database with keys and links. The file (HtmlCesrTA.htm) is in the same directory as the BibTeX file. You may view it with a Web browser.

Please check whether all of the references you wish to cite are in the database and send the information for those that are missing to the bibliography coordinator. Alternatively, you may send your existing list of references to the coordinator, who can then add the missing ones to the database. You can send your reference list in the form of an existing BibTeX file, in another format, or in the form of a paper whose reference list you want to include in the database.

There will be one bibliography for the entire Phase I Report. Please notify the coordinator when you find errors and omissions in the database.

A.7.2 Citation Logistics

The report will make use of the 'natbib' package for citations. Citations will be numbered according to the order in which they appear. Instead of the standard `\cite{key}` command, please use natbib's `\citep{key}` command (for a "parenthetical" citation). You may provide a list of keys, as in `\citep{key1, key2,...}`. The natbib package will perform sorting and compression when multiple keys are provided.

Example: to cite a reference such as the CESR Conversion PAC09 paper [1], use

```
...during the CESR Conversion~\citep{PAC09:FR1RAI02}.
```

The tilde between the text and the citation inserts a "non-breakable" space, which prevents the citation from appearing at the beginning of a new line.

For those who find a non-standard command objectionable, natbib also allows the standard `\cite` command in place of `\citep`. The natbib package provides many other features, although they are mostly oriented toward support for "author-year" citations and are not likely to be very useful for numbered citations. Some of the natbib features are not fully supported by the bibliography style that we are using for the Phase I Report (`\citet`, for example), but this should not be an issue, since we are not using "author-year" citations.

You may wish to refer to a particular part of a paper that you cite (a page number, a section, a figure, a table, etc.). This is generally to be encouraged, especially when you are citing material in a book, design report, etc. The recommended method for this report is to cite the paper in the bibliography and specify the part of interest in the text. The optional argument of the `\citep` command may be useful for this purpose. Example:

```
This was already demonstrated before the last round of
measurements~\citep[Figures 3 and 4]{IPAC10:TUPD022}.
```

The above modifies the citation [41, Figures 3 and 4]. (Note that this works the same way as for the standard LaTeX `\cite` command.) By putting the specifics in the text, we can avoid multiple entries in the bibliography for the same work.

A.7.3 Bibliography and Citation Guidelines

It is preferable for the references in the bibliography to be ones that are available to the public. In cases where it is necessary for to cite work that is not in the public domain, you might consider how the work could be made publicly available. For work that is not suitable for journal articles or conference proceedings, there are other options, including e-print servers and archives of laboratory reports, including several report series associated with CESR/LEPP/CLASSE.

The bibliography can be used to acknowledge "private communications" for unpublished information, but this should be used sparingly (also, citing a "private communication" from someone who is one of the authors of the Phase I Report might be considered a circular argument).

You may wish to include information about a device or product and its manufacturer in the report. Please include this information in the text or in a footnote.[1] Example:

```
We used a dc electron gun\footnote{Model ELG-2, Kimball
Physics, Inc., Wilton, NH.} positioned at 25 degrees
to the manipulator.
```

A.7.4 Bibliography Details

The coordinator will try to make sure that consistency is maintained between different database entries and will try to identify and eliminate duplicate entries associated with works that have been published in more than one way. For cases in which a paper is determined to have been published as an internal report/pre-print/e-print as well as a proceedings paper or a journal article, the latter version will be used preferentially.

In assigning keys, the goal is to maintain a scheme whereby a unique key can be associated with each entry in the database. The disadvantage is that the keys are long. The advantage (we hope) is that the bibliography database can be expanded and updated in the future for other reports, proposals, etc.

The format of the bibliography will be determined by the BibTeX bibliography style, and will not necessarily be the same as the list of papers mentioned above (which was converted to HTML using somewhat primitive methods). In particular, the bibliography will not include URLs.

[1] This is an example of a footnote.

The rule of thumb is that each entry in the bibliography will be a "stand-alone" entry. In other words, the XREF feature of BibTeX will not be used to cross-reference one entry to another.

Bibliography

[1] M. A. Palmer *et al.*, "The Conversion and Operation of the Cornell Electron Storage Ring as a Test Accelerator (CesrTA) for Damping Rings Research and Development," in *Proceedings of the 2009 Particle Accelerator Conference, Vancouver, BC* (2009), p. 4200–4204.

[2] M. Izawa, Y. Sato & T. Toyomasu, "The Vertical Instability in a Positron Bunched Beam," *Phys. Rev. Lett.* **74**, p. 5044–5047 (Jun. 1995).

[3] K. Ohmi, "Beam-Photoelectron Interactions in Positron Storage Rings," *Phys. Rev. Lett.* **75**, p. 1526–1529 (Aug. 1995).

[4] H. Fukuma, "Electron Cloud Instability in KEKB and SuperKEKB," in *ICFA Beam Dynamics Newsletter*, M. E. Biagini, Ed., International Committee on Future Accelerators, No. 48, p. 112–118 (Apr. 2009).

[5] P. Cruikshank *et al.*, "Mechanical Design Aspects of the LHC Beam Screen," in *Proceedings of the 1997 Particle Accelerator Conference, Vancouver, BC, Canada* (1997), p. 3586–3588.

[6] F. Zimmermann, "A Simulation Study of Electron-Cloud Instability and Beam-Induced Multipacting in the LHC," Tech. Rep. SLAC-PUB-7425/CERN LHC Project Report 95, SLAC/CERN, Stanford, CA/Geneva, Switzerland (Feb. 1997).

[7] M. A. Furman, "The Electron-Cloud Effect in the Arcs of the LHC," Tech. Rep. LHC Project Report 180/LBNL-41482/CBP Note 247, CERN, Geneva, Switzerland (May 1998).

[8] F. Ruggiero, "Electron Cloud in the LHC," in *Beam Dynamics Issues for e+ e- Factories: Proceedings: 14th Advanced ICFA Beam Dynamics Workshop, Frascati, Italy, 1997*, L. Palumbo & G. Vignola, Eds. (1997), Fascati Physics Series, Vol. 10, p. 437–444.

[9] J. M. Jimenez *et al.*, "Vacuum and Cryogenic Observations for Different Bunch Spacing," in *Proceedings of the 2011 LHC Performance Workshop, Chamonix*, C. Carli, Ed. (2011), CERN-ATS-2011-005, p. 56–62.

[10] O. Gröbner, "Bunch Induced Multipactoring," in *Proceedings of the X International Conference on High Energy Accelerators, Protvino, USSR, 1977*, Y. M. Ado *et al.*, Eds. (1977), p. 277–282.

[11] R. J. Macek *et al.*, "Status of Experimental Studies of Electron Cloud Effects at the Los Alamos Proton Storage Ring," in *Proceedings of ECLOUD 2004: 31st ICFA Advanced Beam Dynamics Workshop on Electron-Cloud Effects, Napa, CA*, M. Furman, S. Henderson & F. Zimmerman, Eds. (2004), CERN-2005-001, p. 63–75.

[12] V. Dudnikov, "Some Features of Transverse Instability of Partly Compensated Proton Beams,"

in *Proceedings of the 2001 Particle Accelerator Conference, Chicago, IL*, P. Lucas & S. Webber, Eds. (2001), p. 1892–1894.

[13] K. Smolenski, Ed., *Proceedings of ECLOUD 2010: 49th ICFA Advanced Beam Dynamics Workshop on Electron Cloud Physics, Ithaca, NY* (in press).

[14] K. C. Harkay & R. A. Rosenberg, "Properties of the Electron Cloud in a High-Energy Positron and Electron Storage Ring," *Phys. Rev. ST Accel. Beams* **6**, 034402 (Mar. 2003).

[15] Z. Y. Guo *et al.*, "The Experimental Study on Beam-Photoelectron Instability in BEPC," in *Proceedings of the 1997 Particle Accelerator Conference, Vancouver, BC, Canada* (1997), p. 1566–1568.

[16] J. A. Holmes *et al.*, "Computational Beam Dynamics Studies of Collective Instabilities Observed in SNS," in *Proceedings of the 2008 European Particle Accelerator Conference, Genoa, Italy* (2008), p. 1640–1642.

[17] W. Fischer *et al.*, "Electron Cloud Observations and Cures in the Relativistic Heavy Ion Collider," *Phys. Rev. ST Accel. Beams* **11**, 041002 (Apr. 2008).

[18] R. J. Macek *et al.*, "Electron Cloud Diagnostics in Use at the Los Alamos PSR," in *Proceedings of the 2003 Particle Accelerator Conference, Portland, OR*, J. Chew, P. Lucas & S. Webber, Eds. (2003), p. 508–510.

[19] R. Cimino *et al.*, "Electron Cloud Build-Up Study for DAΦNE," in *Proceedings of the 2005 Particle Accelerator Conference, Knoxville, TN*, C. Horak, Ed. (2005), p. 779–781.

[20] M. A. Furman & G. R. Lambertson, "The Electron-Cloud Instability in the Arcs of the PEP-II Positron Ring," in *Proceedings of MBI97: International Workshop on Multibunch Instabilities in Future Electron and Positron Accelerators, Tsukuba, Japan, 1997*, Y. H. Chin, Ed. (1997), KEK Proceedings 97-17, p. 170.

[21] A. Kulikov *et al.*, "The Electron Cloud Instability at PEP-II," in *Proceedings of the 2001 Particle Accelerator Conference, Chicago, IL*, P. Lucas & S. Webber, Eds. (2001), p. 1903–1905.

[22] X. Zhang *et al.*, "Electron Cloud Studies at Tevatron and Main Injector," in *Proceedings of the 2007 Particle Accelerator Conference, Albuquerque, NM*, C. Petit-Jean-Genaz, Ed. (2007), p. 3501–3503.

[23] R. Cappi *et al.*, "Electron Cloud Buildup and Related Instability in the CERN Proton Synchrotron," *Phys. Rev. ST Accel. Beams* **5**, 094401 (Sep. 2002).

[24] G. Rumolo *et al.*, "Experimental Studies on the SPS Electron Cloud," in *Proceedings of BEAM 2007: CARE-HHH-APD Workshop on Finalizing the Roadmap for the Upgrade of the CERN & GSI Accelerator Complex, Geneva, Switzerland*, W. Scandale & F. Zimmermann, Eds. (2007), CERN-2008-005/CARE-Conf-08-004-HHH, p. 202–208.

[25] K. Akai, "High Intensity Issues for Super B-Factories," in *Proceedings of the 2003 Particle Accelerator Conference, Portland, OR*, J. Chew, P. Lucas & S. Webber, Eds. (2003), p. 356–360.

[26] G. Rumolo, W. Bruns & Y. Papaphilippou, "Electron Cloud Build Up and Instability in the CLIC Damping Rings," in *Proceedings of the 2008 European Particle Accelerator Conference, Genoa, Italy* (2008), p. 661–663.

[27] M. Pivi *et al.*, "Suppressing Electron Cloud in Future Linear Colliders," in *Proceedings of the 2005 Particle Accelerator Conference, Knoxville, TN*, C. Horak, Ed. (2005), p. 24–28.

[28] F. Le Pimpec *et al.*, "Properties of TiN and TiZrV Thin Film as a Remedy Against Electron Cloud," *Nucl. Instrum. Methods Phys. Res.* **A551**, p. 187–199 (Jul. 2005).

[29] Y. Funakoshi *et al.*, "KEKB Performance," in *Proceedings of the 2001 Particle Accelerator Conference, Chicago, IL*, P. Lucas & S. Webber, Eds. (2001), p. 3546–3548.

[30] D. Schulte & F. Zimmermann, "Electron Cloud Build-Up Simulations using ECLOUD," in *Proceedings of ECLOUD 2004: 31st ICFA Advanced Beam Dynamics Workshop on Electron-Cloud Effects, Napa, CA*, M. Furman, S. Henderson & F. Zimmerman, Eds. (2004), CERN-2005-001, p. 143–152.

[31] G. Rumolo & F. Zimmermann, "Electron Cloud Simulations: Beam Instabilities and Wakefields," *Phys. Rev. ST Accel. Beams* **5**, 121002 (Dec. 2002).

[32] L. F. Wang *et al.*, "Numerical Study of the Photoelectron Cloud in KEKB Low Energy Ring with a Three-Dimensional Particle in Cell Method," *Phys. Rev. ST Accel. Beams* **5**, 124402 (Dec. 2002).

[33] L. F. Wang, "User's Guide for CLOUDLAND," Tech. Rep. KEK Internal 2003-2, KEK, Tsukuba, Japan (2003).

[34] M. A. Furman & M. T. F. Pivi, "Probabilistic Model for the Simulation of Secondary Electron Emission," *Phys. Rev. ST Accel. Beams* **5**, 124404 (Dec. 2002).

[35] J.-L. Vay *et al.*, "Update on Electron-Cloud Simulations Using the Package WARP-POSINST," in *Proceedings of the 2009 Particle Accelerator Conference, Vancouver, BC* (2009), p. 4719–4721.

[36] K. Ohmi, "Particle-in-Cell Simulation of Beam-Electron Cloud Interactions," in *Proceedings of the 2001 Particle Accelerator Conference, Chicago, IL*, P. Lucas & S. Webber, Eds. (2001), p. 1895–1897.

[37] L. Wang & M. Pivi, "Trapping of Electron Cloud in ILC/CesrTA Quadrupole and Sextupole Magnets," in *Proceedings of ECLOUD 2010: 49th ICFA Advanced Beam Dynamics Workshop on Electron Cloud Physics, Ithaca, NY*, K. Smolenski, Ed. (in press).

[38] C. M. Celata, "Electron Cloud Dynamics in the Cornell Electron Storage Ring Test Accelerator Wiggler," *Phys. Rev. ST Accel. Beams* **14**, 041003 (Apr. 2011).

[39] F. Zimmermann, G. Rumolo & K. Ohmi, "Electron Cloud Build Up in Machines with Short Bunches," in *ICFA Beam Dynamics Newsletter*, K. Ohmi & M. Furman, Eds., International Committee on Future Accelerators, No. 33, p. 14–24 (Apr. 2004).

[40] M. A. Palmer *et al.*, "Design, Implementation and First Results of Retarding Field Analyzers Developed for the CesrTA Program," in *Proceedings of the 2009 Particle Accelerator Conference, Vancouver, BC* (2009), p. 3510–3512.

[41] J. R. Calvey *et al.*, "CesrTA Retarding Field Analyzer Modeling Results," in *Proceedings of the 2010 International Particle Accelerator Conference, Kyoto, Japan* (2010), p. 1970–1972.

[42] M. T. F. Pivi *et al.*, "Observation of Magnetic Resonances in Electron Clouds in a Positron Storage Ring," *Nucl. Instrum. Methods Phys. Res.* **A621**, p. 33–38 (Sep. 2010).

[43] C. M. Celata *et al.*, "Cyclotron Resonances in Electron Cloud Dynamics," in *Proceedings of the 2009 Particle Accelerator Conference, Vancouver, BC* (2009), p. 1807–1811.

[44] Y. Suetsugu *et al.*, "Experimental Studies on Grooved Surfaces to Suppress Secondary Electron Emission," in *Proceedings of the 2010 International Particle Accelerator Conference, Kyoto, Japan* (2010), p. 2021–2023.

[45] J. Kim *et al.*, "In Situ SEY Measurements at CesrTA," in *Proceedings of ECLOUD 2010: 49th ICFA Advanced Beam Dynamics Workshop on Electron Cloud Physics, Ithaca, NY*, K. Smolenski, Ed. (in press).

[46] F. Le Pimpec, F. King & R. E. Kirby, "Electron Conditioning of Technical Aluminum Surfaces," Tech. Rep. LCC-0153/SLAC-TN-04-051, Linear Collider Collaboration/SLAC, Stanford, CA (Sep. 2004).

[47] K. G. McKay, "Secondary Electron Emission," in *Advances in Electronics*, L. Marton, Ed., Academic Press, New York, vol. I, p. 65–130 (1948).

[48] T. Kroyer *et al.*, "Unexpected Results on Microwave Waveguide Mode Transmission Measurements in the SPS Beam Pipe," in *Proceedings of ECLOUD 2004: 31st ICFA Advanced Beam Dynamics Workshop on Electron-Cloud Effects, Napa, CA*, M. Furman, S. Henderson & F. Zimmerman, Eds. (2004), CERN-2005-001, p. 89–94.

[49] J. P. Sikora, S. De Santis & K. Hammond, "TE Wave measurements at CesrTA," in *Proceedings of ECLOUD 2010: 49th ICFA Advanced Beam Dynamics Workshop on Electron Cloud Physics, Ithaca, NY*, K. Smolenski, Ed. (in press).

[50] S. De Santis *et al.*, "Characterization of Electron Clouds in the Cornell Electron Storage Ring Test Accelerator using TE-Wave Transmission," *Phys. Rev. ST Accel. Beams* **13**, 071002 (Jul. 2010).

[51] B. Carlson *et al.*, "Implementation and Comparison of Electron Cloud Measurements at the Cornell Electron Storage Ring," REU Report, LEPP, Cornell University, Ithaca, NY (2009).

[52] S. De Santis *et al.*, "Measurement of Electron Clouds in Large Accelerators by Microwave Dispersion," *Phys. Rev. Lett.* **100**, 094801 (Mar. 2008).

[53] E. Mahner, T. Kroyer & F. Caspers, "Electron Cloud Detection and Characterization in the CERN Proton Synchrotron," *Phys. Rev. ST Accel. Beams* **11**, 094401 (Sep. 2008).

[54] S. Federmann, F. Caspers & E. Mahner, "Measurements of Electron Cloud Density in the CERN Super Proton Synchrotron with the Microwave Transmission Method," *Phys. Rev. ST Accel. Beams* **14**, 012802 (Jan. 2011).

[55] K. Hammond *et al.*, "Effects of Reflections on TE-Wave Measurements of Electron Cloud Density," in *Proceedings of ECLOUD 2010: 49th ICFA Advanced Beam Dynamics Workshop on Electron Cloud Physics, Ithaca, NY*, K. Smolenski, Ed. (in press).

[56] M. A. Heald & C. B. Wharton, *Plasma Diagnostics with Microwaves*, John Wiley & Sons, New York (1965).

[57] S. J. Buchsbaum & S. C. Brown, "Microwave Measurements of High Electron Densities," *Phys. Rev.* **106**, p. 196–199 (Apr. 1957).

[58] R. G. Carter, "Accuracy of Microwave Cavity Perturbation Measurements," *IEEE Trans. Microwave Theory Tech.* **49**, p. 918–923 (May 2001).

[59] J. R. Calvey *et al.*, "Methods for Quantitative Interpretation of Retarding Field Analyzer Data," in *Proceedings of ECLOUD 2010: 49th ICFA Advanced Beam Dynamics Workshop on Electron Cloud Physics, Ithaca, NY*, K. Smolenski, Ed. (in press).

[60] J. A. Crittenden *et al.*, "Studies of the Effects of Electron Cloud Formation on Beam Dynamics at CesrTA," in *Proceedings of the 2009 Particle Accelerator Conference, Vancouver, BC* (2009), p. 4631–4633.

[61] J. A. Crittenden *et al.*, "Progress in Studies of Electron-cloud-induced Optics Distortions at CesrTA," in *Proceedings of the 2010 International Particle Accelerator Conference, Kyoto, Japan* (2010), p. 1976–1978.

[62] R. P. Badman, "Comparing ECLOUD Simulation Results to 2.1 and 5.3 GeV Positron Shielded Pickup Data," REU Report, LEPP, Cornell University, Ithaca, NY (Aug. 2011).

[63] G. Dugan & D. Sagan, "Synrad3D Photon Propagation and Scattering Simulation," in *Proceedings of ECLOUD 2010: 49th ICFA Advanced Beam Dynamics Workshop on Electron Cloud Physics, Ithaca, NY*, K. Smolenski, Ed. (in press).

[64] L. Boon *et al.*, "Application of the SYNRAD3D Photon-Tracking Model to Shielded Pickup Measurements of Electron Cloud Buildup at CesrTA," in *Proceedings of the 2011 International Particle Accelerator Conference, San Sebastián, Spain* (in press).

[65] U. Iriso & G. Rumolo, "Benchmarking Electron Cloud Data with Computer Simulation Codes," in *Proceedings of the 2006 European Particle Accelerator Conference, Edinburgh, Scotland* (2006), p. 363–365.

[66] J. A. Crittenden *et al.*, "Recent Developments in Modeling Time-Resolved Shielded-Pickup Measurements of Electron Cloud Buildup at CESRTA," in *Proceedings of the 2011 International Particle Accelerator Conference, San Sebastián, Spain* (in press).

[67] J. A. Crittenden *et al.*, "Electron Cloud Modeling Results for Time-Resolved Shielded Pickup Measurements at CesrTA," in *Proceedings of ECLOUD 2010: 49th ICFA Advanced Beam Dynamics Workshop on Electron Cloud Physics, Ithaca, NY*, K. Smolenski, Ed. (in press).

[68] J. A. Crittenden *et al.*, "Electron Cloud Modeling Results for Time-Resolved Shielded Pickup Measurements at CesrTA," in *Proceedings of the 2011 Particle Accelerator Conference, New York, NY* (in press).